20/5/8

Indian J. pure appl. Phys., Vol. 18 No. 3 pp. 147-226
March 1980
CODEN : IJOPAU ISSN : 0019-5596
18 (3) 147-226 (1980)

147
20-5-80

INDIAN JOURNAL OF PURE & APPLIED PHYSICS

Published by
THE COUNCIL OF SCIENTIFIC & INDUSTRIAL RESEARCH, NEW DELHI
in association with
THE INDIAN NATIONAL SCIENCE ACADEMY, NEW DELHI

AA PRE-EMINENCE ...AT THE TOUCH OF A BUTTON...

For advanced programme flexibility, Pye Unicam have partnered their atomic absorption spectrophotometers with DATA CENTRE, an exceptionally low cost, touch button, microprocessing system. For example, you can now achieve even more with the Pye Unicam SP2900... the instrument with a performance that is unequalled by literally any other atomic absorption spectrophotometer.

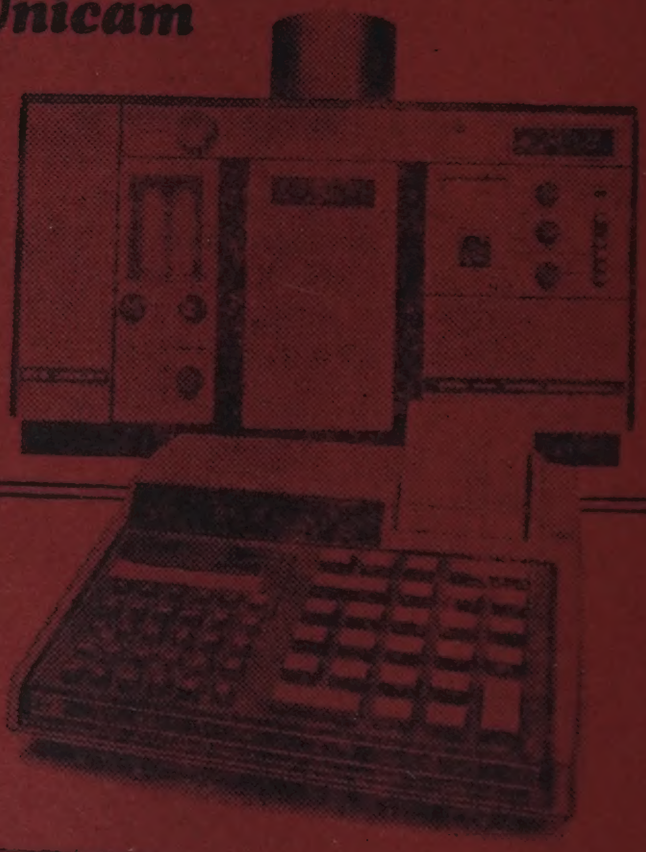

Send for details...

For further details contact:-
Pelco Electronics & Electricals Limited
Product Division
Science & Industry
Shivsagar Estate, Block 'A'
Worli, Bombay-400 018

PHILIPS

PEST 4968

FORM IV

(See Rule 8)

1.	Place of publication	New Delhi 110 012
2.	Periodicity of publication	Monthly
3.	Printer's name Nationality Address	D S Sastry Indian Publications & Information Directorate (CSIR), New Delhi-12
4.	Publisher's name Nationality Address	Do
5.	Editor's name Nationality Address	Do
6.	Names and addresses of individuals who own the newspaper and partners or shareholders holding more than one per cent of the total capital	Nil

I, D S Sastry, hereby declare that the particulars given above are true to the best of my knowledge and belief.

(Sd) *D S Sastry*
Signature of Publisher

14 March 1980

CSIR SCIENTIFIC PERIODICALS

JOURNAL OF SCIENTIFIC & INDUSTRIAL RESEARCH (monthly)

With a fine record of over 35 years' service to the scientific community, this Journal has grown into India's leading general science periodical. Intended to fulfil the responsibility of helping the research workers to keep themselves abreast of current developments in various fields of science and technology, the Journal carries editorial features highlighting important scientific events in India and abroad; articles on science policy and management of science; review articles on topics of current research interest; technical reports on international and national conferences; reviews of scientific and technical publications; and notes on major advances in various fields.

Annual subscription	**Rs 60.00**	**£ 10.00**	**$ 25.00**
Single copy	**6.00**	**1.00**	**2.50**

INDIAN JOURNAL OF CHEMISTRY (monthly)

This Journal which is running the 18th year of publication, was split up into two sections with effect from January 1976.

Section A : This section is devoted to papers in Inorganic, Physical, Theoretical and Analytical Chemistry.

Annual subscription	**Rs 70.00**	**£ 12.00**	**$ 30.00**
Single copy	**7.00**	**1.20**	**3.00**

Section B : This section is devoted to papers in Organic Chemistry including Medicinal Chemistry.

Annual subscription	**Rs 70.00**	**£ 12.00**	**$ 30.00**
Single copy	**7.00**	**1.20**	**3.00**

INDIAN JOURNAL OF PURE & APPLIED PHYSICS (monthly)

This Journal, which is running the 18th year of its publication, is devoted to original research communications (full papers and short communications) in all conventional branches of physics (except radio and space physics).

Annual subscription	**Rs 100.00**	**£ 16.50**	**$ 42.00**
Single copy	**10.00**	**1.80**	**4.50**

INDIAN JOURNAL OF RADIO & SPACE PHYSICS (bimonthly)

This Journal is intended to serve as a medium for the publication of the growing research output in various areas of radio and space physics.

Annual subscription	**Rs 60.00**	**£ 10.00**	**$ 25.00**
Single copy	**12.00**	**2.00**	**5.00**

INDIAN JOURNAL OF TECHNOLOGY (INCLUDING ENGINEERING) (monthly)

This Journal publishes papers reporting results of original research of applied nature pertaining to unit operations, heat and mass transfer, products, processes, instruments, and appliances, etc. The Journal is of special interest to research workers in the departments of applied sciences in universities, institutes of higher technology, commodity research laboratories, industrial cooperative research institutes, and industrial research laboratories.

Annual subscription	**Rs 60.00**	**£ 10.00**	**$ 25.00**
Single copy	**6.00**	**1.00**	**2.50**

INDIAN JOURNAL OF EXPERIMENTAL BIOLOGY (monthly)

This Journal, devoted to the publication of research communications in the fields of experimental botany, zoology, microbiology, pharmacology, endocrinology, nutrition, etc., is the only one in India with such a wide coverage and scope.

Annual subscription	**Rs 120.00**	**£ 20.00**	**$ 50.00**
Single copy	**12.00**	**2.00**	**5.00**

INDIAN JOURNAL OF BIOCHEMISTRY & BIOPHYSICS (bimonthly)

This Journal, published in association with the Society of Biological Chemists (India), Bangalore, is the only research Journal in India devoted exclusively to original research communications in biochemistry and biophysics.

Annual subscription	**Rs 40.00**	**£ 7.00**	**$ 17.00**
Single copy	**8.00**	**1.40**	**3.50**

INDIAN JOURNAL OF MARINE SCIENCES (quarterly)

Commencing publication from June 1972, this Journal is devoted to research communications (full papers and short communications) pertaining to various facets of marine research, viz. biological, physical, geological and chemical oceanography.

Annual subscription	**Rs 40.00**	**£ 7.00**	**$ 17.00**
Single copy	**12.00**	**2.00**	**5.00**

RESEARCH & INDUSTRY (quarterly)

Intended to serve as a link between science and industry, this Journal is addressed primarily to technologists, engineers, executives and others in industry and trade. It publishes informative original articles containing practical details of processes and products developed in India, which show promise of ready utilization, and technical digests on new processes, products, instruments and testing methods which are of interest to industry. Developments in Indian industry are regularly reported.

Annual subscription	**Rs 24.00**	**£ 4.00**	**$ 10.00**
Single copy	**7.25**	**1.30**	**3.50**

INDIAN JOURNAL OF TEXTILE RESEARCH (quarterly)

Commencing publication from March 1976, this Journal is devoted to the publication of papers reporting results of fundamental and applied researches in the field of textiles.

Annual subscription	**Rs 36.00**	**£ 6.00**	**$ 15.00**
Single copy	**12.00**	**2.00**	**5.00**

Please contact

THE SALES & DISTRIBUTION OFFICER
PUBLICATIONS & INFORMATION DIRECTORATE, CSIR
HILLSIDE ROAD, NEW DELHI 110 012

Indian Journal of Pure & Applied Physics

VOLUME 18 No. 3 MARCH 1980

CONTENTS

Solid State Physics

Computer Simulation of Ternary Miscibility Gap in the Ternary Alloy $Pd_{77.5}$ Cu_6 $Si_{16.5}$ 147
RAHUL BASU

Transport Properties of Monoclinic Rare-Earth Sesquioxides 154
B K VERMA, VIRENDRA PRATAP & H B LAL

Lattice Distortion Spectrum of Evaporated Bismuth Films 159
SAMAR K SAHA & P C MAHANTA

Microtopographical Studies of Second Order Prism Faces of Synthetic Quartz Crystals 162
M S JOSHI & K B SARAF

Optical Study of Magnetic Polarization in Polypropylene 167
S ASGHAR HUSAIN & C S BHATNAGAR

Mathematical & Theoretical Physics

Massive Spheres : Some General Considerations & Applications 171
M C DURGAPAL & A K PANDE

Effect of Polarized Velocity Distribution of Electrons on Double Ionization of He by Proton Impact 176
VIR SINGH

Nuclear Physics

Coincidence Studies of ^{144}Ce with Improved Detection System 180
R K MISHRA

Dielectrics & Microwaves

Mechanism Responsible for the Observed Dielectric Relaxations in Polyvinylidene Fluoride 183
P C MEHENDRU, S CHAND & K JAIN

Spectroscopy

Polarized Absorption Spectra of Fluoranthene in Pure & Mixed Crystals ... 191
N B PALIT, S C CHAKRAVORTY & M K CHOUDHURY

Vibrational Spectra of Biological Molecules : 2, 4-Diamino-6-Hydroxy Pyrimidine 195
R K GOEL & S N SHARMA

CONTENTS

COMMUNICATIONS

Emission Spectrum of Copper Chloride Molecule 200
P MEENAKSHI RAJA RAO

NOTES

On the Debye Characteristic Temperature of Some Crystals with NaCl-type Structure 204
(Miss) DEBASRI BASU & J K D VERMA

Studies on the Stability & Strength of fcc Aluminium Using Morse Potential ... 205
A K MITRA & P K SENGUPTA

Isothermal Decay of CaO: Eu:Tb Phosphors 207
Y RAMAN, S SIVARAMAN & J D RANADE

Moelwyn-Hughes Parameter of Pure Liquids & Liquid Metal Alloys 209
K P THAKUR & LAKSHMI KANT JHA

EPR & Optical Absorption Studies on the Coordination Compounds of Copper (II) with (3,5-Dimethyl Isoxazole) & (3-Methyl, 5-Phenyl Isoxazole) Ligands ... 212
G PONTICELLI, G PELIZZI, B A SASTRY, S MD ASADULLA & E S CHARY

Relativistic Electronic State of a One-Dimensional System 214
C L ROY, A SINGH & G ROY

Microwave Absorbing Material Using Rubber & Carbon 216
E J ZACHARIAH, K VASUDEVAN, G SREENIVAS, P MOHANAN,
P A PRAVINKUMAR & K G NAIR

Dipole & Quadrupole Polarizabilities & Shielding Factors of Li Using Hydrodynamic Analogy 218
V K TONDON, S K SURI & G C SHUKLA

Stability Measurements in Time Domain Using Dual Mixer Time Difference System 220
G M SAXENA & B S MATHUR

Vibrational Assignments of 2, 3-, 2, 5-, 2, 6-, & 3, 5-Dichloroanilines 223
R K GOEL, S K GUPTA, R M P JAISWAL & P P GARG

Indian Journal of Pure & Applied Physics
Vol. 18, March 1980, pp. 147-149

Computer Simulation of Ternary Miscibility Gap in the Ternray Alloy $Pd_{77.5}$ Cu_6 $Si_{16.5}$

RAHUL BASU*

Mechanical Engineering Division, Indian Institute of Science, Bangalore 560 012

Received 25 *February* 1978; *accepted* 26 *November* 1979

A detailed study has been made to calculate the miscibility gap over a range of temperatures for the metallic glass ternary alloy $Pd_{77.5}$ Cu_6 $Si_{16.5}$, utilizing a suitable computer programme. It has been found that the miscibility gap of interest in this ternary system has a neck at 1500 K rather than the usual gradual variation. The mechanical properties increase disproportionately with the addition of a small proportion of copper. The precipitation of a secondary crystalline phase around 1240°C is postulated. This could produce a dispersed phase composite with interesting high temperature properties.

1. Introduction

In an earlier paper,[1] the author has reported the results of a computer simulation study to calculate the compositional limits in some metallic glasses which are of interest in view of their mechanical properties. The present paper reports a similar computer study to estimate the miscibility gap in $Pd_{77.5}$ Cu_6 $Si_{16.5}$ over a range of temperature.

The amorphous alloy is regarded by many as a super cooled liquid, the liquid structure being maintained by rapidly quenching the alloy. In effect, this can be done in several ways. Duwez[2] has mentioned some of them. Waseda *et al.*[3] have studied the Pd-Si binary combination and analyzed the radial distribution function and compared the solid and liquid phases with regard to the structure. Since the radial distribution functions are very similar, it is concluded that the parameters for the liquid and amorphous phases are also the same, by definition of the Van Laar's parameters e_0, e_p, and e_1. In the present instance, the addition of Cu to the amorphous binary is feasible provided the compositions are within certain limits. Duwez[2] mentions a general formula T_{70-80} G_{30-20} where G is one or more of the metalloid glass formers and T consists of the higher valency elements, notably $3d$ transition elements. A miscibility gap would be expected to exist, heuristically, within this composition range.

2. Analysis

The amorphous phase is treated here as a liquid structure and given the liquid interaction parameter; the secondary crystalline phase is treated as bcc, be it bcc fcc or hcp, since the parameters for fcc and hcp phases are obtained from the bcc parameter by addition of negligible quantities. It may be noted here that the excess free-energy is given, according to Kaufman's analysis[4] as $L\,x\,(1-x)$ for the liquid phase, and $Bx\,(1-x)$ for the solid phase where x is the composition of the binary constituent. The programs listed by Kaufman and Bernstein[4] for the IBM FORTRAN system were adapted to the 360/44 system and applied to the Pd-Cu-Si alloy. Kaufman's method[4] has come in for some criticism in the literature[5] as it is only an approximate treatment (regular solution model), and gives just a vague idea of the actual phase relationships. Various other approaches are possible, and modifications to the excess free-energy relationships can be formulated.[6] However, it was felt that there was sufficient justification to use this approach since the subject is in a very undeveloped stage, in terms of the quantitative concepts. The details of evaluations of the interaction parameters e_0, e_p and e_1 and their approximate numerical values have already been given in the earlier paper.[1]

The quantity e_0 could possibly be different when calculated from calorimetric measurements. However, the data for the rapid quenching (splat cooling) which yields the amorphous states are difficult to measure accurately as this particular transformation is extremely rapid, and the heat transfer consequently is essentially a 'non steady' state process over the surface to surface contact area of the alloy foil (or film) and the quenching surface. Duwez[2] mentions several types of equipment which have been designed for production of amorphous alloys and films. Other methods such as thermal sensors or infrared

* Present address : Gas Turbine Research Establishment, POB 1777, Bangalore 560 075

detection could possibly be applied. It is hoped that such equipment would be available in the near future.

3. Details of Input to the Computer Programme and Calculations

In order to provide the input to the computer, the three binary interaction parameters for the ternary system Pd-Cu-Si were calculated. These were taken to be the parameters for the bcc phase, viz. E_1, E_2 and E_3 where $E_{ij}=L_{ij}+e_1+e_2$ and $L_{ij}=e_0+e_p$ for the liquid phase consisting of binary compound *ij*.

The condition for the miscibility gap is $\partial^2 G/\partial x^2 = \partial^3 G/\partial x^3 = 0$. The summit temperature and compositions are:

$$T_s = \frac{-(E_{jk} + E_{ij} - E_{ik})^2 - 4 E_{jk} E_{ij}}{8 R E_{ik}}$$

$$x_s = \tfrac{1}{2} = x_j \text{ at the summit}$$

$$z_s = \frac{E_{ik} + E_{jk} - E_{ij}}{4 E_{ik}}$$

$$= \Delta E'/4 E_{ik} = z_i \text{ at summit.}$$

The programme MIGAP of Kaufman,[4] when applied to calculate the miscibility limits, solves by the Newton Raphson iteration, the following set of equations:

$$G_i + RT \ln (z_2/z_1) + E_{ij} (x_2^2 - x_1^2) + E_{ik} (y_2^2 - y_1^2) + \Delta E' (x_2 y_2 - x_1 y_1) = 0$$

Similar expressions can be formulated for G_j and G_k by replacing x by $1-x$ and y by $1-y$ respectively.

Various improvements are possible in the expressions for G_i and are described by Spencer.[7] The above expressions could certainly be modified, but without additional empirical data this is not feasible. In the present study, the expressions as given above were kept unchanged, and the Pauling's numbers were utilized to evalute e_0 for the binary combinations of Pd-Cu-Si. The interested reader is referred to Ref. 1 for details. The results of the MIGAP simulation are given in Table 1.

4. Results

The computer results given in Table 1 indicate that the miscibility gap is almost complete over the binary Cu-Si, and from 1000 K onwards it begins to decrease. Around 1500 K, it suddenly levels off and beyond 1500 K, the gap appears again at about the same composition. This suggests a surface for the miscibility gap in T-*xyz* space with a saddle point at the temperature (nearly 1500 K). The other edges were run on the programme and it was found that over the range of 1000-1500 K there was no gap in these binary edges.

Table 1—Edge Solutions on the Cu-Si Edge for Various Temperatures

Temperature (K)	Solution on Cu-Si edge	
1000	0·000	1·000
1100	0·001	0·999
1200	0·001	0·999
1300	0·002	0·998
1400	0·003	0·997
1475	0·004	0·996
1500	NO SOLUTION	
1800	0·010	0·989
2000	0·018	0·981
3000	0·097	0·902

At a high enough temperature, any amorphous alloy would precipitate a secondary phase.[2] This is also true for Pd-Cu-Si alloy. Of particular interest is the unusual effect on mechanical properties, which could compare to a 'dispersion or precipitation' hardening in crystalline lattices. The computer simulation points out possibilities for fabrication of novel composite alloys with unusual high temperature properties. Duwez[2] has mentioned the mechanical properties of Pd_{80} Si_{20} which are as follows: brittle below T_g = 653 K, and a total strain at rupture less than 0·5% with a fracture stress of 136·4 kg/mm². The stress-strain curve is linear up to a stress of 87·3kg/mm². The value of the Young's modulus E is $6{\cdot}8 \times 10^3$ kg/mm². When Cu is added to the binary to form the combination $Pd_{77.5}$ Cu_6 $Si_{16.5}$ the strength of the matrix increases disproportionately. Duwez[2] has illustrated this at various temperatures. For the ternary combination, the stress is proportional to strain up to 1·8% and a stress of 150 kg/mm². Since the former elastic limit for $Pd_{80}Si_{20}$ was 136·4 kg/mm² and the behaviour linear up to 87·3 kg/mm² the linear properties have increased by a factor of 150/87·3 which is nearly 2. The elastic modulus increase in crystalline lattices with only 6% addition is never this high, and this increase in Pd-Cu-Si is remarkable.

5. Discussion

It was found that the miscibility gap of interest in the ternary system $Pd_{77.5}$ Cu_6 $Si_{16.5}$ has a saddle point or neck at 1500 K rather than the usual gradual variation. The mechanical properties increase disproportionately with addition of a small amount of impurity (copper). This is equivalent to doping the compound and corresponding changes in electronic properties are also postulated. Various

experimental tabulations for Pd-Si have given the relevant thermodynamic variables[8-11] such as the heat of crystallization and the glass-temperature T_g. However, the electronic parameters are yet to be studied, and it seems feasible that the electron distributions and type of bonding play a vital role in this type of alloy hardening. Effects of dislocation-precipitate interaction might also prove an interesting topic for further research. It is certain that at the present rate of research, ribbons and wires of glassy metals with strengths over 300,000 lb/in^2 will be commercially available.

Nomenclature

L_{ij} = interaction parameter for the liquid phase consisting of components *i-j*

B_{ij} = interaction parameter for the bcc phase consisting of components *i-j*

E_{ij} = general interaction parameter for components *i-j*

G_i = Gibbs free-energy for system *i*

x,y,z = ternary coordinates

x_s,z_s = summit composition

T = temperature

T_s = summit temperature

References

1. Basu R, *Indian J. pure appl. Phys.*, **18** (1980), 67.
2. Duwez P, *Annl. Rev. mater. Sci.*, No. 8583, **6** (1976), 83.
3. Waseda Y & Masumoto T, *Phys. status Solidi*, (*a*) **31** (1975), 477.
4. Kaufman L & Bernstein H, *Computer calculations of phase diagrams* (Academic Press, London), 1970.
5. Kubaschewsky O & Slough W, *Progress in materials science*, edited by Chalmers (Pergamon Press, Oxford), 1969.
6. Ansara I, *International Symposium on Metallurgical Chemistry*, (National Physical Laboratory, Teddington, UK) 1971, paper 3·2.
7. Spencer P J, *International symposium on Metallurgical Chemistry* (National Physical Laboratory, Teddington, UK), 1971.
8. Chen H S & Turnbull D, *Acta Met.*, **17** (1969), 1021.
9. Chen H S, *Acta Met.*, **22** (1974), 1507.
10. Davies H A & Lewis B G, *Mater. Sci. Engng*, **23** (1976), 179.
11. Chen H S, *Mater. Sci. Engng*, **23** (1976), 151.

Indian Journal of Pure & Applied Physics
Vol. 18, March 1980, pp. 150-158

Transport Properties of Monoclinic Rare-Earth Sesquioxides

B K Verma, Virendra Pratap & H B Lal
Department of Physics, University of Gorakhpur, Gorakhpur 273 001

Received 9 *November* 1978; *accepted* 28 *August* 1979

Measurements on dc and ac electrical conductivity (600 to 1180 K), thermoelectric power (700 to 1100 K) and dielectric constant (300 to 900 K) of pressed pellets of monoclinic (B-type) rare-earth sesquioxides, are reported. It has been concluded that intrinsic conduction in these sesquioxides is of band-type with positive intermediate polaron as the main entity of charge carriers. The energy band gaps of Sm_2O_3, Gd_2O_3 and Tb_2O_3 have been obtained as 2·12, 2·44 and 2·24 eV respectively. Experimental results indicate the onset of ionic conduction particularly in Sm_2O_3 above 1000 K. The slow increase of dielectric constant up to about 750 K and extremely faster increase above this temperature have been attributed to enhanced lattice polarizability and to space charge polarization of thermally generated charge carriers, respectively.

1. Introduction

The rare-earth metal oxides have recently emerged as important high temperature materials and find numerous uses in technical applications. They serve as one of the base materials for the preparation of various compounds [e.g. orthoferrites, chromites, tungstates, molybdates, garnets, etc.]. All the rare-earth elements form sesquioxides which have a variety of phases.[1] However, at room temperature, the stable structures of sesquioxides are hexagonal (A-type), Cubic (C-type) and monoclinic (B-type). Some important parameters regarding the structure of monoclinic rare-earth sesquioxides are presented in Table 1. There have been a lot of studies on pressed pellets regarding the transport properties of $R_{E_2}O_3$ (where R_{E_2} stands for rare-earth elements) with cubic lattice structure[2-13] but no such studies have been reported in literature for the sesquioxides with monoclinic and hexagonal lattice structures. As a part of our study programme of electrical, transport and magnetic properties of 4*f* compounds,[14-19] we have studied the electrical conductivity (ac and dc), thermoelectric power and dielectric constant of all the three monoclinic rare-earth sesquioxides. All these studies have been made on pressed pellets as we failed to melt these oxides to form crystals due to our experimental limitations.

Table 1—Structural Parameters of Monoclinic Rare-Earth Sesquioxides

Sesqui-oxides	Lattice parameters, Å			β	Space group	No. of sites per unit cell
	a	*b*	*c*			
Sm_2O_3	14·177	3·638	8·847	99° 59′	C_{2H}^3	6
Gd_2O_3	14·061	3·566	8·760	100° 6′	C_{2H}^3	6
Tb_2O_3	13·92	3·536	8·646	100° 35′	C_{2H}^3	6

2. Experimental Details

These sesquioxides in powder form with stated purity of 99·99% have been procured from M/s Rare-Earth Products Ltd, England and used as such in our investigation. The powders were fine enough to pass through a grid structure of 600 mesh per square inch. After heating the powders for a few hours at 900 K, they were pressed in the form of pellets (1 to 5 mm thick and area about 0·9 cm^2) at pelletizing pressures ranging from 2×10^6 to 10×10^6 g cm^{-2} using hand-operated hydraulic press and suitable die. These pellets were sintered at a temperature of about 1200 K for more than 20 hr and were kept afterwards in an oven maintained at a temperature of about 500 K. High temperature silver paint was gently applied on the cleaned faces of the pellet to serve as electrodes. All the measurements were made using two-electrode method. The sample holder designed in this laboratory employing quartz as insulator was used for electrical conductivity as well as dielectric constant measurements. The sample holder was kept in a long furnace, where there was practically no temperature gradient. The temperature was raised by increasing the current in the non-inductive windings of the furnace and was measured by chromel-alumel

thermocouple. The dc conductivity of pellets was obtained by measuring current through them using a Keithley digital multimeter type-171. Conductance and capacitance of the pellets at 1·542 kHz were measured using a Weine-Kerr Bridge, USA and at 100 Hz, 1 kHz and 10 kHz using a Systronic LCR bridge (India), type-921. Conductance at 50 Hz and 3 kHz was obtained using a Toshniwal conductivity bridge type-C10/02A (India). The overall accuracy of all these measurements was better than 2%. Thermo-emf (ΔE) was measured using a sample holder very similar to the one used by us earlier[20,21] employing a Keithley digital multimeter type-171 with an internal impedance of 10^{10} Ω to measure ΔE. Sufficient time (~1hr) was given after applying the thermal gradient (ΔT) to get stability before recording the thermo-emf.

3. Results

The density (d_p) and electrical conductivity (σ_p) of the pellets have been measured as a function of pelletizing pressure at a constant temperature. It has been found that d_p and σ_p of pressed pellets increases almost linearly with pelletizing pressure up to a value of $P \sim 3 \times 10^6$ g cm^{-2}. This increase becomes very slow for higher values of P and becomes almost constant for $P \sim 6 \times 10^6$ g cm^{-2}. The density of the highest pressed pellets (d_p) remains slightly less than the theoretical X-ray density (d_0) of the compound. To account for the pore fraction $f = (d_0 - d_p)/d_0$ and to get the crystalline value of the electrical conductivity (σ), correction has been applied using the following relation[22]:

$$\sigma = \sigma_p \left[1 + \frac{f}{1+f^{2/3}} \right] \qquad \ldots(1)$$

Thermoelectric power has been found independent of P, and, therefore, needs no correction regarding the pore fraction. The real part of the dielectric constant of the material (ϵ') has been obtained using another standard relation[23]:

$$\epsilon' = \left(\frac{\epsilon_p^{1/3} - f}{1-f} \right)^3 \qquad \ldots(2)$$

It has also been observed that current density-electric field (J-E) characteristic for the pellets is linear, which indicates that the contact between the electrode and pellet interface is ohmic; σ has also been studied as a function of frequency (0-10 kHz) and the results are shown in Fig. 1. It is observed from this figure that σ does not depend upon frequency at higher temperatures ($T > 700$ K). This result leads us to believe that grain boundary effects are considerably reduced. Also, σ has been found to be independent of heating and cooling cycles; σ has also been found independent of dimensions of the pellets. Further, no significant reduction in electrical current has been observed with time at higher temperatures. This indicates that ionic conduction does not take place in electrical conduction and charge carriers are essentially electrons or holes.

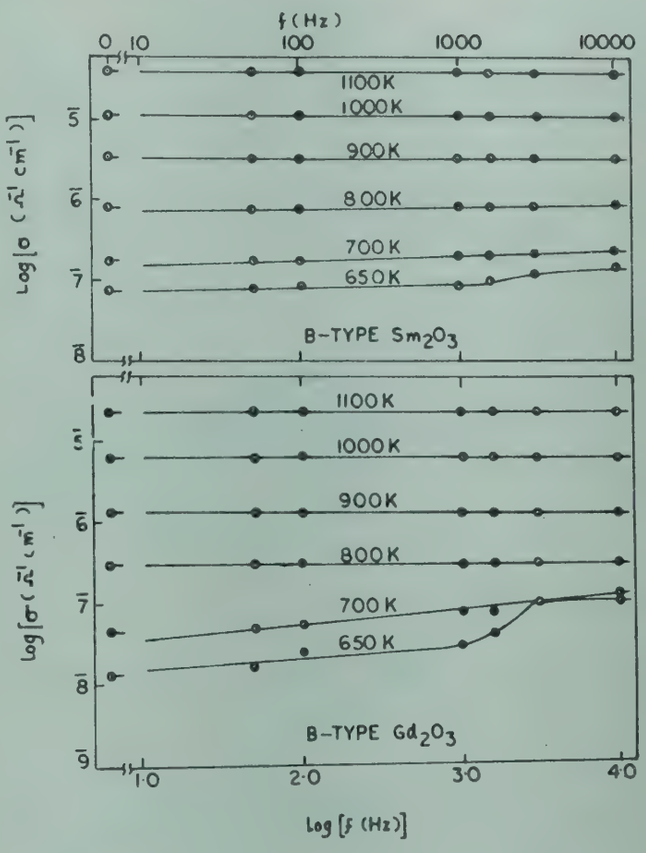

Fig. 1—Variation of logarithm of electrical conductivity (σ_{ac}) with logarithm of frequency (f) at different temperatures for Sm_2O_3 and Gd_2O_3

The variation of log σ_{dc} with $10^3/T$ for monoclinic Sm_2O_3 and Gd_2O_3 and for Tb_2O_3 is shown in Figs. 2 and 3 respectively. In the case of Tb_2O_3, above 900 K, conductivity becomes so large that it cannot be measured accurately by our experimental arrangement. For such high conductivity, lead resistance as well as contact resistance become significant. The values of electrical conductivity vary from 10^{-5} to 10^{-1} Ω^{-1} cm^{-1} in the temperature range studied. This conductivity is much higher in comparison to other sesquioxides in the same temperature range. It is seen from these figures that there is a break of log σ versus T^{-1} plots around 830 K in all materials

$$\sigma = \sigma_{01} \exp\left(-\frac{W_1}{kT}\right) + \sigma_{02} \exp\left(-\frac{W_2}{2kT}\right) \qquad \ldots(3)$$

where σ_{01} and σ_{02} are constants and W_1 and W_2 are activation energies. First term in above equation dominates for temperature $T < 800$ K and second term is more significant for $T > 800$ K. The values of σ_{01}, σ_{02}, W_1 and W_2 for all these sesquioxides are given in Table 2. Fig. 4 shows the variation of thermoelectric power (Θ) with T^{-1} for Sm_2O_3 and Gd_2O_3. The results can be expressed by the relation

$$\Theta = \frac{\eta}{T} + K \qquad ...(4)$$

The values of slope (η) and intercept (K) on Θ-axis in different temperature ranges for Sm_2O_3 and Gd_2O_3, are presented in Table 3. At higher temperatures, Θ values are negative for Sm_2O_3 and Gd_2O_3, indicating the holes as the dominant charge carriers. We could not accurately determine the variation of Θ with T for Tb_2O_3 because we had this material in small quantity. However, it seems that Θ has low and positive values at lower temperatures and low but negative values at higher temperatures.

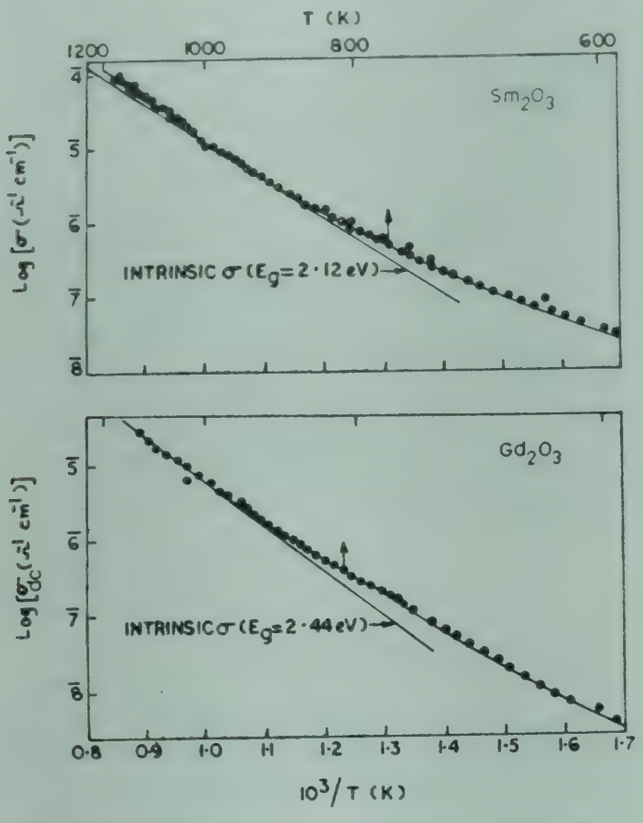

Fig. 2—Variation of log σ_{dc} with inverse of temperature ($1/T$) for Sm_2O_3 and Gd_2O_3

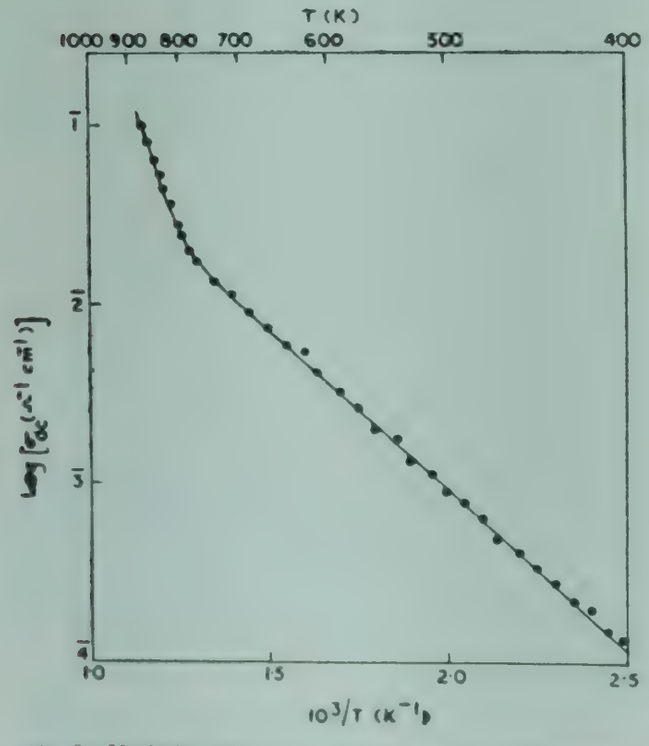

Fig. 3—Variation of log σ_{dc} with inverse of temperature ($1/T$ for Tb_2O_3

4. Discussion

4.1 Energy Band Theory

We will first try to explain our results using the energy band theory. Normally, the energy bands

Table 2—Experimental Values of Pre-exponential Factors and Activation Energies Observed in Electrical Conductivity Expression for Monoclinic Rare-Earth Sesquioxides

Materials	$\sigma_{01}(\Omega^{-1}$ cm$^{-1})$	W_1(eV)	$\sigma_{02}(\Omega^{-1}$ cm$^{-1})$	W_2(eV)
Sm_2O_3	$2{\cdot}71\times10^{-2}$	0·72	2·68	2·12
Gd_2O_3	$2{\cdot}10\times10^{-1}$	0·93	8·75	2·44
Tb_2O_3	3·35	0·35	$3{\cdot}08\times10^{5}$	2·24

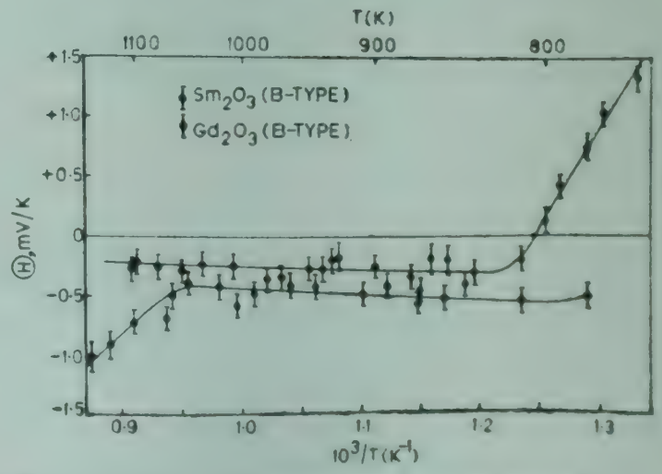

Fig. 4—Variation of thermoelectric power Θ with inverse of temperature ($1/T$) for Sm_2O_3 and Gd_2O_3

Table 3—Values of Slope (η) and Intercept (K) for Sm_2O_3 and Gd_2O_3

Material	η (V)	K (mV/K)	Temperature range	Nature of majority charge carriers
Sm_2O_3	−0·50	+0·07	(800-1050 K)	positive
	+9·20	−9·10	(1050-1150 K)	positive
Gd_2O_3	+16·50	−20·49	(750- 800 K)	negative
	−0·30	+0·50	(800-1100 K)	positive

appropriate for electrical conduction in rare-earth sesquioxides seem to be empty cation $5d$ band, completely filled $2p$ band and partially filled and extremely narrow $4f$ band. High temperature magnetic susceptibility data on rare-earth sesquioxides[24] are compatible with $R_E^{3+} : 4f$ core, which indicates that $4f$ electrons are localized and their contribution to electrical conductivity cannot be significant as they conduct only via hopping mechanism with very small mobility. This essentially leaves empty cation $5d$ and filled $O^{2-} : 2p$ bands as the only appropriate bands for electrical conduction in $R_{E_2}O_3$. The former may be regarded as the conduction and the latter as the valence band. This model, however, will be valid only when the localized $4f^n$ or excited state $4f^{n+1}$ energy levels do not lie within the energy band gap. Isostructural sesquioxides have little variation in their lattice parameters and very little variation in $R_E^{3+} - R_E^{3+}$ and $R_E^3 - O^{2-}$ distances. Thus it is expected that there will not be much difference in the energy band gap of isostructural rare-earth sesquioxides. On the above consideration, the conduction in isostructural sesquioxides can be determined by an energy band model shown in Fig. 5. It is seen from this model that $4f^1$ level for Ce and $4f^2$ level for Pr lie in the energy band gap in $4f^n$ configuration. Probably $Nd^{3+} : 4f^3$ level lies just below E_v. On moving towards the higher members of the series up to R_E=Gd, the $4f^n$ levels fall successively lower in the energies, so that Gd^{3+}: $4f^7$ level is far below E_v. $Tb^{3+} : 4f^8$ level will jump up and may lie slightly below E_v. In case of $4f^{n+1}$ configuration, probably $La^{2+} : 4f^1$ level lies above E_c and these levels for higher members of the series fall successively below this level up to $Eu^{2+} : 4f^7$ but jump to higher energies at $Gd^{2+} : 4f^8$ configuration because eight electron begins to occupy the second half shell with opposite spin. Consequently, the $Eu^{2+} : 4f^7$ level lies below E_c but $Gd^{2+} : 4f^8$ above E_c.

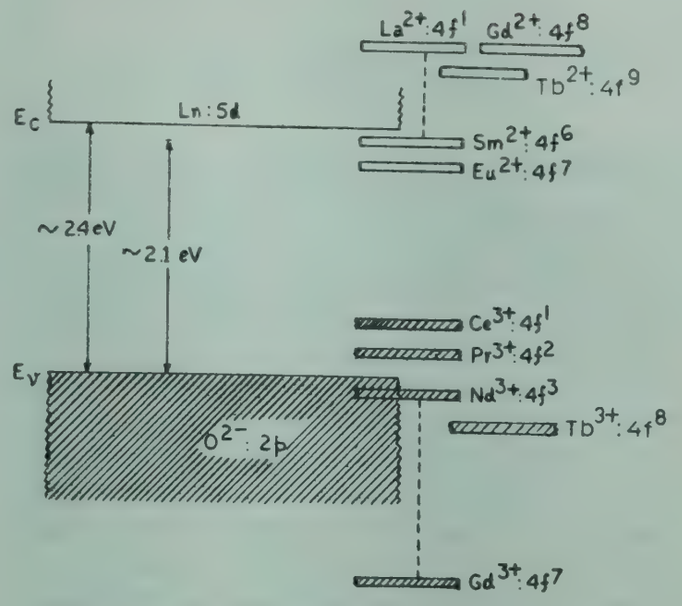

Fig. 5—Schematic energy band diagram for rare-earth oxides

The $Sm^{2+} : 4f^6$ level should lie close to E_c probably just below it. $Tb^{2+} : 4f^9$ level lies much above E_c. On the basis of the above qualitative model, we can discuss the conduction in Sm_2O_3, Gd_2O_3 and Tb_2O_3 in monoclinic structure, studied by us.

In the case of Sm_2O_3, the empty $Sm^{2+} : 4f^6$ levels lie below E_c. Thus electrons from valence ($O^{2-} : 2p$) band, will be first excited to the empty levels giving holes-dominated conduction. Assuming that electrons in $Sm^{2+} : 4f^6$ levels are localized, it is easy to show that electrical conductivity in this solid will be given by the expression[25]:

$$\sigma = e\left[2\left(\frac{2\pi\, m_h\, kT}{h^2}\right)^{3/2} N\right]^{1/2} \exp\left(-\frac{W}{2kT}\right)\left(\mu_h + \mu_e^*\right) + 2e\left(\frac{2\pi kT}{h^2}\right)^{3/2}\left(m_e\, m_h\right)^{3/4} \exp\left(-\frac{E_g}{2kT}\right)\left(\mu_h + \mu_e\right) \quad \ldots(5)$$

where μ^*_e is the mobility of electrons in $Sm^{2+} : 4f^6$ level and $W = E_{4f^6} - E_v$ (energy difference between $Sm^{2+} : 4f^6$ level and top of the valence band) and N the number of rare-earth ions per unit volume. Other symbols have their usual meanings. The first term in the above equation is the contribution of holes in $O^{2-} : 2p$ band, created by the excitation of electrons to the $Sm^{2+} : 4f^6$ level, and the second term is the contribution of thermally excited electrons to $5d$ band and holes left in $O^{2-} : 2p$ band. Since $E_g > W$ and $\mu_h > \mu^*_e$, the above expression can be simplified to:

$$\sigma \simeq A(T) \exp(-W/2kT) \quad ...(6)$$

with

$$A(T) = e\left[2\left(\frac{2\pi m_h kT}{h^2}\right)^{3/2} N\right]^{1/2} \mu_h \quad ...(7)$$

Thus for Sm_2O_3, the plot of log σ versus $1/T$ should be a straight line. The plot of log σ versus T^{-1} has actually been found to be a straight line in the temperature range (830-1180 K). Below 830 K, the slope of the straight line goes down. We assume that intrinsic conductivity in this solid is above 830 K. According to the above theory, the conduction in the intrinsic range of Sm_2O_3 should be hole in O^{2-} : $2p$ band. Experimentally Θ has been found negative in all temperature ranges, indicating the dominance of holes in O^{2-} : $2p$ band. The values of W and the constant $A(T)$ can be determined from the log σ versus T^{-1} plot and knowing the value of $A(T)$, one can evaluate μ_h in terms of m_h. The value of m_h is not exactly known. However, taking $m_h = m$, one can evaluate the order of mobility of the hole (μ_h). On computation, one gets $A(T) = \sigma_{02} = 2{\cdot}68\ \Omega^{-1}\ cm^{-1}$, $W = W_2 = E_{4f}{}^6 - E_v = 2{\cdot}12$ eV and $\mu_h = 8{\cdot}29 \times 10^{-3}\ cm^2/V$ sec at 1000 K.

In the case of Gd_2O_3, both Gd^{3+} : $4f^7$ and Gd^{2+}: $4f^8$ levels do not lie in the band gap. Thus intrinsic conduction in this solid should be due to equal number of electrons in cation $5d$ band and holes in O^{2-} : $2p$ band. There is evidence[26] that R_E^{3+} : $5d$ band in rare-earth solids is narrow in comparison to O^{2-} : $2p$ band. Thus mobility of electrons in $5d$ band will be low in comparison to that of holes in $2p$ band. Hence conduction in Gd_2O_3 should be dominated by holes is O^{2-} : $2p$ band. The negative values of Θ at higher temperatures ($T > 830$ K) indicate that conduction is really dominated by holes in this solid in the intrinsic range. This confirms the validity of the above model according to which, on the above model the log σ and Θ results for Gd_2O_3 should be expressed by the relations[27,28]

$$\sigma = \sigma_0(T) \exp(-E_g/2kT)$$

where

$$\sigma_0(T) = 2e\left(\frac{2\pi kT}{h^2}\right)^{3/2} (m_e m_h)^{3/4} (\mu_e + \mu_h) \quad ...(8)$$

and

$$\Theta = \frac{E_g}{2e}\left(\frac{C-1}{C+1}\right)\frac{1}{T} + 2\left(\frac{C-1}{C+1}\right)\frac{k}{e} + \frac{3}{4}\frac{k}{e}\ln\left(\frac{m_e}{m_h}\right) \quad ...(9)$$

where $C = \mu_e/\mu_h$ and all the other symbols have their usual meanings. These relations predict straight lines, both for log σ versus T^{-1} and Θ versus T^{-1} plots. Figs. 2 and 4 show that both log σ versus $10^3/T$ and Θ versus $10^3/T$ plots are really straight lines for Gd_2O_3 in the temperature range 800-1180K, as expected from theory. Using slope and intercept [$\sigma_0(T)$] of log σ versus T^{-1} and slope (η) and intercept (K) of Θ versus T^{-1} plots, one can evaluate the values of E_g, C and a, using the following relations

$$C = \frac{\mu_e}{\mu_h} = \frac{E_g - 2e\eta}{E_g + 2e\eta} \quad ...(10)$$

and

$$\ln\left(\frac{m_e}{m_h}\right) = \frac{4}{3}\frac{e}{k}\left[K - \frac{2(C-1)}{(C+1)}\frac{k}{e}\right] \quad ...(11)$$

On computation, one gets E_g ($E_c - E_v$) = 2·44 eV, $C = \mu_e/\mu_h = 0{\cdot}605$ and $a = m_e/m_h = 4{\cdot}17$. The effective mass of charge carriers in any band for this solid is not known. However, an estimate of the mobilities of charge carriers can be done by taking the mass of the majority charge carriers (hole in this case) to be equal to the free electron mass. Taking this approximation, one obtains $\mu_h = 7{\cdot}65 \times 10^{-2}\ cm^2/V$ sec and $\mu_e = 4{\cdot}63 \times 10^{-2}\ cm^2/V$ sec at 1000 K.

The case of Tb_2O_3 resembles theoretically that of Gd_2O_3. The $4f^n$ and $4f^{n+1}$ levels do not lie in the band gap. Therefore, the conduction in Tb_2O_3 in the intrinsic range should be due to holes in O^{2-} : $2p$ band. In the absence of Θ versus T^{-1} results, transport parameters for this solid could not be determined. However, on comparing the trend of conductivity results for this material with Gd_2O_3, one can safely say that intrinsic conduction in this material also begins above 800 K and $W_2 = 2{\cdot}24$ eV refers to energy band gap of the solid.

4.2 Carrier Mobilities and Conduction Mechanism in the Intrinsic Range

The mobilities of charge carriers, both in the case of Sm_2O_3 and Gd_2O_3 lie in the range of 10^{-2}-$10^{-3}\ cm^2/V$ sec. We could not determine mobilities in the case of Tb_2O_3; but in view of the conclusion that conduction in this solid too is due to holes in O^{2-} : $2p$ band like others, the values cannot be much different. The usual order of mobility in band conduction is 10 cm^2/V sec or greater. Thus evaluated values of mobilities are two orders of magnitude lower than what one expects from band theory. This lowering of mobility may be due to formation of polarons, which in general leads to high effective mass and low mobilities of the charge carriers. It is quite probable that in these materials the charge carriers are polarons. One of the criteria

for distinguishing the type of polaron is by evaluating the value of dimensionless coupling constant (α) and polaron radius (r_p) by the following relations[29]

$$\alpha = e^2 (m^*/2\hbar^3 \omega_0)^{1/2}/\epsilon_p \qquad ...(10)$$

and

$$r_p = \left(\frac{\pi^2}{\alpha}\right)\left(\frac{2\hbar^3}{m^*\omega_0}\right)^{1/2} \qquad ...(11)$$

where m^* is rigid lattice electron effective mass, ω_0 is longitudinal optical mode frequency and $\epsilon_p = \epsilon_0\,\epsilon_\infty/(\epsilon_0 - \epsilon_\infty)$; ϵ_0 and ϵ_∞ are static and optical dielectric constants respectively. The evaluated values of α, r_p, m_p (polaron effective mass) and W_p (polaron binding energy)[30,31] for Sm_2O_3, Gd_2O_3 and Tb_2O_3 are given in Table 4. It is seen from Table 4 that values of α for all three materials are in the range suited for intermediate polaron (IP). Thus we suggest that IP holes are the main entity of charge carriers in the intrinsic range of these solids. The expressions for mobility and conductivity in the case of IP conduction are given by the following equations[31]:

$$\mu = \frac{1}{2\alpha\omega_0}\,\frac{e}{m^*}\left(\frac{m^*}{m_p}\right)^3 f(\alpha)\exp(-\theta/T) \qquad ...(12)$$

Table 4—Polaron Parameters in O^{2-} : 2p band in the Intrinsic Range of Sm_2O_3, Gd_2O_3 and Tb_2O_3

Temp. (K)	ϵ_0	ϵ_p	α	r_p (Å)	m_p/m	W_p (eV)	$\mu_h \times 10$ (cm^2/V sec)
Sm_2O_3 ($m^* = m_h = m$, $\omega_0 = 1{\cdot}18 \times 10^{14}$ Hz*, $\epsilon_\infty = 3{\cdot}61$*)							
850	136	3·71	3·58	38·58	1·596	0·290	1·17
900	230	3·67	3·62	38·16	1·603	0·294	1·89
950	332	3·65	3·64	37·95	1·606	0·295	1·97
1000	440	3·64	3·65	37·85	1·608	0·296	2·06
1050	675	3·63	3·66	37·74	1·610	0·297	2·13
1100	1000	3·62	3·67	37·64	1·612	0·298	2·20
Gd_2O_3 ($m^* = m_h = m$, $\omega_0 = 1{\cdot}16 \times 10^{14}$ Hz, $\epsilon_\infty = 3{\cdot}61$)							
850	90	3·76	3·56	39·14	1·593	0·283	1·85
900	160	3·69	3·63	38·38	1·605	0·289	1·88
950	266	3·67	3·67	37·96	1·611	0·292	1·94
1000	400	3·64	3·68	37·86	1·613	0·293	2·02
1050	1170	3·62	3·70	37·66	1·616	0·295	2·08
Tb_2O_3 ($m^* = m_h = m$, $\omega_0 = 0{\cdot}92 \times 10^{14}$ Hz, $\epsilon_\infty = 3{\cdot}61$)							
800	1100	3·623	4·13	37·86	1·688	0·263	1·99
850	1300	3·621	4·13	37·84	1·689	0·264	2·10
900	1700	3·618	4·14	37·81	1·690	0·264	2·19

Note: Values of ω_0 and ϵ_∞ are taken from Dulepov *et al.*[38]

and

$$\sigma = \sigma_0(T)\exp\left(-\frac{\hbar\omega_0}{kT} - \frac{E_g}{2kT}\right) \qquad ...(13)$$

where $f(\alpha)$ is unity, $\hbar\omega_0/k$ is characteristic Debye temperature and $\sigma_0(T)$ is an algebraic function of T. If this is taken into account, the values of $W = E_{4f^6} - E_v$ in the case of Sm_2O_3, $E_g = E_c - E_v$ in the case of Gd_2O_3 and $E_g = E_c - E_v$ in the case of Tb_2O_3 become 1·97, 2·29 and 2·12 eV respectively. The evaluated values of μ_h for the three compounds using Eq. (12) are also given in Table 4. These mobilities are of the same order as evaluated experimentally using band theory. This confirms the supposition of IP conduction.

It is seen from Fig. 4 that, at low temperatures, Θ is positive in the case of Gd_2O_3 and has a tendency to become positive in the case of Sm_2O_3. Also Fig. 1 shows that dependence of σ upon frequency starts below 700 K. This frequency dependence of σ indicates that band conduction does not remain significant at lower temperatures. It is obvious to expect dominance of impurity conduction at lower temperatures, and we believe that at lower temperatures the conduction in all these materials is extrinsic. This can arise due to impurities or defects in these solids. All these sesquioxides are only 99·99% pure and thus have a large number of chemical impurities. The most common impurities in rare-earth compounds are the other rare-earths. These isostructural impurities can create deep donor or acceptor centres, whose energy lies within the band gap. These centres can be ionized thermally, and extra charges thereby generated in conduction or valence band, can produce extra conductivity over and above its intrinsic conductivity. The charges localized on impurity sites can also produce extra conductivity by thermally-activated hopping mechanism. The mechanism, which requires lesser energy will be preferred. The other source of extra conductivity may be defects. The existence of oxygen vacancy is well known in oxides.[32] The oxygen ion vacancy in rare-earth sesquioxides can produce two types of defect centres. First $(O^{2-})_v$ (effectively doubly charged oxygen ion vacancy) associated with two R_E^{3+} : e (electron bound to cation site adjacent to oxygen vacancy) and second a centre like $(O^{2-})_v$: 2e (oxygen ion vacancy with two trapped electrons). The centre like $(O^{2-})_v$: 2e can be pictured as solid state analogue of helium. atom. Since (i) oxygen ion vacancy, though has effective positive charge to bind two electrons, does not have a central nucleus like helium atom and

(ii) the dielectric constant of the material is high, hence the binding energy of these electrons to oxygen ion vacancy will be weak. Thus they will form discrete donor levels close to conduction band. Two types of activation energies can be associated with such centres. First, one for exciting the first electron to conduction band and second for exciting the second electron to the conduction band after the first has been excited. These two activation energies are expected to be of the order of 10^{-2} and 10^{-1} eV respectively. Such centres are effective in electrical conduction of oxides only at temperatures lower than 300 K. In the case of first type of centres, the motion of $(O^{2-})_v$ is possible only at higher temperatures usually for $T > 1000$ K. The centres like R_E^{3+} : e can create deep donor centres, which can dominate the electrical conduction in the middle temperature range. We propose that in rare-earth sesquioxides, these R_E^{3+} : e centres, together with deep donor sites created by the chemical impurities, are responsible for electrical conduction in the temperatures range 300-800 K. Among the solids studied, Gd_2O_3 is quite stable. The magnetic susceptibility data of Gd_2O_3 (Ref. 33) is compatible with Gd^{3+} configuration at all temperatures. Therefore, the Gd^{3+} : e centres are less probable and deep traps responsible for σ at low temperatures, may be due to chemical impurities. In Sm_2O_3, there might be significant number of centres like Sm^{3+} : e together with deep donors due to chemical impurities. In the case of Tb_2O_3, magnetic susceptibility data[24] do not yield the value of effective number of Bohr magneton (p) appropriate to Tb^{3+} ions. Also Tb exhibits multiple valence states in its compounds. With oxygen, it forms stable oxides like Tb_2O_3, Tb_4O_7, TbO_2, etc. This fact indicates that one can expect large number of Tb^{3+} : e centres in Tb_2O_3 and they may be primarily responsible for electrical conduction in Tb_2O_3.

4.3 Conduction Mechanism for Extrinsic Charge Carriers

Now let us examine the type of conduction mechanism for these extrinsic charge carriers. For this, a qualitative band diagram for impurity levels shown in Fig. 6 is quite helpful. In case of Sm_2O_3, empty energy level Sm^{2+} : $4f^6$, is above these impurity levels. These are localized levels and any electron excited to this level will become immobile. Thus only way of conduction of these charge carriers is by thermally-activated hopping from one impurity centre to another. The number of charge carriers in such a case is constant. Since $\sigma = ne\mu$, the activation energy coming in the experimental plot of $\log \sigma$ versus T^{-1} is completely associated with mobility. It is also seen

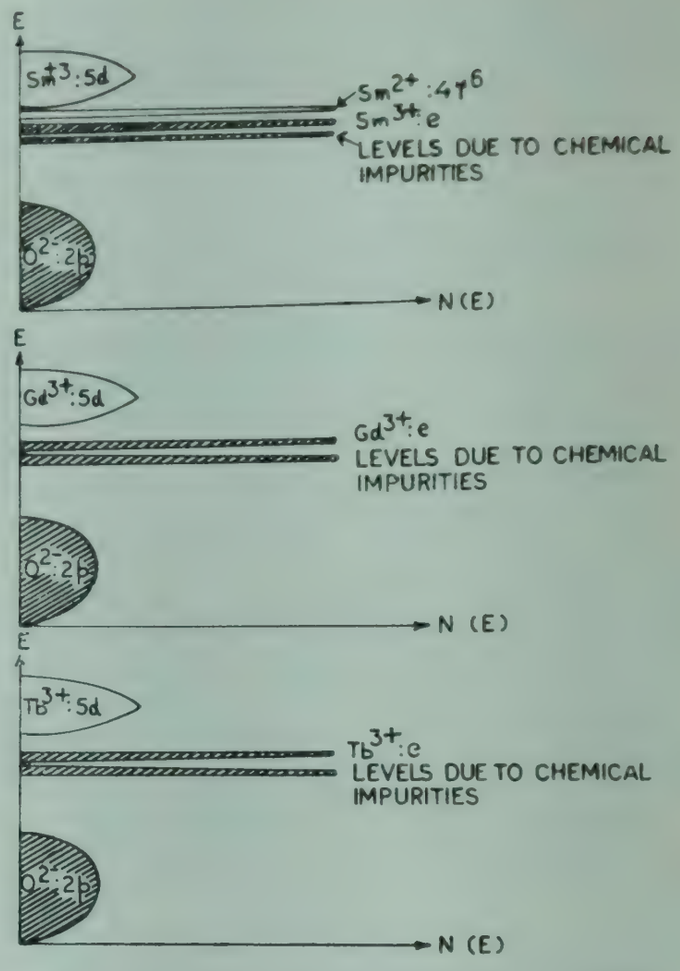

Fig. 6—Qualitative energy band diagram for monoclinic rare-earth sesquioxides

from Fig. 4 that in the case of Sm_2O_3 when $T > 1050$ K, Θ increases much more rapidly. An increase in the slope of $\log \sigma$ versus $10^3/T$ plot above the same temperature (1050 K) is also witnessed in Fig. 2. Perhaps, this is due to the onset of ionic conduction, possibly the motion of $(O^{2-})_v$ centres, which are effectively doubly positive charges, is responsible for this discrepancy. In the case of Gd_2O_3, they can conduct via hopping or band conduction depending on which one involves lower energy. It is seen from Fig. 4 that Θ is positive in the case of Gd_2O_3 at lower temperatures and starts increasing with decrease of temperature. This result indicates thermal generation of charge carriers. Thus extrinsic conduction in Gd_2O_3 is due to electrons in $5d$ band excited from impurity levels. As has been discussed earlier, the electron in $5d$ band will not be a bare electron but will become intermediate polaron. We have evaluated in the case of Gd_2O_3, $m_e/m_h = 4{\cdot}17$ taking $m_h = m$. This gives $m_e \simeq 4m$. Taking this value, we can evaluate α for polaron in $5d$ band using Eq. (10) and once α is known, one can evaluate mobility of charge carriers. The evaluated values of these parameters are given in

Table 5. Since the number of $(O^{2-})_v$ centres is very small in Gd_2O_3, no discrepancy in σ or Θ is appropriate for this solid at higher temperatures. The situation in Tb_2O_3 is the same as that in Gd_2O_3. Here also, conduction can occur by negatively charged polaron in $5d$ band. The evaluated parameters for these polarons are presented in Table 5.

It is seen from Table 5 that values of α are greater than 6 and thus one can expect the formation of small polaron. Since the value of m^* is not known accurately the value of α cannot be known with certainty. Since $5d$ band width is not expected to be less than kT, formation of small polaron is least probable. Hence the estimated values of α bear much error. Also it is believed that for $\alpha \sim 10$, the entity remains as intermediate polaron and conduction is via band mechanism. In any case, α values represent a limiting case in which existence of small polaron is energetically possible. This may be a case of large (intermediate) polaron converting into small polaron as discussed by Tayozawa[34] and Sumi.[35] Thus the conduction in this solid is, however, due to intermediate polarons conducting via band mechanism with some of these converting into stable small polarons, which do not take part dominantly in the band conduction.

Table 5—Polaron Parameters in the Conduction $5d$ Band of Gd_2O_3 and Tb_2O_3

Temp. (K)	ϵ_0	ϵ_p	α	r_p (Å)	m_p/m	W_p (eV)	$\mu \times 10^5$ cm^2/V sec
Gd_2O_3 ($m^*=m_e=4{\cdot}17m$, $\omega_0=1{\cdot}16\times10^{14}$ Hz, $\epsilon_\infty=3{\cdot}61$)							
300	12·60	5·08	5·39	12·66	7·91	0·44	3·55
400	12·65	5·05	5·42	12·59	7·93	0·44	7·34
500	14·00	4·86	5·63	12·12	8·08	0·46	10·40
600	25·94	4·19	6·53	10·45	8·71	0·54	9·62
700	43·00	3·94	6·94	9·83	9·00	0·58	10·13
800	58·00	3·85	7·11	9·59	9·11	0·60	10·17
(Tb_2O_3 $m^*=m_e \cong 4{\cdot}0m$, $\omega_0=0{\cdot}92\times10^{14}$ Hz, $\epsilon_\infty=3{\cdot}61$)							
300	300	3·65	8·20	9·53	4·73	0·56	2·64
400	400	3·64	8·23	9·51.	4·74	0·56	4·70
500	550	3·64	8·24	9·50	4·74	0·56	4·66
600	750	3·63	8·25	9·48	4·75	0·57	8·38
700	975	3·62	8·27	9·46	4·76	0·57	9·84

Note: It is reasonable to take m^*, in the case of Tb_2O_3 to be of the same order as in case of Gd_2O_3 because the conduction is in the same band.

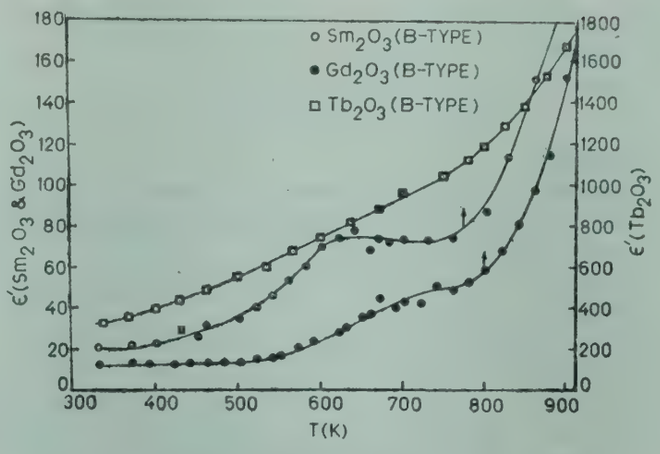

Fig. 7—Variation of dielectric constant (ϵ') with temperature (T) for Sm_2O_3, Gd_2O_3 and Tb_2O_3

Fig. 7 shows the variation of dielectric constant with temperature for all monoclinic rare-earth sesquioxides in the temperature range 300-900 K. When the temperature is increased from room temperature, ϵ' increases slowly with temperature, shows a constancy in the middle temperature range and at higher temperatures it increases at much faster rate. The slow increase of ϵ' at lower temperatures is the net effect of the following factors as discussed by several workers:[36-37]

(i) Electronic polarizability of individual ions increases with increase of temperature due to availability of larger volume owing to expansion of lattice.

(ii) Atomic polarizability also increases due to reduction of forces between the adjacent ions due to expansion of lattice.

(iii) Lattice expansion leads to decrease in the number of polarizable ions per unit volume. The reasons (i) and (ii) lead to increase in ϵ' at the cost of insignificant decrease caused by the reason (iii).

The sesquioxides studied are semiconductors and when temperature becomes high enough, appreciable number of charge carriers are generated whose number increases exponentially with temperature. If these charge carriers are impeded in the bulk of the solid, the space charge polarization builds up and macroscopic field distortion results.[37] And if these charges are not able to discharge at the electrodes, an interfacial polarization results near the solid-electrode interface.[37] Both factors lead to a large increase in ϵ'. These factors are responsible for the rapid increase of ϵ' at higher temperatures.

Acknowledgement

The financial assistance by State Council of Science and Technology, UP, for the work is thank-

fully acknowledged. One of us (VP) is thankful to the CSIR, New Delhi, for the award of a senior research fellowship.

References

1. Brauer G, *Progress in science and technology of rare-earths*, edited by L Eyring (Pergamon press, Oxford), 1966, 312.
2. Foex M, *C. r. hébd. Séanc. Acad. Sci. Paris*, **220** (1945), 369.
3. Noddack W & Walch H, *Z. Phys.*, **211** (1959), 154.
4. Eyring L & Baenziger N C, *J. appl. Phys.*, **33** (1962), 428.
5. Honig J M, Cella A A & Cornwell J C, *Rare-earth research*, Vol. II (Gordon and Breach, New York), 1964, 555.
6. Tare V B & Schmalzried H Z, *Z. Phys. Chem.* (*N F*), **43** (1964), 38.
7. Bogorodistskii P N, Pasynkov V V, Basili R R & Volokobinskii Yu M, *Dokl. Akad. Nauk. SSSR*, **160** (1965), 578.
8. Mehrotra P N, Chandrashekhar G V, Rao C N R & Subba Rao E C, *Trans. Faraday Soc.*, **62** (1966), 3586.
9. Zyrin A V, Dubok V A & Tresvyatskii S G, *Chemistry of high temperature materials*, edited by N A Tarapov, Vol. 10 (1969), 63.
10. Subba Rao G B, Ram Das S, Mehrotra P N & Rao C N R, *J. Solid St. Chem.*, **2** (1970), 377.
11. Naito K, Tsuji T & Une K, *J. Solid St. Chem.*, **10** (1974), 109.
12. Lal H B & Dar N, *Indian J. pure appl. Phys.*, **14** (1976), 788.
13. Lal H B, Pratap V & Dar N, *Indian J. pure appl. Phys.*, **15** (1977), 366.
14. Lal H B, Dar N & Kumar A, *J. Phys.*, C **7** (1974), 4335.
15. Lal H B, Dar N & Kumar A, *J. Phys.*, C **8** (1975), 2745.
16. Lal H B, Dar N & Lundgren L, *J. phys. Soc. Japan*, **41** (1976), 1216.
17. Lal H B & Dar N, *Z. Naturf.*, **30a** (1975), 1783.
18. Lal H B & Dar N, *J. Phys. Chem. Solids*, **38** (1977), 161.
19. Lal H B & Verma B K, *Indian J. pure appl. Phys.*, **15** (1977), 400.
20. Shahi K, Lal H B & Chandra S, *Indian J. pure appl. Phys.*, **13** (1975), 1.
21. Lal H B, Verma B K & Dar N, *Indian J. Cryogenics*, **1** (1976), 119.
22. Russel H W, *J. Am. Ceram. Soc.*, **18** (1935), 1.
23. Loyenga H, *Physica*, **31** (1965), 401.
24. Lal H B, Pratap V & Kumar A, *Pramana*, **10** (1978), 409.
25. Kittel C, *Introduction to solid state physics* (Wiley Eastern, New Delhi), (5th University), Edn, 1977, 235.
26. Wemple G H, Blank S J, Seman J A & Biolsi W A, *Phys. Rev.*, B**9** (1974), 2134.
27. Kittel C, *Introduction to solid state physics*, (Wiley Eastern, New Delhi), (5th University) Edn, 1977, 230.
28. Herman T C & Honig J M, *Thermoelectric and thermomagnetic effects and applications* (McGraw-Hill, New York), 1967, 142.
29. Appel J, *Solid St. Phys.*, **21** (1968), 193.
30. Austin I G & Mott N F, *Adv. Phys.*, **18** (1969), 41.
31. Bosman A J & van Daal H J, *Adv. Phys.*, **19** (1970), 1.
32. Lal H B & Srivastava K G, *Physics Lett.*, **10** (1964), 258.
33. Lal H B & Pratap V, *Indian J. pure appl. Phys.*, **15** (1977), 366.
34. Toyozawa Y, *Prog. theor. Phys.*, **26** (1961), 26.
35. Sumi H, *J. phys. Soc. Japan*, **33** (1972), 327.
36. Smyth C P, *Dielectric behaviour and structure*, (McGraw-Hill, New York), 1955, 132.
37. Von Hippel A R, *Dielectric material and applications* (John Wiley, New York), 1954, 47.
38. Dulepov E V, Batsanov S S & Kustova G N, *J. struct. Chem.*, **13** (1972), 871.

Indian Journal of Pure & Applied Physics
Vol. 18, March 1980, pp. 159-161

Lattice Distortion Spectrum of Evaporated Bismuth Films

SAMAR K SAHA & P C MAHANTA

Department of Physics, Gauhati University, Gauhati 781 014

Received 29 *March* 1979; *revised received* 20 *August* 1979

The temperature variation of electrical resistance of bismuth films, vacuum-deposited at room temperature was observed by heating the films uniformly from room temperature to a maximum temperature of about 230°C. The initial electrical resistance of the films was observed to decrease irreversibly with temperature. The initial lattice distortion energy spectra of the films were determined from the resistance-temperature data. The maximum value of lattice distortion energy function varied from 6×10^{-4} to 21×10^{-4} ohm-cm/eV and the corresponding maximum for decay energy was from 1·10 to 1·34 eV and there was more than one maximum for $F_0(E)_{max}$ and E_{max}. For low thickness range (340 to 958 Å), $F_0(E)_{max}$ was observed to increase with the increase of thickness of the deposits.

1. Introduction

It is well known that the electrical resistivity of vacuum-deposited metallic films is usually higher than the bulk value, and that their initial resistance decays irreversibly on annealing and approaches the resistance of the metal in bulk if the film is heated near to its melting point. The initial high resistivity is due to the presence of lattice distortions caused by a large number of defects frozen in[1] during the atomistic condensation processes in the formation of a vapour-deposited film. If the film is heated uniformly, the rate of decay of resistance will pass through one or more maxima at certain absolute temperatures, each maximum corresponding to a definite number of distortions in the freshly formed film. Thus some understanding of the influence of structural defects on electron transport may be obtained from annealing studies.

Theories of annealing have been proposed by several authors.[2-5] Many workers[6-11] studied the effect of annealing on the electrical properties of different metals and alloys and have determined, using the theory proposed by Vand,[5] the lattice distortion energy spectra of the as-grown films. However, there appears to have been little work of this nature on bismuth films. In the present investigation, bismuth films prepared by vacuum evaporation have been annealed and from the observed changes in their electrical resistance with temperature, the lattice distortion energy spectra of the films have been determined.

2. Experimental Details

Bismuth films were prepared by vacuum deposition of 99·999% pure chips on to clean glass substrates at room temperature at a pressure of about 1×10^{-5} torr. The films were subjected to two cycles of heating and cooling and their resistances were continuously recorded throughout. The maximum temperature reached in both cycles was about 230°C. Specimen temperatures were determined by means of a calibrated copper-constantan thermocouple and Philips dc microvoltmeter GM 6020. The resistance was measured with Marconi Universal Bridge type TF 2700 with an accuracy of ± 2% The heating and the resistance measurements were carried out without breaking the vacuum after the formation of films. The vacuum during annealing was maintained at less than 1×10^{-4} torr. The method of making electrical connections and experimental arrangement was reported earlier in detail by the same authors.[12] The thickness of the films were measured by Tolansky's multiple beam interferometry method.[13]

3. Results and Discussion

Typical variation of the resistance of the films with temperature in both the heating-cooling cycles is shown in Fig. 1. As the temperature is increased, the initial resistance tends to remain unchanged or decrease slowly at the beginning and then begins to fall quite rapidly up to a certain temperature, and then after a sudden decrease, it becomes rather quite

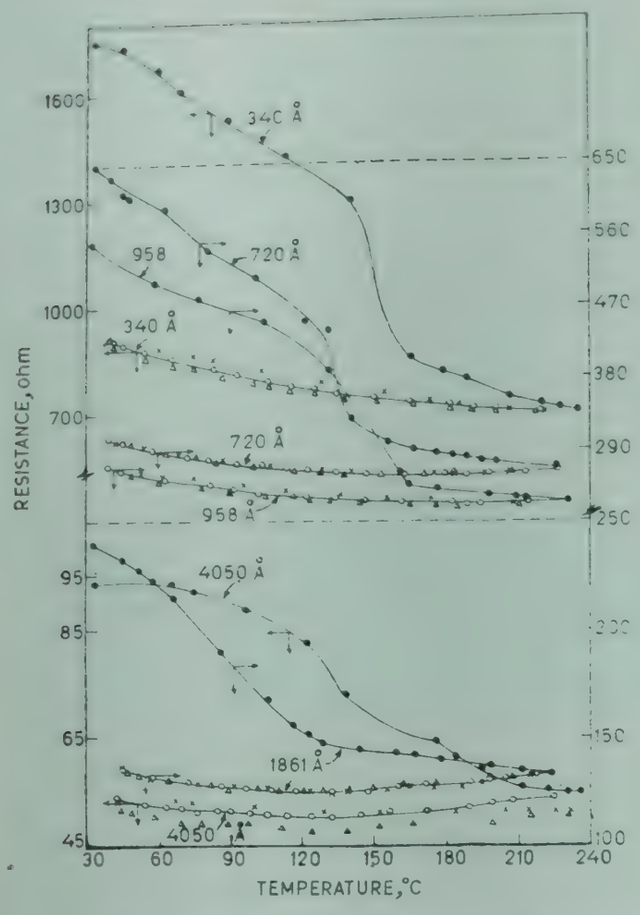

Fig. 1—Resistance versus temperature plots of bismuth films of different thicknesses during heat treatment: closed circles and open circles represent the first cycle of heating and cooling, crosses and triangles represent the second cycle of heating and cooling respectively

slow. This behaviour is in agreement with the well-known fact that during the rise of temperature of the film, the defects are being annealed, resulting in a fall in resistance. It may be noted that in case of annealed bismuth films the resistivity also decreases rather slowly, with increase of temperature, attains a minimum at a particular temperature and then slowly increases.[12] Thus the overall rate of decrease of the resistance in case of a freshly deposited Bi-film is expected to increase upto a certain temperature and then gradually decrease at the higher temperatures. During the cooling process the observed resistivity is only due to the contributions of lattice vibrations, the defect density remaining unaltered below the maximum temperature reached in the cycle. It can be seen that during the second cycle of heating and cooling, the resistance variation with temperature practically coincides with the changes in the cooling branch of the first cycle. This is obviously due to the contribution of the thermal vibrations only since the maximum temperature reached is same as in the first cycle, thus, keeping the defect density unaltered throughout.

Fig. 2 shows the lattice distortion energy spectra of the as-grown films obtained by using Vand's theory, from the resistance versus temperature curve, the temperature being noted at different instants. Vand assumed that the irreversible change in resistance during heating is mainly due to removal of distortions of the 'combined type', that is, vacancies and interstitials in close proximity to one another, which require only very low activation energies for their removal. The defects of this type can have various activation energies. Vand showed that the initial lattice-distortion energy function was,

$$F_0(E) = -(d\rho_i/dT)/kU \quad \ldots (1)$$

where, the decay energy,

$$E = ukT \quad \ldots (2)$$

$d\rho_i/dT$ is the rate of change in the defect resistivity of the film with temperature during the first cycle of heating, k the Boltzmann's constant and U is defined by,

$$U = u(u+2)/(u+1).$$

Here u is given by,

$$u + \log u = \log ct \quad \ldots (3)$$

c being equal to $4fn$, where f is the Debye frequency of the lattice, n the number of atoms which can initiate the decay of a single distortion (estimated to be 10 by Vand), and t is the time taken to reach that particular temperature at which $d\rho_i/dT$ was measured. Thus, $F_0(E)$ and E can be calculated from measurements of $d\rho_i/dT$ at different tempera-

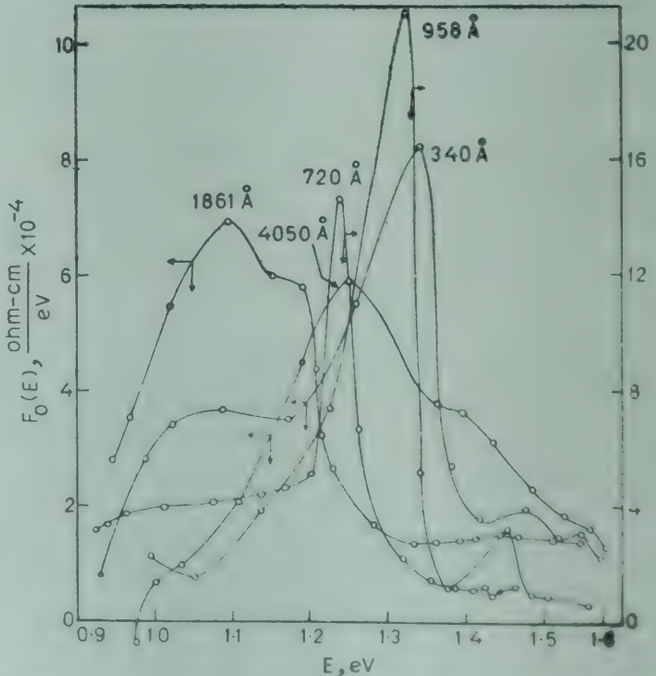

Fig. 2—Initial lattice distortion energy spectra determined from the resistance-temperature data for Bi films of different thicknesses

tures T, and a plot of $F_0(E)$ versus E can be drawn giving the initial distortion energy spectrum.

From the known value[14] of Debye temperature θ_D (= 117 K) = hf/k, the value of c was calculated to be roughly 1×10^{14}, where h is the Planck's constant.

Neglecting size-effect, the overall electrical resistance R is given by,

$$R = R_T + R_i$$

so that,

$$dR_i/dT = dR/dT - dR_T/dT \quad ...(4)$$

where R_T is due to scattering by lattice vibration and R_i is due to scattering by lattice defects. Evaluating dR/dT and dR_T/dT from the irreversible and reversible parts of the curves respectively, dR_i/dT and hence $d\rho_i/dT$ were computed. Finally, a set of values of ct was calculated for the recorded times corresponding to which $d\rho_i/dT$ values were calculated. Then the corresponding values of u and U were calculated by solving Eq. (3) in a computer (TDC-316). The values of $F_0(E)$ were then calculated by using Eq. (1). Evaluating the corresponding decay energy E from Eq. (2), the curve representing the distortion spectrum was obtained.

It is seen from the plots that the distribution function maxima $F_0(E)_{max}$ for the films vary over the range (6 to 21) $\times 10^{-4}$ ohm-cm/eV and the corresponding decay energies E_{max}, vary over the range between 1·095 to 1·339 eV. It is further observed from the plots that the existence of more than one maxima of $F_0(E)$ is indicated. This suggests the existence of more than one preferred value for the decay energy, the lowest being most populated.[7]

Referring to Fig. 2 corresponding to a thicker film of thickness 4050 Å, it is seen that $F_0(E)$ is negative near the room temperature, showing a metallic characteristic. Thus, it indicates that in case of a freshly deposited thicker film, when the temperature is not high enough, the effect of lattice vibration is more than the effect of annealing on the change of resistance of the film with temperature. Similar results were obtained by Das and Jagadeesh[10] in case of thicker Sn-Sb alloy films.

It is seen from Fig. 2 that for lower thickness films (340 to 958 Å) the $F_0(E)_{max}$ increases with the increase of thickness. On the otherhand, in case of thicker films (1861 Å and 4050 Å), Fig. 2 reveals slight decrease of $F_0(E)_{max}$ with increase of thickness. The reported results of the variation of $F_0(E)_{max}$ with thickness differs widely.[6,8] Vand himself states that $F_0(E)_{max}$ and E_{max} should be sensitive to thickness since the density, energy and distribution of defects are controlled by the nature of the substrates in the case of very thin films. For vapour-deposited films, the defect density is greatly influenced by the deposition parameters, especially the deposition rate. Thus, $F_0(E)_{max}$ and E_{max} values are difinitely a function of the deposition rate.[6] Thus unless the deposition rate is maintained constant during deposition, it is not possible to draw definite conclusion about the thickness dependence of the $F_0(E)_{max}$ values. Thus the observed fact in the higher thickness range may be due to the fact that the deposition condition was not held strictly constant.

Acknowledgement

The authors would like to thank Prof. B Chaudhuri, Head of the Department of Physics for providing laboratory facilities and keen interest in this work and S Maheswari for computer programming. One of the authors (SKS) thanks CSIR, New Delhi, for the award of a senior research fellowship.

References

1. Chopra K L, *Thin film phenomena* (McGraw-Hill, New York), 1969.
2. Damaskas A C & Dienes G J, *Point defect in metals* (Gordon and Breach, New York), 1963.
3. Meechan C J & Brinkman J A, *Phys. Rev.*, **103** (1956), 1193.
4. Primak W, *Phys. Rev.*, **100** (1955), 1677.
5. Vand V, *Proc. phys. Soc. Lond.*, 55 (1943), 222.
6. Wilkinson P G & Birks L S, *J. appl. Phys.*, **20** (1949), 1168.
7. Wilkinson P G, *J. appl. Phys.*, **22** (1951), 419.
8. Toyoda H & Nagashima M, *J. phys. Soc. Japan*, **14** (1959), 274.
9. Shah V V & Naik Y G, *Indian J. pure appl. Phys.*, **3** (1965), 20.
10. Das V D & Jagadeesh M S, *Thin solid films*, **24** (1974), 203.
11. Olumekor L & Beynon J, *Thin Solid Films*, **53** (1978), L13.
12. Saha S K & Mahanta P C, *Indian J. pure appl. Phys.*, (sent for publication), 1980.
13. Tolanasky S, *Multiple beam interferometry of surfaces and films*, (Oxford University Press, London), 1948.
14. Furukawa G T & Douglas T B, *American Institute of physics handbook*, Section Eds. Zemansky, M W & Gray D W, (McGraw-Hill, New York), 1957, 4-48.

Indian Journal of Pure & Applied Physics
Vol. 18, March 1980, pp. 162-166

Microtopographical Studies of Second Order Prism Faces of Synthetic Quartz Crystals

M S Joshi & K B Saraf

Physics Department, Sardar Patel University, Vallabh Vidyanagar 388 120

Received 13 *September* 1979

Microtopographical studies of second order prism faces of synthetic quartz crystals grown on *Y*-cut and *Z*-cut seeds are reported. Isolated as well as densely populated parallelogram shaped and also rectangular oriented growth pyramids are illustrated and described. Interaction between neighbouring growth hillocks are illustrated and shown to lead to various growth patterns. Growth around guest microcrystals and modification of growth fronts are reported. Evidence of independent growth on these faces is discussed.

1. Introduction

Quartz crystals have been synthesized by several workers.[1-6] Microtopographical studies of habit faces of natural and synthetic quartz crystals have also been reported by several workers.[7-12] Such studies are very helpful in the understanding of mechanism of growth and development of various habit faces in particular, and of crystals concerned, in general. Occasionally, non-habit faces may also develop on synthetic quartz crystals. Basal planes are almost never found on natural quartz crystals. However, basal planes are found on synthetic quartz crystals. Surface structure studies on basal planes and also on few non-habit faces of synthetic quartz crystals have been reported by Joshi.[13] In spite of vast literature reports on various characteristics of habit faces of natural and synthetic quartz crystals, there is no report so far, to the best of the knowledge of the present authors, on microtopographical studies of second order prism faces of synthetic quartz. Hence, it was thought worthwhile to carry out this work and report about it. Second order prism faces have not been observed and reported on natural quartz crystals. Such faces are, however, found on synthetic quartz crystals. The present work describes microtopographical studies of second order prism faces of synthetic quartz crystals grown in this laboratory by hydrothermal method.

2. Experimental Procedure

Crystal surfaces were thoroughly cleaned with usual reagents. They were then silvered in a vacuum coating unit and then examined under a metallurgical mircoscope.

3. Observations and Discussion

First order prism faces of synthetic quartz crystals exhibit a variety of growth forms. The present paper deals with observations on second order prism faces of quartz crystals grown on *Y*-cut and *Z*-cut seeds.

3.1 Crystals Grown On Y-cut Seeds

Fig. 1 is a photomicrograph showing oriented, rhombus shaped growth pyramids on a portion of second order prism face. Such pyramids are fairly big in size, but few in number. They are observed in isolated regions. They are oriented such that their two opposite sides (one pair) are perpendicular to the *c*-axis of the crystal. The region surrounding such pyramids exhibit horizontal and inclined striations and no other growth forms. Hence, it is conjectured that these pyramids dominate growth in the region of the face where they occur. Growth layers extending and composing such pyramids grow over other initiation centres, if any. Growth fronts of growth layers composing such pyramids manifest themselves as horizontal (perpendicular to *c*-axis) and inclined striations on the face. These inclined striations make an angle of 40° with *c*-axis and 50° with horizontal striations. Existence of these pyramids bears testimony to independent growth on these faces. As against isolated big pyramids shown in Fig. 1, densely populated comparatively smaller oriented parallelogram-shaped growth pyramids are also observed on some prism faces. It is interesting to note that such growth hillocks are found to occur on almost the entire face. This suggests that the number of growth centres is very large and, that

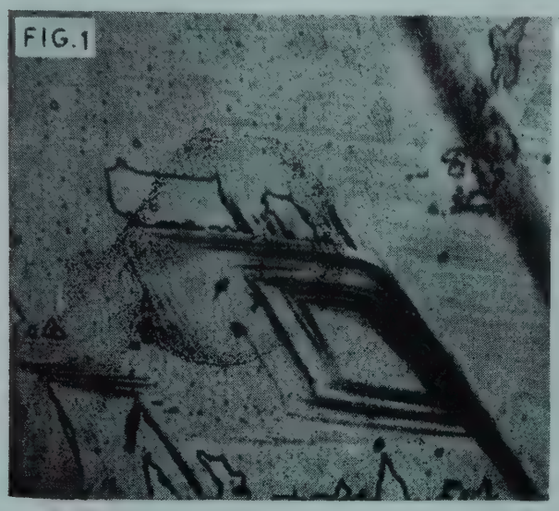

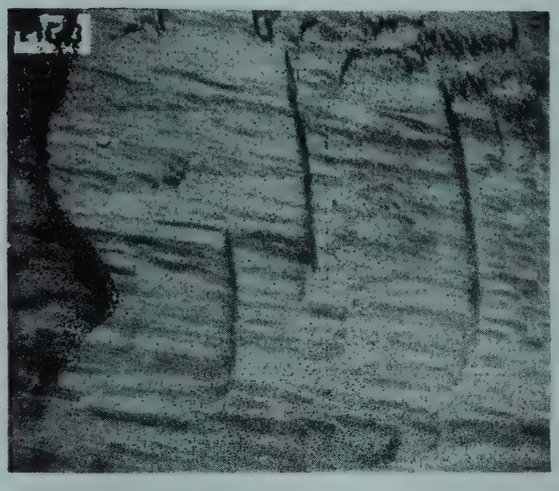

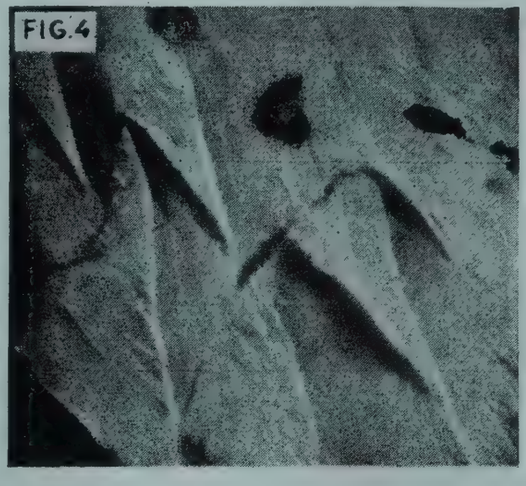

Fig. 1—Rhombus shaped isolated growth pyramid (×230)

Fig. 2—Densely populated small oriented parallelogram shaped growth pyramids (×230)

Fig. 3—Zigzag traces resulting from interaction of very small rectangular growth hillocks (×180)

Fig. 4—Irregular boundaries of interaction of neighbouring growth pyramids (×75)

they all remain active towards the end of growth of the prism face concerned. On account of very close proximity of growth centres of such pyramids, there is intergrowth among neighbouring growth pyramids. Growth fronts of layers composing one pyramid join and fuse with those belonging to the neighbouring ones, thereby giving rise to curved growth fronts which go around from one pyramid to the neighbouring ones. Observations of these pyramids also indicate independent growth on such faces. On faces exhibiting crowded pyramids, practically no region is left to show striations as they are called. Due to intergrowth of neighbouring pyramids, some pyramids look trapizium shaped, but basically they are all parallelogram shaped. Fig. 2 illustrates one case of densely populated growth pyramids described above.

Occasionally, it is found that on some faces a very large number of very shallow and very small rectangular growth hillocks intergrow giving rise to zigzag, mutually perpendicular traces as shown in Fig. 3. These traces, which appear as black lines in the photograph, are vertical cliffs or ledges. Rarely some irregular boundaries of interaction between neighbouring growth forms exhibit traces as shown in Fig. 4. The white (bright) lines in Fig. 4 are ruts.

3.2 Crystals Grown on Z-Cut Seeds

Ample evidence is obtained of independent growth on almost all second order prism faces of crystals grown on *Z*-cut seeds. Growth pyramids on these faces extend further from the growth centres, and growth fronts of growth layers composing growth hillocks are observed to get bunched and thereby form thick layers. They become irregular and corners of growth layers get rounded. Spacing between neighbouring growth fronts is also altered. These growth fronts exhibit themselves as almost vertical and also almost horizontal striations on the prism face. Fig. 5 is a photomicrograph illustrating

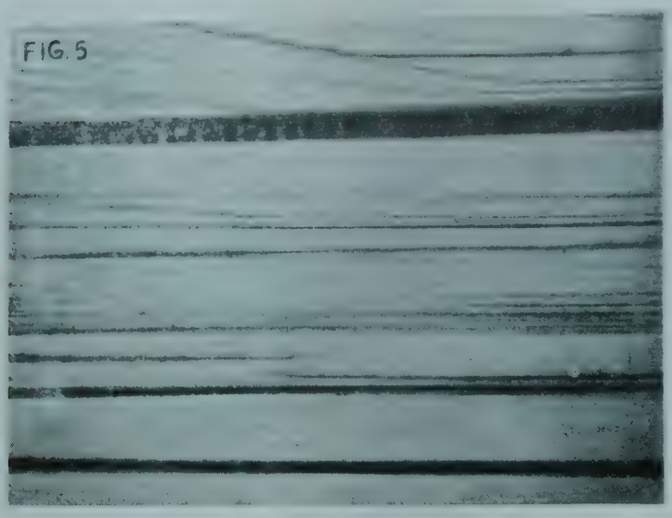

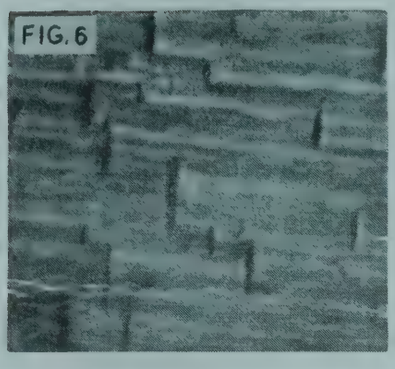

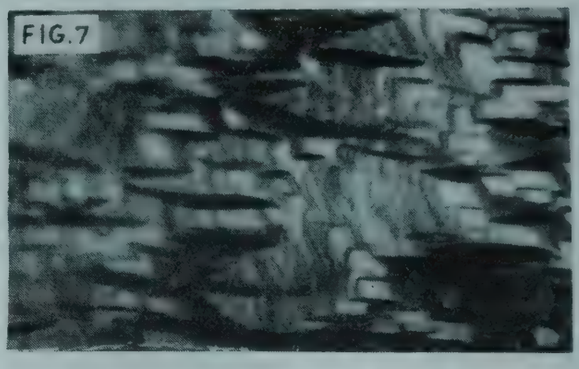

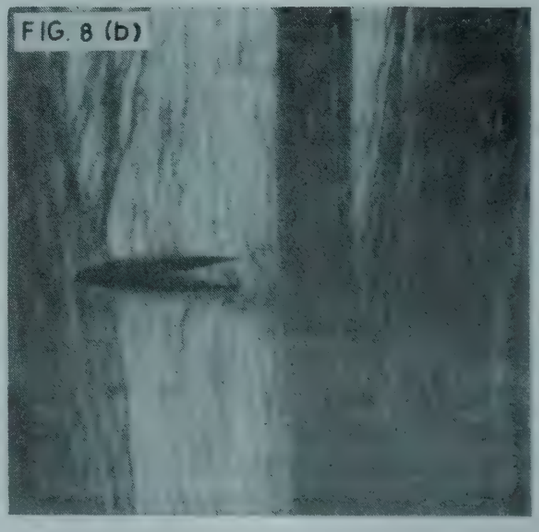

Fig. 5—Horizontal striations illustrating bunching of growth fronts (×50)

Fig. 6—Small shallow closely spaced rectangular growth hillocks (×200) in the region between neighbouring striations of Fig. 5

Fig. 7—Interaction of densely populated strictly oriented parallelogram shaped tiny growth hillocks (×300) in the region between neighbouring horizontal striations of Fig. 5

Fig. 8 (a) & (b)—Modification of growth fronts as they cross some obstacle (×230)

horizontal striations on a portion of a second order prism face. It illustrates bunching of growth fronts. It also shows kinking of growth fronts. Black strips in the photograph are regions which are slightly inclined to the main face. It also represents unequal spacing between neighbouring striations. Some of these striations are straight and smooth but remaining ones are not. When regions between neighbouring striations were examined under high magnifications and studied in detail, they were found to exhibit structures as shown in Fig. 6. This photograph shows that independent growth takes place in

some regions between neighbouring striations in the form of small, shallow, closely spaced rectangular growth hillocks. Interaction between these crowded rectangular hillocks result into zigzag orthogonal line traces as shown in Fig. 6. It is reasonable to say that these rectangular growth pyramids have grown towards the end of growth of the crystal. Some regions between neighbouring striations, shown in Fig. 5, exhibit presence of densely populated and strictly oriented parallelogram shaped small growth hillocks. Some of them are shown in Fig. 7. Here, growth fronts of layers composing the hillocks are clearly visible. Observations reported in Figs. 5, 6 and 7 support our above given suggestion that independent growth takes place on second order prism faces of synthetic quartz crystals. Figs. 8 (a) and 8 (b) show how growth fronts get modified when they meet (as they advance forward) some obstacle in the path of their advance. Here, in Figs. 8 (a) and (b), the horizontal protruding, partly dark structure seems to be an inclusion, the right hand side of which seems to be partly embedded in the body of the crystal. These two figures [Figs. 8 (a) and (b)] also illustrate almost vertical striations which are of course not very smooth and straight.

Microcrystals are found attached on to second order prism faces of synthetic quartz crystals as they do on first order prism faces. Role of microcrystals (attached and detached) has been extensively described and discussed in two papers by Joshi and Kotru.[14,15] Fig. 9 illustrates a noteworthy case of growth around an attached guest microcrystal on a host second order prism face. Here, growth has taken place around a pyramidal termination of an attached guest microcrystal (which appears as a dark cone in the right hand bottom corner of Fig. 9). The resulting growth pyramid is composed of hexagonal well resolved growth layers as seen clearly in Fig. 9. The right half of this hexagonal growth pyramid is not complete because of the existence of some high level structure or cliff which did not allow the right half of growth layers of the pyramid in question to advance.

While growing quartz crystals in an autoclave, by hydrothermal method, it may happen that the temperature gradient may shoot up and/or nutrient may get exhausted. In either case, the growing crystal in the autoclave is susceptible to etching. In such a case, the crystal faces should show evidence of general dissolution of the faces or etch pits on them. In our trial runs to synthesize quartz crystals in our laboratory, we have come across both the situations. In the former case, the face concerned becomes very dull and rough, with practically no

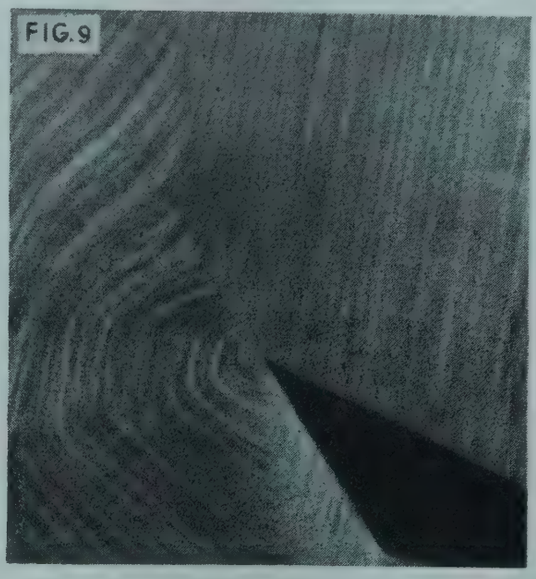

Fig. 9—Growth around a mis-oriented guest microcrystals (×90)

Fig. 10—A big and deep oriented parallelogram shaped etch pit with its longer sides perpendicular to *c*-axis (×65)

reflectivity. If dissolution has advanced substantially, the result is that the face is like a dull, washed-off face. In the latter case, isolated and/or crowded pits are to be expected. In the present work, we have obtained both types of pits. Both types of pits are oriented and, their morphology and other characteristics depend upon several factors and conditions which are uncertain because crystals are inside the autoclave. Fig. 10 illustrates one isolated etch pit. It is one of the big and deep pits. Its longer sides are perpendicular to *c*-axis of the crystal. They are isolated and their number is small, as compared to small and shallow pits. Etch fronts in the right half of the pit are clearly visible. Each such pit is eccentric. The dark region in the pit indicates very great depth of the pit. From the morphology, shape and orientation of such pits, the authors suggest that the pits themselves can be taken to support growth on second order prism faces by spreading and piling up of parallelogram shaped

growth layers. Such pits also support existence of inclined dislocations in the crystal. The former nucleate at the latter.

Acknowledgement

One of the authors (KBS) would like to express sincere thanks to the University Grants Commission, New Delhi, for the award of a teacher fellowship under the Faculty Improvement Programme. He expresses his deep sense of gratitude to the Principal, Pratap College, Amalner, for granting study leave during which this work was done.

References

1. Butuzov V P & Bryatov L V, *Growth of crystals*, Eds. Shubnikov A V & Shiftal N N (Consultants Bureau, New York), **1** (1959), 241.
2. Butuzov V P, Shakhosky G P & Smirnov S P, *Growth of crystals*, Eds. Shubnikov A V & Shiftal N N (Consultants Bureau, New York), **1** (1959), 256.
3. Ballman A A & Laudise R A, *Appl. Phys. Lett.*, **8** (1966), 53.
4. Bandyopadhyay Tarun & Saha Prasenjit, *Res. Ind.*, **11** (1966), 78.
5. Fliestein Jean & Schieber Michael, *J. Cryst. Growth*, **8** (1972), 157.
6. Lias N C, Grudenski E E, Kolb E D & Laudise R A, *J. Cryst. Growth*, **18** (1973), 1.
7. Sunagawa I, *Am. Mineral.*, **49** (1964), 785.
8. Joshi M S, Kotru P N & Vagh A S, *J. Cryst. Growth*, **2** (1968), 329.
9. Joshi M S & Ittyachen M A, *J. Cryst. Growth*, **2** (1968), 47.
10. Joshi M S & Taku R K, *Am. Mineral.*, **57** (1972), 1884.
11. Joshi M S & Paul B K, *Am. Mineral.*, **62** (1977), 122.
12. Joshi M S & Antony A V, *Pramana*, **12** (1979), 251.
13. Joshi M S & Tolansky S, *Proc. R. Soc. A*, **260** (1961), 475.
14. Joshi M S & Kotru P N, *Kristall. Technik*, **11** (1976), 913.
15. Joshi M S & Kotru P N, *Kristall. Technik*, **12** (1977), 13.

Indian Journal of Pure & Applied Physics
Vol. 18, March 1980, pp. 167-170

Optical Study of Magnetic Polarization in Polypropylene

S Asghar Husain & C S Bhatnagar
Department of Physics, Maulana Azad College of Technology, Bhopal-7

Received 17 *May* 1979; *revised received* 11 *July* 1979

An optical study has been made on the effects of magnetic polarization in polypropylene. As a result of this polarization, a change in optical anisotropy was observed in this polymer. Studies on a series of samples (0·25 mm thick) polarized by different magnetic fields (3·25-17·5 kgauss) and forming temperatures (80-140°C) have revealed the dependence of change in optical anisotropy on the forming conditions, and the developed surface charges. An attempt is made to correlate the optical anisotropy with the surface charge. The possible importance of this study in the fields of synthetic fibre technology and applied optics is indicated.

1. Introduction

Following the discovery of 'magneto-electret' (ME) by Bhatnagar[1] in 1964, different properties of a number of electret-forming substances (both inorganic and organic) were investigated. Subsequently an attempt was made to correlate them in a review[2] on magneto-electret, read in an international conference on dielectrics.

The optical properties, however, have not been paid proper attention so far. Earlier work, as reported by Quamara *et al.*[3] on the change in refractive index and that of Fillipova[4] on optical anisotropic effect, yielded encouraging results in understanding the mechanism of electret formation.

The different optical phenomena, such as anisotropy, optical activity, dichroism, etc. are exhibited as a result of particular preferred orientations and properties of the constituent molecules of the substance.[5] A change in any optical property brought about by an external agency (here heat and magnetic field) will yield information about the corresponding change in the molecular arrangement. Here an optical method is adopted to study the change in anisotropy as a result of magnetic polarization in polypropylene.

Several transparent substances can be differentiated as either isotropic or anisotropic depending upon their difference in behaviour when placed between crossed polarizers.[6] Polypropylene in thin sheets (preferably below 1 mm thickness) exhibits the property of anisotropism as confirmed from theory on anisotropism.[7] The polymer in its isotactic form is regular in molecular structure, highly crystalline, non-polar, thermoplast, and having the requisite properties of a good insulator. Softening temperature of the polymer is 100-110°C. Its molecular structure[8] is as shown Chart 1.

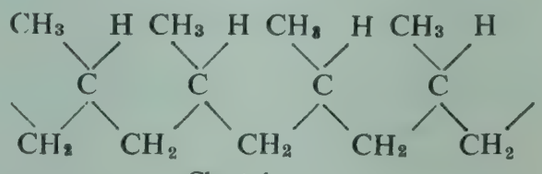

Chart 1

2. Experimental Details

Polypropylene sheet (0·25 mm thick and natural in colour) was procured from M/s Foranco National House, Bombay. The sheet was line-marked (to ensure similar orientation in all samples). Discs of 4 cm diam. were cut from the sheet, cleaned with benzene for any surface contamination and then kept wrapped in metallized paper in order to remove frictional charges. Two series of magneto-electret samples were prepared below and above the softening temperature (100-110°C) of the polymer, following the method of Qureshi and Bhatnagar.[9] The first series consisted of samples prepared at forming temperatures (T_f) 80, 100 and 110°C and the second series at 120, 130 and 140°C, and at each T_f, different forming magnetic fields (H_f) ranging from 3·25 to 17·5 kgauss were used. Blank samples at each T_f were also prepared for comparison, in which heat treatment was the same but no magnetic field was applied. For samples at every forming field the duration of application of magnetic field was 2½ hr (2 hr at constant elevated temperature and ½ hr during cooling to room temperature when the heating was switched off).

Initial surface charge (charge measured just after the preparation of the sample) was measured on both the surfaces of the sample, by the Lindemann electrometer using the lifted electrode method.[10]

The optical anisotropy in the sample disc was studied by an arrangement consisting of a polarizing microscope (Krauss, France) fitted with a photo-

voltaic cell (well shielded from stray light) and a dc microvolt meter type (Philips PP 9004). Monochromatic sodium light was used for the illumination of the microscope stage. The intensity of transmitted light (without the sample) was calibrated to give a constant output (7·0 mV) in the photocell.

The change in optical anisotropy of the disc sample, brought about by the magnetic polarization, was measured in terms of the change in the amount of transmitted light at the maxima (ΔM) and minima (Δm) (each averaged over four observations) as the same disc was rotated slowly between the crossed polaroids both before and after magnetic polarization.

3. Results

All the curves for the samples prepared at and below the softening temperature of the polymer (i.e. for 80-110°C) show a negative change in the percentage variation of transmitted intensity (ΔI) both for the maxima (ΔM) and the minima (Δm), while the curves for the samples prepared above the softening temperature of polymer (i.e. for 120-140°C) show a positive change in ΔM and a negative change in Δm. A representative curve, to illustrate each of the above cases is given in Fig. 1 A for 80°C and in Fig. 1 B for 130°C. As observed from these figures, the magnitudes of ΔM and Δm are more for the samples of the second series as compared to those of the first one. The change in optical anisotropy is maximum for the samples prepared at 130°C.

Figs. 2 A-C show the percentage variation of ΔI at the maxima (ΔM) and minima (Δm) with respect to the different forming temperatures at different

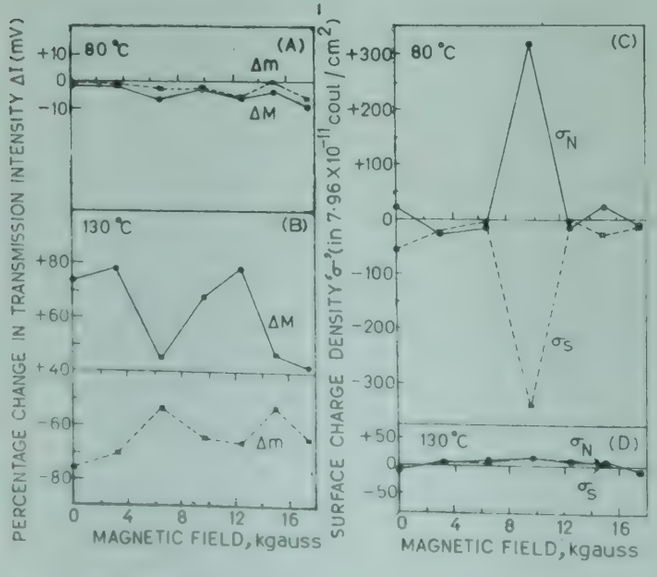

Fig. 1—Variation of percentage change in transmission intensity (ΔI) at the maxima ΔM and at minima Δm with magnetic field at (A) T_f=80 C and (B) T_f=130 C respectively, Variation of surface charge densities (σ_N, σ_S) with forming magnetic field at (C) T_f=80 C and (D) T_f=130 C respectively

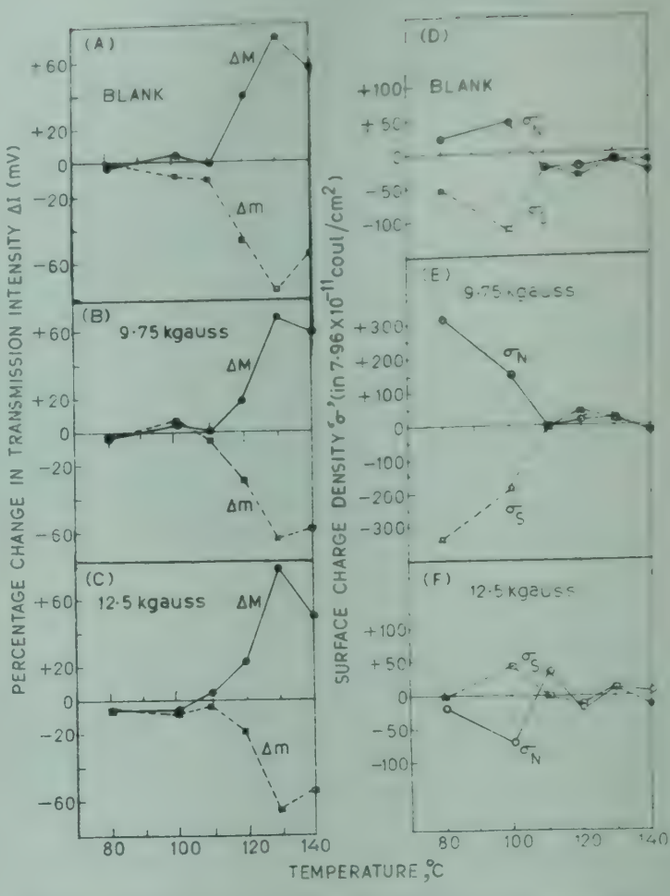

Fig. 2—Variation of percentage change in transmission intensity ΔI at the maxima ΔM and minima Δm with forming temperature at (A) H= 0 gauss, (B) H=9·75 kgauss and (C) H=12·5 kgauss. Variation of surface charge densities (σ_N, σ_S) with forming temperature at (D) H = 0 gauss, (E) H=9·75 kgauss and (F) H=12·5 kgauss magnetic field respectively

forming magnetic fields 0, 9·75 and 12·5 kgauss respectively. In general, all the curves do not show appreciable variation in ΔI up to T_f 110°C, after which it increases, reaching a maximum at 130°C, and then decreases. It can also be seen that the optical anisotropy is more in blank samples than those subjecting simultaneously to heat and magnetic field.

The degree of polarization P which is a measure of optical polarization (and hence anisotropy) was determined using the formula[11]

$$\text{Degree of polarization } (P) = \frac{(I_{max} - I_{min})}{(I_{max} + I_{min})}$$

where I_{max} and I_{min} denote the transmission intensities at the maxima and minima respectively.

The change in the degree of polarization (ΔP), for the samples prepared at different polarizing parameters, with respect to the untreated disc is given in Table 1 from which an analytical assessment of the change in anisotropy can be made. The value of ΔP shows a regular increase with the increase of forming temperature except for samples prepared at 140°C which show a decrease in some cases.

Table 1—Values of ΔP for Different T_f and H_f for Polypropylene Magneto-electrets

H_f	Forming temperature, (T_f) (in °C)					
kgauss	80	100	110	120	130	140
0·0	−0·006	+0·009	+0·042	+0·392	+0·630	+0·486
3·25	−0·003	−0·001	+0·008	+0·336	+0·556	+0·564
6·50	−0·022	−0·009	+0·004	+0·254	+0·410	+0·476
9·75	−0·001	−0·020	+0·021	+0·220	+0·570	+0·511
12·50	−0·002	+0·003	+0·027	+0·189	+0·590	+0·472
15·00	−0·017	−0·008	+0·025	+0·532	+0·446	+0·484
17·50	−0·019	+0·023	+0·032	+0·412	+0·507	+0·547

However, the variation of ΔP with forming magnetic field does not show a regular variation.

Variation of initial surface charge densities σ_N and σ_S (for the sample surface facing the N and S poles of the magnet respectively) with forming magnetic fields, shows a characteristic mirror image type relationship of idiocharge,[9] for the samples prepared below the softening temperature of the polymer, charges being maximum for $H_f = 9{\cdot}75$ kgauss. A representative curve is shown in Fig. 1 C. For the samples prepared above the softening temperature, variation of σ_N and σ_S with H_f is not regular and also does not show the mirror image relationship, as can be seen from Fig. 1 D. The variation of σ_N and σ_S with forming temperature is shown in Figs. 2 D-F for blank and for samples prepared at two different fields 9·75 and 12·5 kgauss respectively. As observed from these figures, the magnitudes of σ_N and σ_S are more in the range of T_f below the softening temperature of the polymer as compared to their magnitudes above the softening temperature. Also the nature of σ_N and σ_S are opposite in the temperature range below the softening temperature of polymer. As can be seen from Fig. 2 E, the magnitudes of σ_N and σ_S are more for the samples prepared with the combined action of heat and magnetic field ($H_f = 9{\cdot}75$ kgauss) in comparison to blank samples [shown in Fig. 2 D], while they are less for samples prepared with $H_f = 12{\cdot}5$ kgauss as shown in Fig. 2 F compared to those of Fig. 2 E for $H_f = 9{\cdot}75$ kgauss.

4. Discussion

4.1 Explanation of Optical Anisotropy

The results presented by Figs. 1 A, B and 2 A-C can be explained as follows. Polypropylene is highly crystalline, as cited in literature.[8] If the molecular crystals are somehow forced to arrange themselves in a particularly preferred and regular pattern then it results in the exhibition of optical anisotropism, as the resistance to light propagation becomes more along the more aligned direction of molecules as compared to the nonaligned direction. The property of anisotropism in the polymer sheet can be attributed to the mechanical stress and strain to which the melt is subjected while rolling sheets from it, resulting in preferential orientation of molecular crystals.[12] As the temperature of the sample disc is increased gradually (during magneto-electret preparation) in the presence of polarizing magnetic field, increased alignment of molecules within the crystal takes place, thus making it easier for them to pack together better. This increases the crystallinity and hence the anisotropy.[13] The molecular chain alignment in magneto-electrets prepared at higher forming temperatures is in conformity with the observation in the case of waxes.[2] Decrease of optical anisotropy at temperatures higher than 130°C may be due to the greater disturbing thermal effects, which decrease the effects of alignment of molecules by the magnetic field.

4.2 Explanation of Charge

The results of Figs. 1 C and D and Figs. 2 D-F showing variations of σ_N and σ_S with H_f and T_f can be explained by the conduction process in the polymer.

It has been established that the conduction process in plastics is ionic rather than electronic. These ions arise from impurity included in the structure, where the impurity includes constituents of different molecular weights.[14] Because of the combined action of heat and magnetic field, microscopic displacement of ions takes place. At the time of cooling, in the presence of magnetic field, these ions get trapped and frozen inside or on the surface of crystallites, giving rise to space charge polarization.[15] This type of polarization contributes to the establishment of idiocharge in non-polar polymers[2] (such as polypropylene). Dipolar polarization is not expected in polypropylene as it is reported to be non-polar.[8] Production of idiocharge (as evident from their mirror image relationship) at the temperatures 80-110°C (below softening temperature) is thus explained. The decrease of charge for samples prepared at 110-130°C (above the softening temperature) can be explained on the basis of increased conductivity at higher temperatures, because, as a result of higher temperature, the movement of ions becomes increasingly fast enough to escape trapping on or inside the crystallites at the time of cooling the sample while preparing the magneto-electret. Hence the surface charge reduces as the temperature increases up to 130°C (surface

charges being least at this temperature). Increase of surface charge for samples prepared above 130°C can be ascribed to a different phenomenon of trapping of charge in magneto-electrets. Because of heat energy, transfer of charges takes place at the metal-polymer boundary. These get trapped and frozen during cooling in the presence of magnetic field, giving rise to increase in surface charge which is predominant in isocharges. Variation of surface charge with magnetic field is rather complex. However, it can be understood by imagining some resonance phenomenon going on within the dielectric, as surmised earlier.[16]

4.3 Correlation of Optical Anisotropy with Surface Charge

The changes in transmission intensity as shown in Figs. 2 A-C can be correlated with the charge densities as shown in Figs. 2 D-F. It is clear that the changes ΔM and Δm are less prominent (hence the optical anisotropy) in the range of temperature 80-110°C (below softening temperature) while the values of the surface charge densities are more in the same range of temperature. At temperatures in the range 110-140°C (above softening temperature), the changes in ΔM and Δm (hence optical anisotropy) are more while the charge densities σ_N and σ_S are less. Thus the changes in anisotropy are oppositely related to changes in charge densities.

Optical property (like thermal and electrical ones) depend upon the behaviour of the constituents of the medium (such as electrons, atoms, ions and molecules). When a light wave propagates through a transparent medium, the photon's energy is shared by the forced oscillations of electrons in the dielectric medium, thus decreasing its own (photon's) energy. The more polarized charges are present, the more will be the attenuation of light intensity. The concentration and mobility of charges determine the transmission of light through a medium. This is in conformity with the maximum light transmission through transparent dielectrics as compared to no transmission through metals.[17] Thus good conductors cannot be transparent.

5. Conclusion

From the above it is concluded that optical anisotropy in polypropylene is maximum for $T_f = 130$°C and $H_f = 12{\cdot}5$ kgauss. These findings can be of some help in the field of synthetic fibre technology as the fibre, in which more molecules are aligned is preferred for commercial use due to its increased strength.[13] Application of proper heat and magnetic field will help in more and more alignment of molecules in a preferred direction.

The investigations can also be useful in the field of applied optics, as two polymer magneto-electret discs showing maximum anisotropy can be arranged in crossed position so as to effectively reduce transmission intensity and hence can work as cheaper polaroids.

Acknowledgement

The authors are grateful to the University Grants Commission, New Delhi, for the award of a Teacher Research Fellowship to one of them (SAH) and also to the Government of Madhya Pradesh for sponsoring him to avail the opportunity. Constant encouragement, cooperation and help rendered by the research colleagues Mr Rudrakant Shrivastava, (Miss) Malini, G Meenakshi, Mr V K Shrivastava and others, are gratefully acknowledged. Thanks are also due to Prof. K A Rao of the Geology Department, M V M Bhopal, for the help rendered by him during the experimental set-up, and to the Principal, M A College of Technology, Bhopal, for providing necessary facilities for research.

References

1. Bhatnagar C S, *Indian J. pure appl. Phys.*, 2 (1964), 331.
2. Bhatnagar C S, Khare M L & Qureshi M S, *A review on Magneto-electret—Extended abstracts*—Workshop on Electric charges in Dielectric, Oct. 1978, Japan, 172.
3. Quamara J K, Khare M L & Bhatnagar C S, *Indian J. pure appl. Phys.*, 14 (1976), 147.
4. Fillipova K V, *Izv. Akad. Nauk. SSSR Ser. Fiz.*, 22 (1958), 843.
5. Skobel'tsyn D V, *Optical methods of investigating solid Bodies—A special research report* (Consultants Bureau, New York), 1965, 3.
6. Hartshorne N H & Stuart A, *Crystals and polarizing microscope* (Edward Arnold, London) 1960, 270.
7. Ditchburn R W, *Light* (Blackie & Sons, London) 1961, 385.
8. Clark F M, *Insulating materials for design and engineering practice* (John Wiley, New York), 1962, 654.
9. Qureshi M S & Bhatnagar C S, *Indian J. pure appl. Phys.*, 10 (1972), 220.
10. Gemant A, *Phil. Mag.*, 20 (1935), 929.
11. Kingslake R, *Applied optics and optical engineering* Vol. I (Academic Press, New York), 1965, 351.
12. Ritche P D, *Physics of plastics*, (D Van Nostrand, New York), 1965, 397.
13. Moncrieff R W, *Man-made fibres*, (John Wiley, New York) 1966, 503.
14. Ritche P D, *Dielectrics & Waves* (John Wiley, New York) 1959, 286.
15. Takamatsu T & Fukada Eiichi, *Rep. Prog. Polym. Phys., Japan*, 15 (1972), 393.
16. Khare M L & Bhatnagar C S, *Indian J. pure appl. Phys.*, 7 (1969), 497.
17. Schmidt A X & Marlies C A, *Principles of high polymer theory & practice* (McGraw-Hill, New York), 1948, 456.

Indian Journal of Pure & Applied Physics
Vol. 18, March 1980, pp 171-175

Massive Spheres : Some General Considerations & Applications

M C Durgapal & A K Pande
Department of Physics, D S B Constituent College, Kumaun University, Naini Tal 263 002

Received 13 *July* 1978

Simple relations for rest-mass density and redshift for cold spherical stars have been obtained. On the basis of these relations, the gravitational binding of Tolman's various models has been calculated. The maximum binding is found to occur when $(P/\rho)_c=1$. Tolman's IV, V and VI solutions have been used to construct neutron star models under the limiting physical condition $dP/d\rho=1$. The well known theorem on chemical potential has been derived in a simple manner. Lastly, Zeldovich's assertion, that a given number of baryons can be arranged in such a manner that the system may have an arbitrarily small energy, has been proved to be erroneous.

1. Introduction

Spherically symmetric and static configurations in general relativity theory were first dealt with in detail by Tolman.[1] Tolman's exact solutions have since then found wide applications in relativistic astrophysics. Oppenheimer and Volkoff[2] used these solutions to calculate mass of neutron stars under extreme conditions of pressure and density, viz. $P=(1/3)\,\rho$. Zeldovich[3] used Tolman's VI solution to show the possibility of conversion of entire rest mass into energy.

Except for Tolman's III solution, it is not known whether these systems are bound or not. In order to estimate the gravitational binding and the energy released during the formation of these configurations, one must find the rest mass density ρ_0 $(=m_B N_B$, where N_B is baryon number density and m_B is the baryon mass). A simple relation for rest mass density for cold stars has been derived in this paper. The formula connects density, pressure, rest-mass density and redshift (or e^{ν}, where ν is general relativistic counterpart of Newtonian gravitational potential). We have calculated rest-mass density, rest-mass and gravitational mass-defect for Tolman's various solutions. These quantities give us a measure of gravitational binding of the configurations. It has been found that these configurations are most tightly bound under the physical condition $P = \rho$.

Some of Tolman's solutions have been written[4] in the form of known equations of state under the extreme causality condition $dP/d\rho=1$. An estimate of the mass of the mass of neutron star has then been made under this condition. The mass comes out to be larger than that estimated by Oppenheimer and Volkoff,[2] using equation of state for degenerate neutron gas and the condition $P = (1/3)\rho$.

Further, it is shown that the theorem regarding chemical potential[5] follows in a simple manner. Moreover, it has also been shown that Zeldovich's deduction[4] of zero coordinate mass is erroneous.

2. Rest-Mass Density

For a static spherically symmetric metric

$$ds^2=e^{\nu}\,dt^2-e^{\lambda}\,dr^2-r^2\,d\theta^2-r^2\sin^2\theta\,d\phi^2 \qquad ...(1)$$

where ν and λ are functions of r only. Einstein's field equations for this metric give[6]

$$dP=-(1/2)\,(\rho+P)\,d\nu \qquad ...(2)$$

Now, for a cold star, we have[7]

$$d\rho_0/\rho_0=d\rho/(\rho+P) \qquad (3)$$

where ρ_0 is the rest-mass density and hence using Eqs. (2) and (3), we get

$$d\rho_0/\rho_0=(d\rho+dP)/[(\rho+P)+(1/2)]\,d\nu \qquad ...(4)$$

or,

$$\rho_0=\text{constant}\times(\rho+P)e^{\nu/2}$$

At $r=a$ (where a = radius of the configuration), $P=0$ and $\rho=\rho_0$. Thus, Eq. (4) becomes

$$\rho_0=(\rho+P)\,e^{(\nu-\nu_a)/2} \qquad ...(5)$$

where ν_a is the value of ν at $r=a$. Eq. (5) can also be written as

$$(1+Z)/(1+Z_s)=(P+\rho)/\rho_0 \qquad ...(6)$$

where Z is the redshift at the point where pressure is P and Z_s is the surface redshift of the configuration. If P_c, ρ_c and ρ_{0c} correspond to the respective quantities at the centre, we have

$$(1+Z_c)/(1+Z_s)=(P_c+\rho_s)-\rho_{0c} \qquad ...(7)$$

Eq. (7) gives a simple relation connecting the central redshift and surface redshift.

The rest-mass density for various Tolman's solutions can be calculated by using relations for P, ρ and e^{ν} from Ref. 6 and 8 to 11 and Eq. (5). The expressions for Tolman's various solutions for ρ_0 are listed below along with other expressions needed for further calculations (we have put $u=m/a$ and $x=r^2/a^2$).

III Solution

$$\rho_0=\rho=\text{constant}$$

$$e^{-\lambda}=1-2ux \qquad ...(8)$$

$$(1+Z)^{-1}=e^{\nu/2}=(3/2)(1-2u)^{1/2}-(1/2)(1-2ux)^{1/2}$$

$$P/\rho=[(1-2ux)^{1/2}-(1-2u)^{1/2}]\,[3(1-2u)^{1/2}-(1-2ux)^{1/2}]^{-1}$$

IV Solution

$$8\pi a^2\rho_0=6u(1-u)(1-3u+ux)^{3/2}/[(1-2u)^{1/2}(1-3u+2ux)^2]$$

$$e^{-\lambda}=(1-ux)(1-3u+ux)/(1-3u+2ux)$$

$$P/\rho=u(1-x)(1-3u+2ux)\,[(1-3u)(2-3u)+ux(3-7u+2ux)]^{-1}$$

$$8\pi Pa^2=3u^2(1-x)(1-3+2ux)^{-1} \qquad ...(9)$$

V Solution

$$b(1+n)\,8\pi a^2\rho_0=2n[1+n(1-n)x^b(1+n)^{-1}]$$

$$b(1+n)e^{-\lambda}=1-n^2x^b(1+2n)^{-1};\quad e^{\nu}=(1-2u)x^n$$

$$b(1+n)\,8\pi a^2\rho=(n/x)[2-n+n(3-n)x^b(1+n)^{-1}]$$

$$b(1+n)\,8\pi a^2P=(n^2/x)(1-x^b) \qquad ...(10)$$

where $n=u/(1-2u)$ and $b=(2n+1-n^2)/(1+n)$

VI Solution

$$q\,8\pi a^2\rho_0=u[(1+q)-(1-q)x^q]x^{-(1+q)/2}$$

$$e^{-\lambda}=1-2u$$

$$4q\sqrt{(2-q^2)}\,e^{q/2}=(1+q)^2x^{(1-q)/2}-(1-q)^2x^{(1+q)/2}$$

$$4\pi a^2\rho=u/x$$

$$(P/\rho)_c=(1-q)/(1+q) \qquad ...(11)$$

where $q^2=(1-4u)/(1-2u)$

VII Solution

$$\rho=\rho_c(1-x)$$

$$e^{-\lambda}=1-ux(5-3x)$$

$$e^{\nu/2}=(1-2u)^{1/2}\cos\tfrac{1}{2}(\omega_1-\omega)-\sqrt{u/3}\sin\tfrac{1}{2}(\omega_1-\omega) \qquad ...(12)$$

$$8\pi P=M\tan\left(\frac{\omega_1-\omega_2}{2}+\beta\right)-N$$

where

$$M=(12u)^{1/2}[1-u(5-3x)x]^{1/2},\quad N=u(5-3x)$$

$$\omega=\ln\left[x-\frac{5}{6}+\left(x^2-\frac{5}{3}x+\frac{1}{3u}\right)^{1/2}\right]$$

(with $\omega=\omega_1$ at $x=1$),

$$\beta=\tan^{-1}[u/3(1-2u)]^{1/2}.$$

Plot of $(P/\rho)_c$ versus u is shown in Fig. 1. The value of ρ_0 can be calculated using Eq. (5).

3. Rest Mass and Binding

A configuration is said to be bound when the rest-mass M is greater than the coordinate mass m (Ref. 3, 7). The binding energy per unit mass, i.e. the total fraction of the rest-mass energy released during the formation of the configuration is given by

$$\alpha=(M-m)/m$$

where $M=\int_0^a 4\pi\rho_0 r^2 e^{\lambda/2}\,dr \qquad ...(13)$

$$m=\int_0^a 4\pi\rho r^2\,dr$$

Values of α for different configurations have been calculated using appropriate values of e^{λ} and ρ_0. The rest mass is calculated by numerical integration for different values of u $(=m/a)$. Fig. 2 shows variation of α with m/a and Fig. 3 shows variation of α with $\tan^{-1}(P/\rho)_c$. $(P/\rho)_c$ is calculated for different u values using Eqs. (8) to (12).

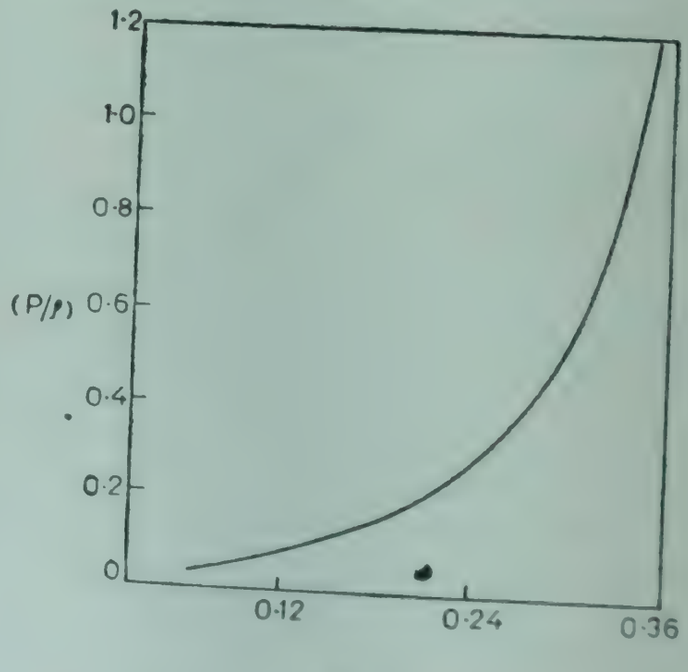

Fig.1—Variation of $(P/\rho)_c$ with u

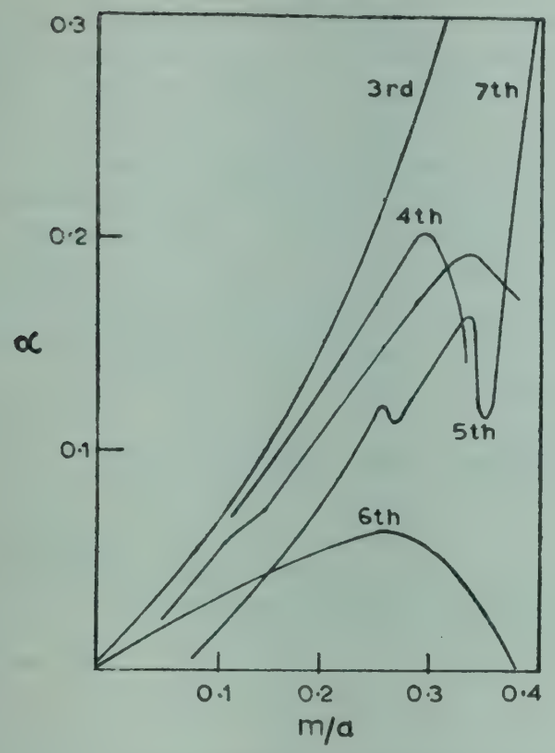

Fig. 2—Variation of α with m/a

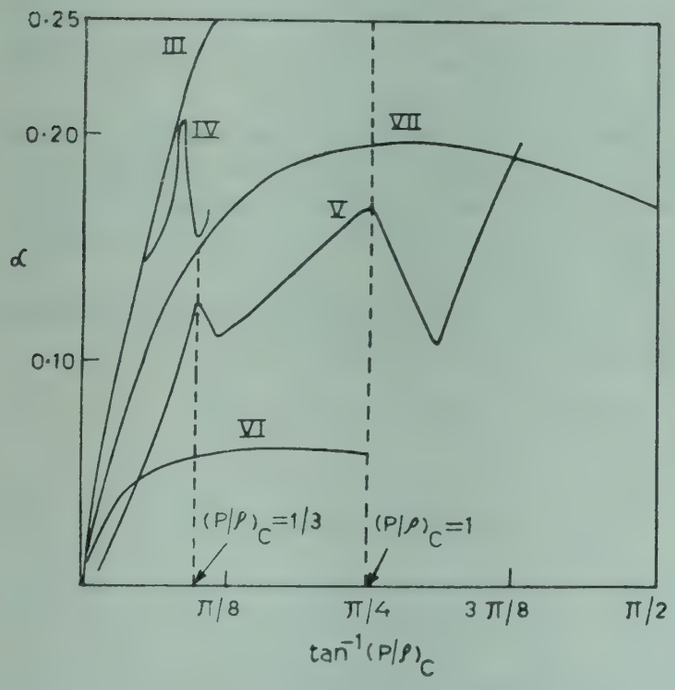

Fig. 3—Variation of α with $\tan^{-1}(P/\rho)_c$

Fig. 3 shows that for configurations pertaining to V, VI and VII solutions, maximum binding occurs when $P_c=\rho_c$. This result is consistent with the casuality condition. The curve for III solution does not show any maximum and the value of α increases monotonically. This is because in a structure of constant density there is no compressibility and $dP/d\rho$ is infinite throughout. IV Solution does not show any maximum at $(P/\rho)_c=1$. This is probably due to the reason that the value of P/ρ in this solution decreases as we move outward from the centre and has a maximum value somewhere between $r=0$ and $r=a$ for $0{\cdot}25 \leqslant u \leqslant 1/3$. Solution V shows a maximum also at $P_c=\rho_c/3$, but this peak is absent in other solutions. Hence, for Tolman's solutions we see that a spherical configuration is most bound for $P_c=\rho_c$.

4. Neutron Star Models

Under the condition $dP/d\rho=1$, Tolman's IV and V solutions can be written as

$$P=4\pi a^2\,\rho_0^2-1/16\pi a^2$$
$$\rho=4\pi a^2\,\rho_0^2+1/16\pi a^2 \qquad \ldots(14)$$
$$P/\rho=(1-x)/(1+x),\ dP/d\rho=1$$
$$P=\rho-1/8\ a^2 \text{ and } a=3\ m$$

while Tolman's VI solution takes the form (near the centre)

$$P=\rho=256\ m^2\ \rho_0^2 \qquad \ldots(15)$$

Eqs. (14) and (15) are now compared with the following standard equations of state corresponding to the condition $dP/d\,\rho=1$.

4.1 Zeldovich's Equation

Harrison *et al*[15]. give

$$P=\rho=4\pi g^2\,(G/c)\,(\hbar/m_\omega c)\,N_B^2 \qquad \ldots(16)$$

where m_ω=mass of the vector meson intermediating the law of repulsion between two baryons separated by the distance r through the equations, interaction energy $=(g^2/r)\ \exp\ (-m_\omega\, c\, r/\hbar)$, and g^2=square of coupling constant.

Breit[12] and Sakurai[13] have shown that the most probable candidate for repulsive interaction is ω-vector meson (m_ω = 782·8 MeV). Green and Swada[14] have estimated $g^2 \simeq 25$ from an average cancellation of vector and scalar interaction. Substituting the values of g^2, m_ω, $\hbar$ and μ_B, Eq. (16) becomes (in geometrized units)

$$P=\rho=(5{\cdot}9\times10^6)^2\ \rho_0^2 \qquad \ldots(17)$$

Comparing Eqs. (14) and (15) with Eq. (17), we get

$$\left.\begin{array}{l} m=3{\cdot}8\ M_\odot \text{ for IV and V solutions} \\ m=1{\cdot}4\ M_\odot \text{ for VI solution} \end{array}\right\} \qquad \ldots(18)$$

4.2 The results obtained by Hagaye *et al.*[15] come out to be $m=3{\cdot}7\ M_\odot$ and $1{\cdot}3\ M_\odot$ respectively.

4.3 Equation of state given by Cazzola *et al.*[16] is $P=0{\cdot}32\times10^{39}\ n_B^2$ (where n_B is number of baryons per fm^3).

In geometrized units, the equation reduces to

$$P=1{\cdot}744\times10^{15}\ \rho_0^2 \qquad \ldots(19)$$

The respective masses come out to be $26{\cdot}6M_{\odot}$ and $10\,M_{\odot}$. These masses are much more than the usually expected values.[17] It may be due to qualitative nature of Cazzola's equation that such a high value for neutron star mass is obtained. However, the results obtained by using Zeldovich's equation and Hagaye's equation are consistent with the accepted values for neutron stars.

5. Chemical Potential

The chemical potential is defined as

$$\mu=(\partial\rho/\partial n)_s=(1/m_B)\,(\partial\rho/\partial\rho_0)_s \qquad ...(20)$$

or,

$$\left.\begin{aligned} m_B &= (\partial\rho/\partial\,\rho_0)_s \\ &= (P+\rho)/\rho_0 \end{aligned}\right\} \qquad ...(21)$$

Eq. (21) is obtained by using Eq. (3). Now using Eq. (5), we get

$$m_B\,\mu = \exp\{(\nu_a-\nu)/2\} = (1+Z)/(1+Z_s) \qquad ...(22)$$

or,

$$m_B\,\mu\,e^{\nu/2} = e^{\nu_a/2} = \text{constant} \qquad ...(23)$$

Eq. (23) shows that the energy gained for addition of each particle is independent of the location of the particle. It is a well known theorem of cold stars and it follows in a simple manner from Eq. (5.)

Usually the equations of state used for construction of a neutron star model include P, ρ and ρ_0 (Ref. 17). Without going to the actual calculations of neutron stars, we can know the nature of chemical potential and hence the ratio $(1+Z_c)/(1+Z_s)$ for the configurations to be constructed on the basis of these equations. Fig. 4 shows the variation of $(P+\rho)\,\rho_0$ and hence that of $(1+Z_c)/(1+Z_s)$ or chemical potential with central density. It is seen that except for Walecka's equation, the value of chemical potential is more or less same for all the equations of state. Probably due to this reason, one gets nearly the same mass of neutron star for these equations. Using the value of surface redshift for Walecka's equation[18] we find that the maximum central redshift from these equations comes out to be, $Z_c=9{\cdot}7$. This value is more than the value obtained by Das and Narlikar[19] ($Z_c=8{\cdot}5$) for an isothermal core with an adiabatically stable envelope.

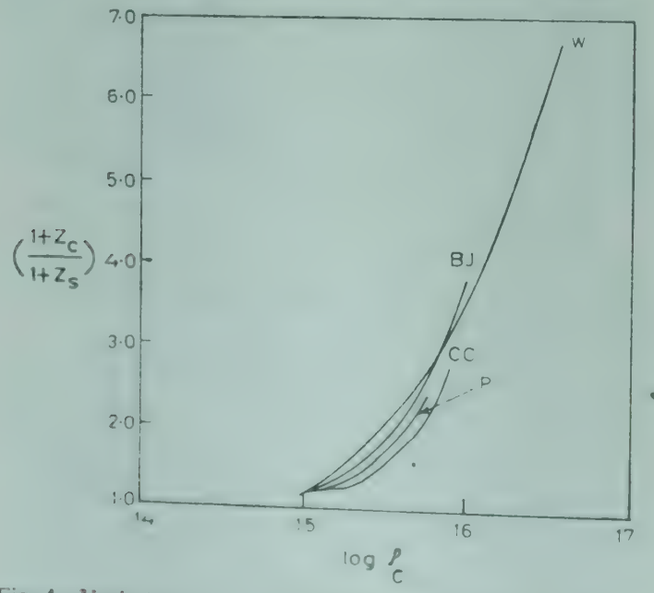

Fig. 4—Variation of $(1+Z_c)/(1+Z_s)$ with control density ρ_c [CC : Canto-Chitre (1972), B-J : Bethe-Johnson (1974), P : Pandhari-pande (1971), W : Walecka (1974) For details, Refer to Arnett and Bowers[18]]

6. Zeldovich's Zero Coordinate Mass

Zeldovich[3] demonstrated that a given number of nucleons N can always be arranged in such a manner that their total energy would be arbitrarily small. For proving this, he assumed that

$$\rho \propto n_B^{4/3} \qquad (24)$$

$$\text{and } \rho \propto 1/r^2 \qquad ...(25)$$

and obtained

$$m=\text{constant}\times N^{2/3}\,u^{1/2}\,(1-2u)^{1/3} \qquad ...(26)$$

He argued that as $u\to 1/2$, $m\to 0$ and the energy produced will be equal to Mc^2.

But, Zeldovich commits a basic error in deriving Eq. (26). In solving Einstein's field equations, one can have only one assumption regarding the equation of state. Choosing two such conditions simultaneously is erroneous.

If one starts with the choice $\rho\propto 1/r^2$ (Tolman's VI solution), one obtains from Eq. (11)

$$M=m_B\,N=3\,m\,(1-2u)^{1/2}/(3-4u)$$

or,

$$m=\text{constant}\times N\,(1-4u/3)/(1-2u)^{1/2} \qquad ...(27)$$

Eq. (27) is the correct equation relating the mass with total number of baryons N for a density distribution $\rho\propto 1/r^2$. This is because Eq. (27) shows that for no physically permissible value of u, the mass tends to ∞.

7. Discussion and Conclusions

(i) For Tolman's solution which have a varying density and in which P/ρ decreases with increasing value of r, (i.e. V, VI and VII solutions), the most bound structures are obtained when $P_c=\rho_c$. The V solution shows an additional maximum for $P_c=(1/3)\,\rho_c$. This maximum is absent in other solutions. Hence, for the cases discusssed in this paper, the condition $P_c=\rho_c$ is more valid for stability than the condition $P_c=(1/3)\,\rho_c$.

(ii) A simple formula relating central redshift with surface redshift has been obtained for cold spherical configurations [Eq. (7)]. Fig. 4, shows the value of $(1+Z_c)/(1+Z_s)$ for different central densities, ρ_c. The maximum central redshift comes out to be 9·7

(iii) The mass of the neutron star under extreme physical condition $dP/d\rho=1$, comes out to be 3·8 $M_\odot$ which is consistent with the accepted values of neutron star mass.[7]

(iv) The theorem of chemical potential follows in a simple manner from Eq. (5).

(v) It has been established that, one cannot arrange a given number of nucleons to get an arbitrarily small value of total energy. This follows from Eq. (27).

Acknowledgement

The authors acknowledge their thanks to the U P State Observatory, Naini Tal, for providing library facilities.

References

1. Tolman R C, *Phys. Rev.*, 55 (1939), 364.
2. Oppenheimer J R & Volkoff G M, *Phys. Rev.*, 55 (1939), 374.
3. Zeldovich Ya B & Novikov I D, *Relativistic astrophysics*, Vol. I (Chicago University Press, Chicago), 1971, 295.
4. Zeldovich Ya B, *Soviet Phys. JETP*, 14 (1962), 1143.
5. Harrison B K, Thorne K S, Wakano M & Wheeler J A, *Gravitational theory and gravitational collapse*, (Chicago University Press, Chicago) 1965, 20.
6. Tolman, R C, *Relativity, thermodynamics and cosmology* (Oxford University Press, London), 1934, 247.
7. Tooper R F, *Astrophys. J.*, **140** (1964), 434.
8. Durgapal M C & Pande A K, *Indian J. pure appl. Phys.*, **17** (1979), 313.
9. Durgapal M C & Gehlot G L, *Phys. Rev.*, **172** (1968), 1308.
10. Gehlot G L & Durgpal M C, *Phys. Rev.*, **D4** (1971), 2963.
11. Durgapal M C & Gehlot G L, *J. Phys.*, **A4** (1971), 747.
12. Breit G, *Phys. Rev.*, **120** (1960), 287.
13. Sakurai J J, *Phys. Rev. Lett.*, 7 (1961), 356.
14. Green A E S & Swada T, *Rev. mod. Phys.*, **39** (1967), 594.
15. Hagaye D, Lee T S M & Cohen J M, *Astrophys. J.*, **201** (1975), 462.
16. Cazzola P, Lucarconi L & Scarinci C, *Nuovo Cim.*, **B43** (1966), 250.
17. Canuto V, *Ann. Rev. Astronom. Astrophys.*, **13** (1975), 355.
18. Arnett W D & Bowers R L, *Astrophys. J.* (Supp.), **33** (1977), 415.
19. Das P K & Narlikar J V, *Mon. Not. R. Astr. Soc.*, **171** (1975), 87.

Indian Journal of Pure & Applied Physics
Vol. 18, March 1980, pp. 176-179

Effect of Polarized Velocity Distribution of Electrons on Double Ionization of He by Proton Impact

VIR SINGH
Physics Institute, Odense University, Denmark

Received 28 *November* 1978; *revised received* 21 *December* 1979

The double encounter theory of M Gryzinski [*Phys. Rev.*, **138** (1965), 305] has been used to calculate double ionization cross-section of He by proton impact. In first encounter, the wavefunction of electron in He is distorted due to the presence of incoming proton. The present work accounts for this polarization effect. The velocity distribution of electron has been obtained by taking the Fourier transform of distorted wavefunction as given by T F M Bonsen and L Vriens [*Physica*, **54** (1971), 318]. For the second encounter, hydrogenic velocity distribution function is used. These results have been compared with the experimental and other theoretical results. It is found that polarization reduces cross-sections at low impact energies, but at higher impact energies no significant change is observed. The variation of the ratio (single ionization cross-section/double ionization cross-section) with incident proton energy is also found improved over the recent calculation of A Kumar and B N Roy [*J. Phys.* **B10** (1977), 3047].

1. Introduction

The ionization of atoms and molecules by proton impact is of importance in a number of areas including plasma physics, astrophysics, upper atmospheric physics and penetration of charged particles through matter. In the recent past, several PWBA, ScA and BEA calculations of single ionization cross-section have been performed by many physicists. Several refinements in PWBA[1-3] and BEA[4-6] theories for single ionization have been given in literature. These modified results are in good agreement with available experimental results and improve the validity of PWBA and BEA theories. On the other hand, very few investigations are available in literature for multiple ionization (especially double ionization) of atoms by proton impact. Theoretical investigations of double ionization of atoms are very much complicated due to the existence of several responsible factors for ionization. Quantum mechanical calculations of double ionization cross-section are very complicated and need a lot of computation and are rare in literature. These complexities can be simplified in the framework of binary encounter theory with some important corrections.

Kumar and Roy[7] have performed calculations of double ionization cross-section for He by proton impact. They have used Gryzinski[8-10] and Vriens[11,12] theories to describe different collision processes. The velocity distribution of atomic electrons plays an important role in these calculations as emphasized by Vriens,[13] Bates and Kingston[14] and Roy and Rai.[15] According to Gryzinski's[10] model, double ionization of atoms may take place in two different ways. In the first process, the two electrons may be ejected from the atom by two successive encounters of the incident proton with the target electrons. Secondly, the incident proton may knock out only one atomic electron and the second electron is removed by the first ejected electron. For the first encounter Kumar and Roy[7] have used the Hartree-Fock velocity distribution of target electrons and the second encounter is described by hydrogenic velocity distribution.

Kumar and Roy's[7] consideration of only Hartree-Fock velocity distribution is not justified because in the presence of projectile, the orbit of target electron is distorted and wavefunction is changed. Due to change of wavefunction, the velocity distribution is also changed. In the present study, we take into account this effect using polarized velocity distribution of electron in He by proton impact as obtained by Bonsen and Vriens.[16] The inclusion of polarization leads to a more accurate analysis of double ionization cross-section.

2. Theory

According to Gryzinski's model if Q_{sc}^{ii} and Q_{ej}^{ii} are cross-sections for double ionization due to the two alternative processes (as described in Sec. 1), the total cross-section for proton impact double ionization is given by

$$Q^{ii} = Q_{sc}^{ii} + Q_{ej}^{ii} \qquad ...(1)$$

where

$$Q_{sc}^{ii} = Y\int_{u_i}^{\Delta E_{max}} \sigma_{\Delta E}(E_q)$$

$$\left(\int_{u_{ii}}^{\Delta E_{max}} \sigma_{\Delta E'}(E_q-\Delta E)\, d(\Delta E')\right) d(\Delta E) \quad ...(2)$$

and

$$Q_{ej}^{ii} = Y\int_{u_i+u_{ii}}^{\Delta E_{max}} \sigma_{\Delta E}(E_q)$$

$$\left(\int_{U_{ii}}^{\Delta_{max}} \sigma_{\Delta E'}(\Delta E)\, d(\Delta E')\right) d(\Delta E) \quad ...(3)$$

with $Y = \dfrac{n_e(n_e-1)}{4\pi\bar{r}^2}$

where n_e is the number of target electrons in a particular shell and $\bar{r}$ is the average radius of the target atom. Kumar and Roy[7] have further simplified Q_{sc}^{ii} and Q_{ej}^{ii} so as to be written as

$$Q_{sc}^{ii} = Y\left(\int_{t=0}^{S_1}\int_{u_i}^{S_2}\left[A\alpha f(t)u_i^{1/2}\right] d(\Delta E)dt\right.$$

$$+\int_{t=0}^{S_1}\int_{S_2}^{S_3}\left[B\alpha f(t)\, u_i^{1/2}\right] d(\Delta E)\, dt$$

$$\left.+\int_{t=S_1}^{\infty}\int_{u_i}^{S_3}\left[B\alpha f(t)\, u_i^{1/2}\right](\Delta E)\, dt\right)$$

$$\times 8{\cdot}797 \times 10^{-17} \quad ...(4)$$

when S_1 is positive
and

$$Q_{sc}^{ii} = Y\left(\int_{t=-S_1}^{\infty}\int_{u_i}^{S_3}\left[B\alpha f(t)\, u_i^{1/2}\right] d(\Delta E)\, dt\right)$$

$$\times 8{\cdot}797 \times 10^{-17} \quad ...(5)$$

when S_1 is negative. The various notations in the above expression are defined as

$$S_1 = S - 1/4S,\ S_2 = 4Su_i(S-t)$$

$$S_3 = 4Su_i(S+t),\ S^2 = v_1^2/v_0^2,\ t^2 = v_2^2/v_0^2$$

where v_1 and v_2 are the velocities of the incident proton and target electron respectively (in atomic units), $f(t)$ is the target electron velocity distribution function. The lengthy expressions for A, B and α have been given by Kumar and Roy,[7] and so we are not giving them here.

The expression for Q_{ej}^{ii} can be written as

$$Q_{ej}^{ii} = Y\left(\int_{t=0}^{S_4}\int_{u_i+u_{ii}}^{S_2}\left[A\alpha f(t)\, u_i^{1/2}\right] d(\Delta E)\, dt\right.$$

$$+\int_{t=0}^{S_4}\int_{S_2}^{S_3}\left[B\alpha f(t)\, u_i^{1/2}\right] d(\Delta E)\, dt$$

$$\left.+\int_{t=S_4}^{\infty}\int_{u_i+u_{ii}}^{S_3}\left[B\alpha f(t)\, u_i^{1/2}\right] d(\Delta E)\, dt\right)$$

$$\times 8{\cdot}797 \times 10^{-17} \quad ...(6)$$

when S_4 is positive
and

$$Q_{ej}^{ii} = Y\left(\int_{t=-S_4}^{\infty}\int_{u_i+u_{ii}}^{S_3}\left[B\alpha f(t)\, u_i^{1/2}\right] d(\Delta E)dt\right)$$

$$\times 8{\cdot}797 \times 10^{-17} \quad ...(7)$$

when S_4 is negative. S_4 may be obtained from following relation

$$S_4 = S-(1+u_{ii}/u_i)/4S$$

and u_i and u_{ii} are the first and second ionization thresholds respectively.

The velocity distribution function $f(t)$ plays an important role as the accuracy of computing double ionization cross-section depends on it. Kumar and Roy[7] have obtained $f(t)$ using Hartree-Fock wavefunction, without considering the effect of projectile on electron wavefunction. This effect is important because, due to presence of projectile the orbit of electron is polarized. We are giving here formulae for polarized $f(t)$ in He by proton impact obtained by Bonsen and Vriens[16] and these have been used to obtain double ionization cross-section. The polarized $f(t,x)$ is given by

$$f(t,x) = N[f_0(t) + (\cos^2\theta\cos^2 x + 1/2\sin^2\theta\sin^2 x)\, f^{pol}(t, r_1)] \quad ...(8)$$

in which the undistorted velocity is given by

$$f_0(t) = \frac{16Z^5}{\pi g^4} \quad ...(9)$$

where $g = t^2 + Z^2$ and the radial part of the distortion is given by

$$f^{pol}(t, r_1) = \frac{4Z}{\pi r_1^4}\left\{\frac{4(t^3+tZ^2)}{g^4}\right.$$

$$+ \exp(-Zr_1)\cos(tr_1)\left[\frac{-4(t^3+tZ^2)}{g^4} + \frac{tr_1^2}{g} + \frac{r_1(2Z^2-t^2)}{g^2} + \frac{r_1(-3t^4-13t^2Z^2+2t^4)}{g^3}\right]$$

$$+ \exp(-Zr_1)\sin(tr_1)\left[\frac{(3t^6+12t^2Z^4-17t^4Z^2-2Z^6)}{Zt^2g^4} + \frac{r_1(-t^4+15t^2Z^2-2Z^4)}{t^2g^3} + \frac{r_1^2(-2t^4-9t^2Z^2-Z^4)}{2Zt^2g^2} - \frac{r_1^3}{2g}\right]\Bigg\}^2 \quad ...(10)$$

In the above expressions t is given in atomic units, $\vec{r}_1$ is the position coordinate of target electron with respect to nucleus, $\cos(\theta) = (\hat{r}_1 \cdot \hat{v}_1)$ and $\cos(x) = (\hat{v}_1 \cdot \hat{v}_2)$. The normalization constant N is given by

$$N^{-1} = 1 + \frac{43}{8Z^6 r_1^4}\left\{1 - \exp(-2Zr_1)\left[1 + 2Zr_1 + 2(Zr_1)^2 + \frac{4}{3}(Zr_1)^3 + \frac{2}{3}(Zr_1)^4 + \frac{28}{129}(Zr_1)^5 + \frac{4}{129}(Zr_1)^6\right]\right\} \quad ...(11)$$

and

$$\int f(\vec{t})\, d\vec{t} = 1 \quad ...(12)$$

as required for each atomic electron.

3. Results and Discussion

The present results of double ionization cross-sections of He by proton impact are shown in Fig. 1. In Eq. (8), we have taken $\cos\theta = 1$, $x = 10°$ and $r_1 = 1$ Å. These results have been compared with the experimental observations of Solov'ev,[17] Wexler[18] and Puckett and Martin[19] and previous theoretical results of Roy *et al.*,[20] and Kumar and Roy.[7] It can be noted from Fig. 1 that present results are in good agreement with experimental results in the middle energy range (80-200 keV). At higher impact energies the present results are very close to the results of Kumar and Roy.[7] At low incident energies the present results are found to be lower than the experimental observations and theoretical calculations. These effects can be explained as follows. At low incident energies, target electrons see a long time presence of proton and the polarization effect is more. Due to this, the cross-section is reduced. But as the energy of proton increases, the polarization effect reduces because target electrons see a short time presence of proton. At higher impact energies (above 1 MeV), the polarization effect is almost negligible and our results are very close to the previous results of Kumar and Roy.[7]

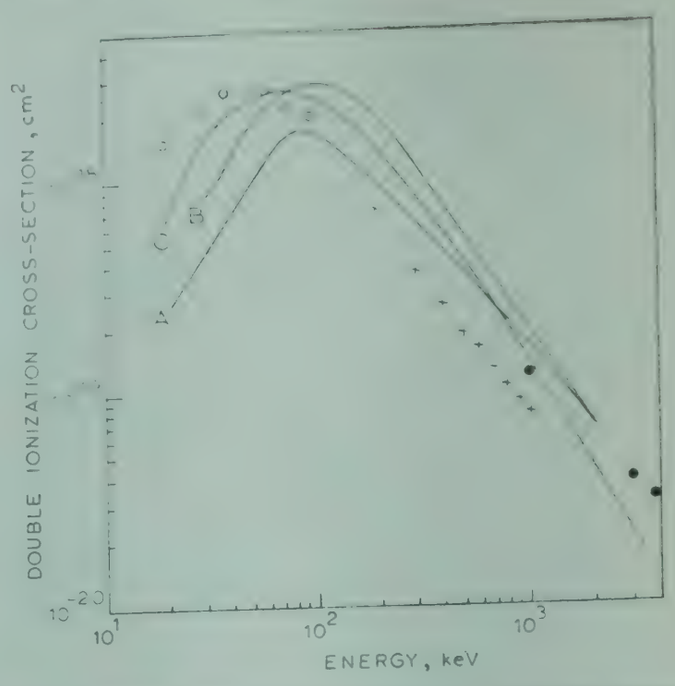

Fig. 1—Proton impact double ionization cross-section versus incident proton energy for He [Theoretical results: Curve A, present results; Curve B, Kumar and Roy[7] Curve C, Roy *et al.*[20]; Experimental results: O, Solov'ev *et al.*[17];, × Puckett and Martin[19]; and ● Wexler[18]]

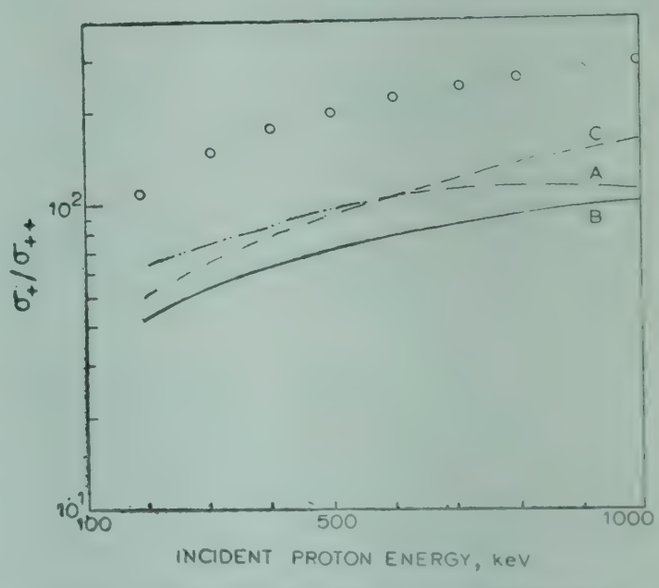

Fig. 2—Variation of the ratio σ_+/σ_{++} for He with incident proton energy [Curves: A, present results; B, Kumar and Roy[7]; C, Roy *et al.*[20]; O, experimental results of Puckett and Martin[19]]

It can also be noted from Fig. 1 that a discrepancy exists among the experimental observations. Some more experimental measurements are needed to resolve these discrepancies. Until these discrepancies are resolved, it is very difficult to testify the

relative superiority of the present and previous results. However, at this juncture, we can say that the inclusion of polarization leads to a more realistic diagnostic tool of the double ionization process. The ratio σ_+/σ_{++} (single ionization cross-section/ double ionization cross-section) has been plotted against incident proton energy and is shown in Fig. 2, along with experimentally observed values of Puckett and Martin.[19] Single ionization cross-sections for He have been culculated by Catlow and McDowell.[21] It can be observed from Fig. 2 that the present results show an improvement over the previous theoretical results.

Acknowledgement

The author is indebted to Dr R P Singhal, Department of Physics and Astronomy, University of Florida, Gainesville, USA for valuable discussions.

References

1. Basbas G, Brandt W & Laubert R, *Phys. Rev.*, A7 (1973), 983.
2. Brandt W & Lapicki G, *Phys. Rev.*, A10 (1974), 474.
3. Carsuo E & Cesati A, *Phys. Rev.*, A15 (1977), 432.
4. Singhal R P & Singh V, *Physica*, 78 (1974), 343.
5. Singhal R P & Singh V, *Physica*, 83C (1976), 200.
6. Singh V, Singhal R P, *Physics Lett.*, 60A (1976), 113.
7. Kumar A & Roy B N, *J. Phys.*, B 10 (1977), 3047.
8. Gryzinski M, *Phys. Rev.*, 138 (1965), 305.
9. Gryzinski M, *Phys. Rev.*, 138 (1965), 322.
10. Gryzinski M, *Phys. Rev.*, 138 (1965), 336.
11. Vriens L, *Proc. phys. Soc. Lond.*, 89 (1966), 13.
12. Vriens L, *Proc. phys. Soc. Lond.*, 90 (1967), 935.
13. Vriens L, *Case studies in atomic collision physics* I, edited by E W McDaniel and M R C McDowell (North-Holland, Amsterdam), 1969, 335-78.
14. Bates D R & Kingston A E, *Advances in atomic and molecular physics* (Academic Press, New York), 6 (1970), 269-318.
15. Roy B N & Rai D K, *J. Phys.*, B 6 (1973), 816.
16. Bonsen T F M & Vriens L, *Physica*, 54 (1971), 318.
17. Solov'ev E S, Il'inn R N, Oparin V A & Fedorenko N V, *Zh. eksp. teor. Fiz.*, 42 (1972), 659.
18. Wexler S, *J. chem. Phys.*, 41 (1969), 1714.
19. Puckett L J & Martin D W, *Phys. Rev.*, A1 (1970), 1432.
20. Roy B N, Tripathi D N & Rai D K, *J. chem. Phys.*, 57 (1972), 3904.
21. Catlow G & McDowell M R C, *Proc. phys. Soc. Lond.*, 92 (1967) 875.

Indian Journal of Pure & Applied Physics
Vol. 18, March 1980, pp. 180-182

Coincidence Studies of ^{144}Ce With Improved Detection System*

R K MISHRA

Department of Physics, Magadh University, Bodh-Gaya, Bihar

Received 18 *September* 1978; *revised received* 24 *July*, 1979

Coincidences of ^{144}Ce were measured with e-γ and e-e coincidence techniques. Closely spaced low energy gamma transitions of ^{144}Pr have been well resolved. Our measurements indicate slight evidence of a weak satellite of 33·53 keV gamma ray. The proposed decay scheme of ^{144}Ce based on these measurements is also given.

1. Introduction

The ^{144}Ce nucleus has a half-life of 285 days and decays by the emission of low energy β- and γ-rays to the ground state of ^{144}Pr which further decays to ^{144}Nd with a half-life of 17·5 min by emitting β- and γ-rays. The level structure of ^{144}Pr has been studied by various workers and different decay schemes of ^{144}Ce were proposed by them.[1-7] The disagreement remains over the existence of the upper level of ^{144}Pr (166 keV) and its possible decay mode. Several workers[1,4-6] proposed that a weak γ-ray (166 keV→133·53 keV transition) may be present close to the well established γ-ray of 33·57 keV whose intensity has been estimated by Geiger, Graham and Ewan to be $2{\cdot}3 \times 10^{-3}$ photons per disintegration. The 33·57 keV gamma is difficult to separate from the K_α X-ray of ^{144}Pr at 35·55 keV. The e-γ, e-e and γ-γ coincidence techniques were applied by many workers[1-6] in the studies of the decay scheme of ^{144}Ce. The detectors, they used were mainly NaI (Tl) scintillator and magnetic β-spectrometer. The estimated resolution of their detection system[2,3] was not better than 33% at 35·55 keV X-ray of ^{144}Pr and the best resolving time of their coincidence system was 2 sec. Therefore, reinvestigation of the 166 keV→133·53 keV transition seems desirable. The present experiment used a high resolution Ge(Li) X-ray detector (FWHM 290 eV at 14 keV) in conjunction with avalanche transistor discriminator and the time pick-off unit in our coincidence channel. The estimated resolution of our detection system with associated electronics is around 2% at 35·55 keV. A considerable improvement in our detection system was made by using a fast 56AVP photomultiplier, NE104 A plastic scintillator, available transistor discriminator and equiangular spiral light guide. The performance of the last two component units is described by Mishra.[7,8]

2. Experimental Procedure

2.1 The e-γ Coincidence

Our e-γ coincidence system consists of a Ge(Li) detector associated with circuitry in conjunction with a prolate spheroidal field β-ray spectrometer. The β-source of ^{144}Ce was prepared by the electrospraying method[9] and the source diameter was 6 mm (Ref. 10). The spectrum obtained by our Ge(Li) X-ray detector [Figs. 1(a) & 1(c)] shows a partial resolution of the 33·57 keV gamma ray together with K_α X-rays and several Ge-escape peaks. In order to measure the coincidences, the spectrometer was focussed on the conversion line and the Ge(Li) spectrum was scanned over the multichannel analyzer. The resolving time of our coincidence system was $2\tau = 34$ nsec and the chance coincidence rate was of the order of 10^{-3} counts per sec.

Fig. 1(b) shows the coincidence spectrum when the beta spectrometer was focussed on the conversion line of L_1 40·93. An expected enhancement of 33·57 keV γ-ray indicates that the γ 40·93 is in coincidence with γ 33·57. No such enhancement is observed near 33·57 keV in the coincidence spectrum when the spectrometer was focussed on the K 133 53 [Fig. 1(d) inset].

2.2 The e-e Coincidence

If the 166 keV → 133·53 keV transition is very weak, it could be a strongly converted transition. Development of our fast detection system made it of interest to search for the above transition by measuring the coincidence between the conversion electrons of 133·53 keV and 33·57 keV gamma rays. The coincidence system consists of a prolate spheroidal field β-ray spectrometer[11] (called the large

* This work was done at Bedford College, London University.

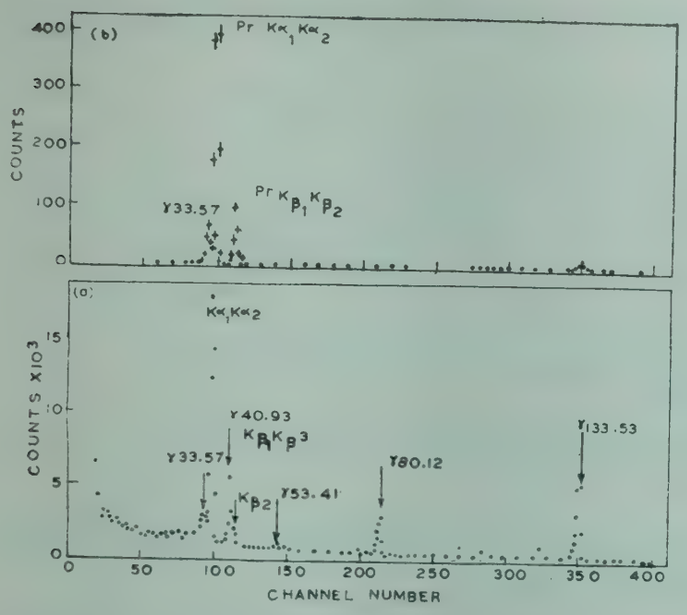

Figs. 1(a) & (b)—The singles gamma ray spectra resulting from the decay of $^{144}Ce \rightarrow ^{144}Pr$ measured with Ge(Li) X-ray detector. $K\alpha_2$-35·55 keV, $K\alpha_1$-36·02 keV, $K\beta_3$-40·65 keV $K\beta_2$-41·75 keV, $K\beta_1$-41·77 keV, (Gamma ray energies are given in keV and spectrum taken for 4 min.)

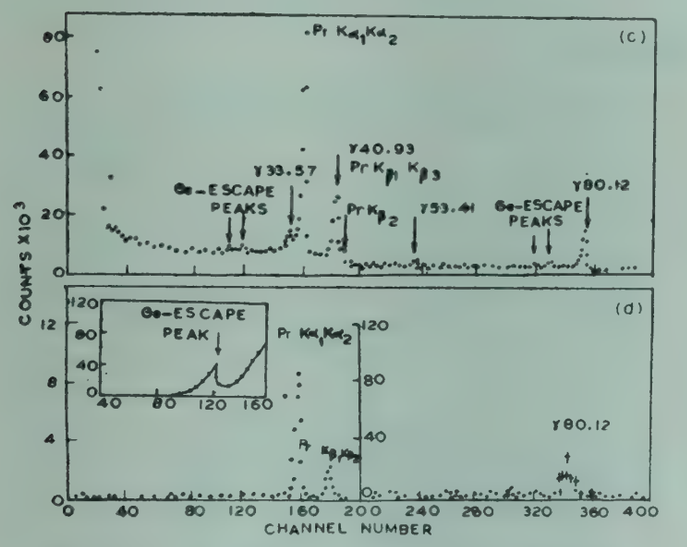

Fig. 1(c)—Coincidences with L40·93. The larger peak represents two peaks of $K\alpha_1\ \alpha_2$ X-rays
Fig. 1(d)—Coincidences with K 133·53 (coincidences taken for 1 hr)

spectrometer) and the magnetic lens beta spectrometer (called the small spectrometer). The resolving time of the coincidence system was estimated to be $2\tau = 14$ nsec, and the chance coincidence rate was of the order of 10^{-3} counts/sec (Ref. 12). Figs. 2 and 3 show the singles beta spectrum of ^{144}Ce measured with the large and the small spectrometers respectively. The momentum resolution of the large spectrometer was estimated to be 1·3% for 38·12 keV line, whereas, with the small spectrometer, for the 91 keV line it was 2·3%. In order to measure the coincidences, the small spectrometer was gated on the conversion line and the current in the large spectrometer was scanned. Figs. 4(a) and 4(b) show the coincidences when the gate was set on the peak of the 91·53 keV line (K 133·53) and on the β-continuum respectively. The difference in the relative height of the 26·75 keV line in Figs. 4(a) and 4(b) is estimated to be 17 counts whereas, the standard deviation in Fig. 4(a) was found to be 10 counts. On comparing the coincidence spectrum [Fig. 4(a)] to the singles spectrum (Fig. 3), not much enhancement in the relative height of the line was observed. The unduly large background under the 26·73 keV bump in Fig. 4(a) is attributed to the coincidences of 91·53 keV line with the β-continuum. The rise in the coincidence spectrum above 0·85 A [Fig. 4(b)] could be due to the coincidences of unresolved Auger electrons.

3. Conclusion

Though our e-γ coincidence measurements do not indicate the presence of a weak satellite of

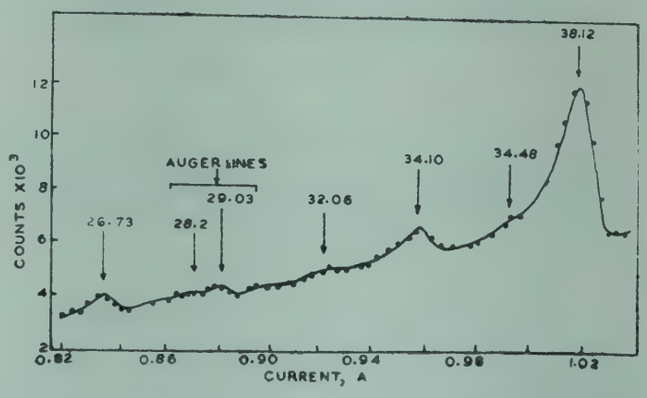

Fig. 2—The singles β-ray spectrum of ^{144}Ce below 38·12 keV measured with the large spectrometer. (The line energies are given in keV and spectrum taken for 4 min.)

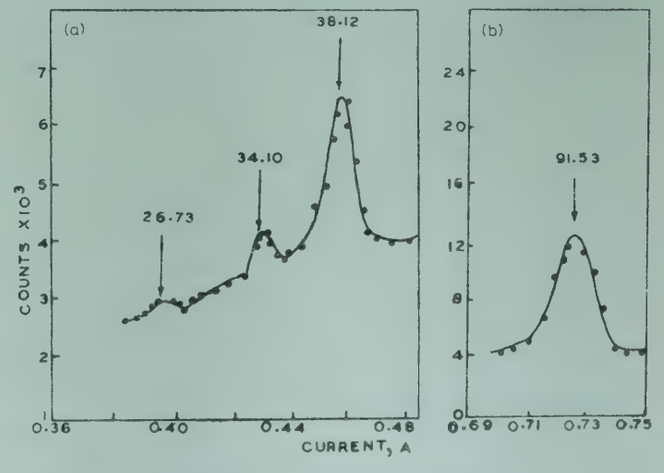

Fig. 3(a)—The singles β-ray spectrum of ^{144}Ce below 38·12 keV measured with the small spectrometer. (b) Conversion line of 91·53 keV (K 133·53). (The line energies are given in keV and spectrum taken for 4 min.)

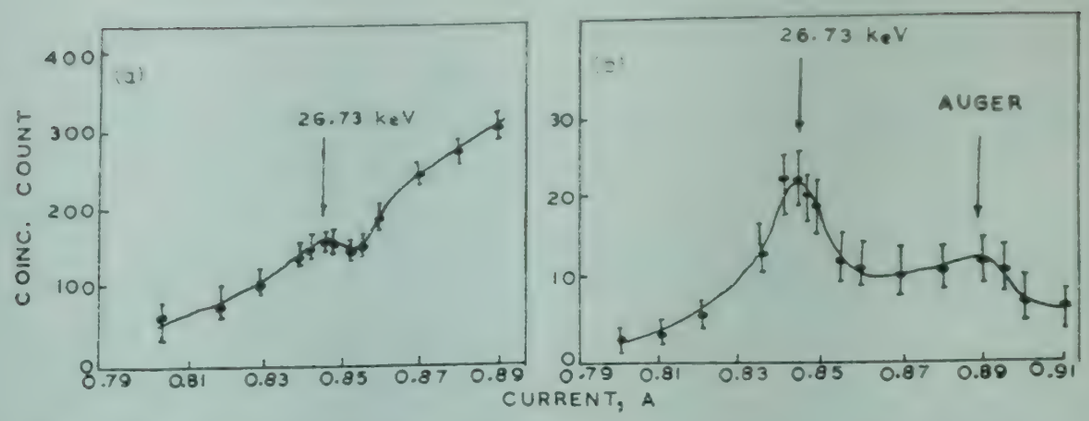

Fig. 4—The K 133·53-L 33·57 coincidences with the gate placed on (a) the peak of K 133·53 line (b) the beta continuum (spectrum taken for 1 hr)

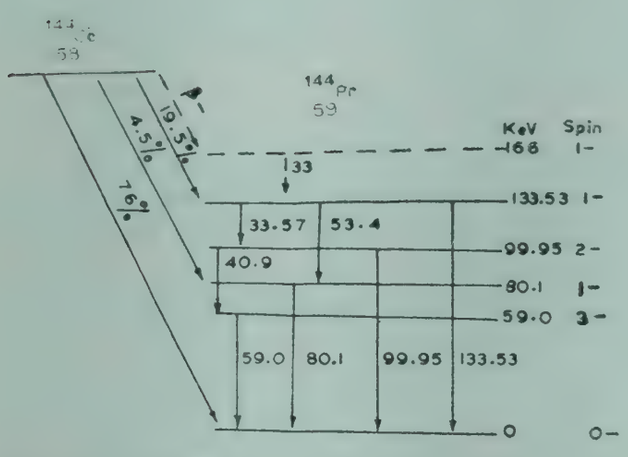

Fig. 5—The proposed decay scheme of ^{144}Ce (The dotted transition was suspected from the present coincidence measurements)

33·57 keV gamma, the e-e coincidence measurements give a small positive evidence of the conversion line of the transition (166 keV→133·53 keV). However, it could not be conclusive as the relative height of the line amounts to 1·5 times the standard deviation. From this particular measurement, though it seems difficult to set the lower limit for the 166 keV→133·53 keV transition, a decay scheme of ^{144}Ce could be proposed as shown in Fig. 5. The spin and parity (1−) to the 166 keV level could be assigned as proposed by Iwashita *et al.*[7]

Acknowledgement

The author is grateful to Prof. H O W Richardson of Bedford College, London University for his valuable discussions.

References

1. Freeman N J, *Proc. phys. Soc.*, **74** (1959), 449.
2. Geiger J S, Graham R L & Ewan G T, *Nucl. Phys.*, **16** (1960), 1.
3. Geiger J S, Graham R L & Ewan G T, *Nucl. Phys.*, **28** (1961), 387.
4. Forafontov N V, Shinel V S & Vasiler T S, *Nucl. Phys.*, 35 (1962), 260.
5. Iwashita T, Inamura T, Ikemota Y & Kageyama T, *J. phys. Soc. Japan*, **18** (1963), 1358.
6. Mangal P C & Trehan P N, *J. phys. Soc. Japan*, **27** (1969), 1.
7. *Nuclear Data Sheets*, 16 (1975), 231.
8. Mishra R K, *IEEE Trans.: Nucl. Sci.*, **23** (1976), 1478.
9. Mishra R K, *Curr. Sci.*, **48** (1979), 379.
10. Mishra R K, *Curr. Sci.*, **47** (1978), 536.
11. Evans P R, Freeman N S, McGinty G K, Armitage B H & Richardson H O W, *Proc. phys.Soc.*, 72 (1958), 949.
12. Mishra R K, *Curr. Sci.*, **48** (1979), 195.

Indian Journal of Pure & Applied Physics
Vol. 18, March 1980, pp. 183-190

Mechanism Responsible for the Observed Dielectric Relaxations in Polyvinylidene Fluoride

P C Mehendru, S Chand & K Jain
National Physical Laboratory, New Delhi 110 012

Received 31 *July* 1979; *revised received* 21 *September* 1979

Dielectric relaxations of polyvinylidene fluoride (PVF_2) films grown from solution have been studied as a function of poling temperature (318-373 K), time ($3{\cdot}6 \times 10^3$-$2{\cdot}16 \times 10^4$ sec), thickness (30-200 μm), nature of the vacuum deposited electrode metals (copper, silver, aluminium and indium) and the heating rates of depolarization (0·047-0·2 K/sec). The depolarization current spectrum of poled Ag:PVF_2:Ag shows two relaxation processes at 319 and 385 K, respectively. The peak at 319 K is attributed to the migration of the charge carriers with subsequent trapping into the shallow traps; the peak at 385 K is associated with the detrapping of the charge carriers from the deeper traps. The shift in the position of 385 K peak with the increase in either poling time or temperature and the linear increase in the activation energy with poling temperature suggest that this peak is due to the distribution of relaxation times and activation energies. The decrease in the magnitude of 385 K peak and the increase in the magnitude of 319 K peak with the increase in the work function of metals used as electrodes during poling, show that the nature of the electrode metals plays an important role in the charging of the PVF_2.

1. Introduction

Generally, electrets[1-3] were made of widely different materials such as resins, waxes, ceramics or mixtures of resins and waxes, but recently[4] the interest in the electrets made from such materials has relaxed because of the success in polymer electrets. The electrification of the polymers takes place due to one or more than one of the following mechanisms operative simultaneously, when it is subjected to dynamical, mechanical or thermal treatment with or without the static electric fields:

1. Space charge injected into the dielectric by surface breakdown between the dielectric and the electrode,
2. Space charge injected from the electrodes,
3. Space charge caused by migration of charge carriers over macroscopic distances,
4. Electronic or ionic dipoles caused by migration of charges over microscopic distances, and
5. Orientation of permanent dipoles.

Though the polymer electrets are the most extensively studied materials and numerous experimental data are available,[2-4] the mechanism associated with the internal persistent polarization observed in such polymer electrets is still not clear. Many workers associate this type of polarization with the thermal randomization of the aligned dipoles and a few of them attribute it to the migration of charge carriers over microscopic distances. It has been shown recently[5,6] that the magnitude of the total charge obtained from the electrets is a few orders of magnitude higher than that expected on the basis of the concentration of the dipoles involved during their electrification. Non-polar polymers are also known to exhibit sufficient charge on electrification. It has also been established[4,7] that the decay time of the charge in the former case is a few orders of magnitude higher than that in the latter, which shows that the charges responsible for the electret formation in polymers may not be due to the dipoles alone but there may be some other factors contributing to their dominant persistent polarization and long life/slower decay time.

The aim of the present investigation in polyvinylidene fluoride (PVF_2) is essentially to understand whether the persistent polarization in such polymers is due to the alignment of dipoles or migration of the charge carriers or a combination of both. The time constant involved in the decay of this charge at room temperature is of the order of several hours or even days. Thermally stimulated discharge current (TSDC) technique[2,4] is being used for investigating the parameters of the migration of charge carriers or of aligned dipoles in PVF_2 which has its glass transition temperature[8] well below the room temperature (RT) and hence the contribution of the aligned dipoles, if any, to the total polarization produced may not be significant. Although PVF_2 has

been studied extensively by dynamical, mechanical, dielectric or by TSDC techniques[9,10] below RT, only a few studies above RT have appeared in the literature.[11] As such, we have studied the dielectric behaviour with special reference to the relaxation mechanism in PVF_2 films as a function of poling temperature T_P (318-373 K), time t_p ($3{\cdot}6 \times 10^3$-$2{\cdot}16 \times 10^4$ sec), thickness (30-200 μm), nature of the vacuum-deposited electrode metals (copper, silver, aluminium and indium) and the heating rate H (0·047-0·2 K/sec), during the depolarization of the specimen by the TSDC technique. The results of these studies are presented in this paper.

2. Experimental Details

PVF_2 having a glass transition temperature ~220 K and melting point 430-463 K, was obtained from Polysciences Inc. (USA). The polymer for the preparation of the films has been used as such without any further purification/recrystallization.

2.1 Preparation of the Specimen

PVF_2 films were prepared by the solution evaporation technique.[12] A solution of PVF_2 was made in dimethylformamide (BDH make) and poured in a petri dish with an optical flat bottom. It was kept in a dust-free chamber at 380 K for $4{\cdot}32 \times 10^4$ sec to form a thin transparent PVF_2 film of uniform thickness which was measured with the help of a micrometer as well as by gravimetric method assuming the density of PVF_2 as 1·78 g/cm^3 and it was of the order of 35 μm. However, films of different thicknesses were also prepared by varying the concentration of the solute in the solvent. Vacuum-evaporated metal electrodes of area 1 cm^2 were used in the sandwich electrode structure. Depending on the experiments, copper, silver, aluminium or indium were used as metallic electrodes. Electrical contacts to the metal electrodes were made with an air drying-type of silver paint. In some experiments, a guard-ring surrounding the top electrode of the sandwich electrode structure was also used, but within experimental limits no effect was observed on the depolarization current. All the observations reported here are with silver electrodes unless stated otherwise.

2.2 TSDC Measurements

The specimens were poled while maintaining them at a certain temperature (T_P) with a dc voltage applied from a regulated power supply (ECIL India, model HV 4800 B) for a certain length of time (t_p). The specimens were then cooled to RT (~300 K) while keeping the poling voltage unchanged for an arbitrarily fixed time of $5{\cdot}4 \times 10^3$ sec.

Immediately after poling, the specimens were kept in a shielded assembly described elsewhere[13] in which they could be heated at a predetermined uniform rate from RT to about 600 K. Before starting the measurements, the electrodes were short-circuited for 300 sec to eliminate the accumulated electric charges due to the applied field during the poling process. The depolarization induced by increasing the temperature of short-circuited specimen at constant rate of 0·1 K/sec from RT to above the temperature of poling, was measured with the help of an electrometer (Keithley, model 610 C) and was recorded as a function of temperature by a copper constantan thermocouple mounted on the specimen, using an X-Y recorder coupled with the electrometer in the usual way.[13] In the case of overlapping peaks a partial heating technique[5] was also employed.

3. Results

3.1 Temperature Dependence

Curves A, B, C and D in Fig. 1 show the depolarization current characteristics of PVF_2 films poled for $t_p = 5{\cdot}40 \times 10^3$ sec with $E_P = 1{\cdot}0 \times 10^5$ V/cm and correspond to T_P = 318, 333, 353 and 373 K, respectively. In each case, two well-resolved peaks, one centred around 319 K (designated as peak I) and the other in the temperature range 380-420 K (designated as peak II) are observed. It is observed from these curves that with the increase in the poling temperature the position of peak I remains unaltered, whereas that of peak II shifts towards higher temperatures. Again, the magnitude of peak I decreases whereas that of peak II increases with the increase in the poling temperature. It is also observed that for lower values of T_P, the decrease in the magnitude of peak I is smaller as compared to that for higher T_P.

The value of activation energy (U) calculated[14] for the isolated processes under peak II for each of the curves of Fig. 1 is shown as a function of T_P in the inset of Fig. 1. It is observed that the value of U corresponding to peak II increases linearly with the increase in T_P. However, the activation energy (0·61 ± ·02 eV) associated with peak I remains unaltered with the increase in T_P.

3.2 Time Dependence

Time dependence depolarization current spectra of PVF_2 films poled under identical conditions at

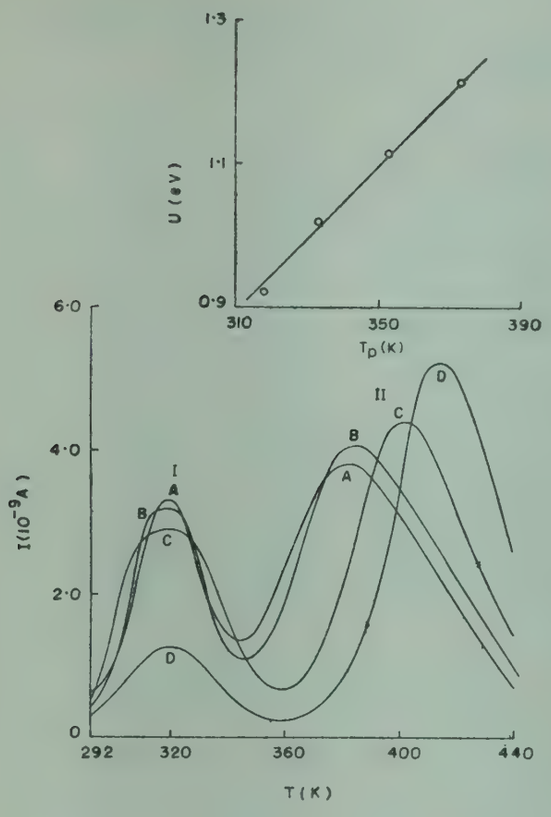

Fig. 1—TSDC curves of PVF_2 films of thickness 35 μm, poled for $5{\cdot}40 \times 10^3$ sec with $E_P = 1{\cdot}0 \times 10^5$ V/cm at different poling temperatures [Curves A, B, C and D correspond to T_P = 318, 333, 353, 373 K, respectively. The inset shows the plot between the activation energy (U) of the isolated process corresponding to peak II and T_P.]

333 K with $E_P = 1{\cdot}0 \times 10^5$ V/cm are shown in Fig. 2. Curves A, B, C and D correspond to t_p as $3{\cdot}60 \times 10^3$, $5{\cdot}40 \times 10^3$, $1{\cdot}26 \times 10^4$ and $2{\cdot}16 \times 10^4$ sec, respectively. As seen from Fig. 2, each curve exhibits the same two peaks, namely, peaks I and II. With the increase in t_p from $3{\cdot}60 \times 10^3$ to $2{\cdot}16 \times 10^4$ sec, the position of peak II is found to shift towards higher temperature (from 380-400 K) whereas that of peak I remains unchanged. It is also observed that the magnitude of peak current for peak II and hence the charge associated with it increase with the increase in t_p whereas those for peak I decrease.

The activation energy calculated[14] for the isolated processes under peak II (Fig. 2) is found to increase from 0·99 to 1·22 eV with the increase in t_p from $3{\cdot}60 \times 10^3$ to $2{\cdot}16 \times 10^4$ sec whereas the activation energy ($0{\cdot}61 \pm 0{\cdot}02$ eV) corresponding to peak I remains the same.

3.3 Thickness Dependence

The TSD currents of PVF_2 films of different thicknesses in the range 30-200 μm, poled under identical conditions ($E_p = 1{\cdot}0 \times 10^5$ V/cm, $t_p = 5{\cdot}40 \times 10^3$ sec and $T_P = 333$ K) were also studied. When the total charge Q involved in the discharge processes is plotted against the thickness of the PVF_2 films a straight line is obtained which leads to the conclusion that in PVF_2 films uniform volume polarization is operative.

3.4 Dependence on Nature of Metallic Electrodes

The TSD currents of PVF_2 films poled under identical conditions ($E_P = 1{\cdot}0 \times 10^5$ V/cm, t_p $5{\cdot}40 \times 10^3$ sec and $T_P = 333$ K) but with different metal electrodes, namely, copper, silver, aluminium and indium, and their respective TSDC spectra are shown by curves A, B, C and D in Fig. 3. It is seen from these curves that with the increase in the work function of the metal electrodes there is a continuous shift in the position of peak I towards lower temperatures and that of peak II towards higher temperatures. Further, the magnitude of peak I increases whereas that of peak II decreases with the increase in the work function of the metal used as electrodes during poling. However, the increase in the magnitude of peak I is smaller as compared to the decrease in the magnitude of peak II with the increase in the work function of the metal electrodes.

3.5 Evaluation of the Relaxation Parameters

In order to evaluate the activation energies of the discharge processes associated with peaks I and II, the partial heating technique[5] has been applied to isolate the individual peaks of the composite curves of Figs. 1, 2 and 3. Typical plots of log I vs $1/T$ from the initial rising parts of the TSDC peaks

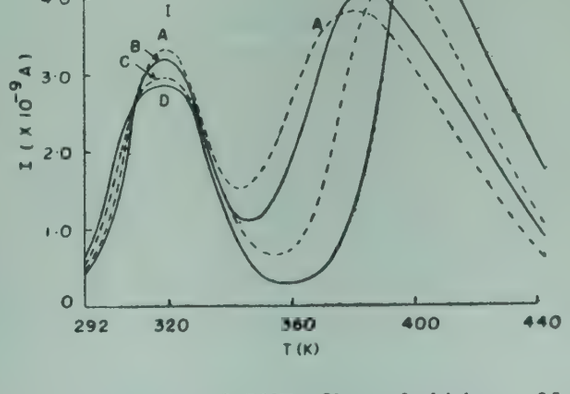

Fig. 2—TSDC curves of PVF_2 films of thickness 35 μm, poled at 333 K with $E_P = 1{\cdot}0 \times 10^5$ V/cm for different poling times. [Curves A, B, C and D correspond to t_p values of $3{\cdot}60 \times 10^3$, $5{\cdot}40 \times 10^3$, $1{\cdot}26 \times 10^4$, $2{\cdot}16 \times 10^4$ sec, respectively.]

Table 1—Depolarization Kinetic Data as Calculated by the Initial Rise Method for 319 K Peak of Poled PVF_2 Films of Thickness 35 μm

Curve	E_P V/cm	T_P K	t_p sec	T_M K	I_M 10^{-9} A	U eV	τ_0 10^8 sec	τ_M 10^2 sec	τ_{300} 10^2 sec
A	$1{\cdot}0\times10^5$	318·0	$5{\cdot}40\times10^3$	319·0	3·30	0·59	7·07	1·48	5·78
B	$1{\cdot}0\times10^5$	333·0	$5{\cdot}40\times10^3$	319·0	3·20	0·62	2·17	1·41	5·90
C	$1{\cdot}0\times10^5$	353·0	$5{\cdot}40\times10^3$	319·0	2·90	0·62	2·37	1·42	5·89
D	$1{\cdot}0\times10^5$	373·0	$5{\cdot}40\times10^3$	319·0	1·25	0·62	2·17	1·41	5·90
A	$1{\cdot}0\times10^5$	333·0	$3{\cdot}60\times10^3$	319·0	3·30	0·62	2·42	1·42	5·89
B	$1{\cdot}0\times10^5$	333·0	$5{\cdot}40\times10^3$	319·0	3·20	0·62	2·17	1·41	5·90
C	$1{\cdot}0\times10^5$	333·0	$1{\cdot}26\times10^4$	319·0	2·95	0·62	2·43	1·42	5·89
D	$1{\cdot}0\times10^5$	333·0	$2{\cdot}16\times10^4$	319·0	2·85	0·61	3·40	1·44	5·85

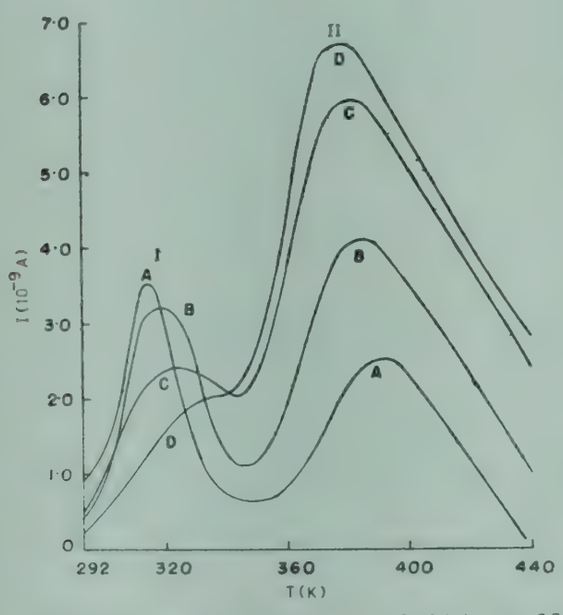

Fig. 3—TSDC curves of PVF_2 films of thickness 35 μm, poled under identical conditions ($E_P = 1{\cdot}0 \times 10^5$ V/cm, $T_P = 333$ K, $t_p = 5{\cdot}40 \times 10^3$ sec), but with different electrode metals deposited in vacuum [Curves A, B, C and D correspond to electrodes of copper, silver, aluminium and indium, respectively.]

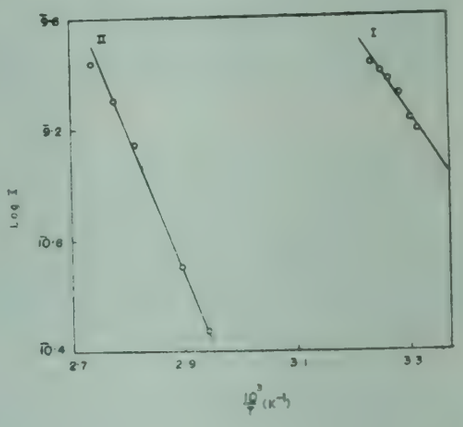

Fig. 4—Plots of log I vs $1/T$ obtained from the initial rising portion of the TSDC curve B of Fig. 1. [Straight lines I and II correspond to peaks I and II, respectively.]

(for curve B, Fig. 1) obtained from the PVF_2 specimen poled at 333 K are shown in Fig. 4. The activation energies of the isolated peaks, calculated from the slopes of these curves are 0·62 ± 0·02 and 1·04 ± 0·02 eV for the peaks I and II, having relaxation times of $5{\cdot}90 \times 10^2$ and $8{\cdot}99 \times 10^5$ sec at 300 K, respectively. Similar calculations for peaks I and II have also been made for other curves of Figs. 1 and 2 and their results are also given in Tables 1 and 2, respectively.

Values of U were also determined[15] from the straight lines obtained when the log of the remaining charge (Q_T) divided by the current $I(T)$ at a particular temperature and were plotted against $1/T$ for each of the two peaks (curve B, Fig. 1) obtained for the PVF_2 specimen, as shown in Fig. 5. U evaluated from the plots of Fig. 5 for peaks I and II is 0·57 ± 0·02 and 0·99 ± 0·02 eV, respectively. The method of Hoogenstraaten[16] was also applied to evaluate the activation energies of the various TSDC peaks which essentially consists in poling the specimen under identical conditions and then discharging it, using various heating rates H and finally by plotting the log of the ratio of the square of the peak temperature (T_M^2) to the heating rate H as a function of $1/T_M$. The slope of this plot gives the average value of U. A typical plot for peaks I and II for a specimen poled under the stated experimental conditions is shown in Fig. 6 The average values of U as calculated from the slopes of the two straight lines are 0·58 ± 0·02 and 0·99 ± 0·02 eV for peaks I

Table 2—Depolarization Kinetic Data as Calculated by the Initial Rise Method for 385 K Peak of Poled PVF_2 Films of Thickness 35 μm

Curve	E_P V/cm	T_P K	t_p sec	T_M K	I_M 10^{-9} A	U eV	τ_0 10^{12} sec	τ_M 10^2 sec	τ_{300} 10^6 sec
A	$1{\cdot}0\times10^5$	318·0	$5{\cdot}40\times10^3$	382·5	3·7	0·94	50·35	1·33	0·35
B	$1{\cdot}0\times10^5$	333·0	$5{\cdot}40\times10^3$	385·0	4·05	1·04	2·78	1·22	0·89
C	$1{\cdot}0\times10^5$	353·0	$5{\cdot}40\times10^3$	401·0	4·4	1·13	0·73	1·22	7·51
D	$1{\cdot}0\times10^5$	373·0	$5{\cdot}40\times10^3$	415·0	5·2	1·24	0·07	1·20	44·43
A	$1{\cdot}0\times10^5$	333·0	$3{\cdot}60\times10^3$	381·0	3·8	0·99	10·09	1·26	0·43
B	$1{\cdot}0\times10^5$	333·0	$5{\cdot}40\times10^3$	385·0	4·05	1·04	2·78	1·22	0·89
C	$1{\cdot}0\times10^5$	333·0	$1{\cdot}26\times10^4$	394·0	4·25	1·13	0·39	1·18	3·99
D	$1{\cdot}0\times10^5$	333·0	$2{\cdot}16\times10^4$	401·0	4·65	1·22	0·05	1·14	16·29

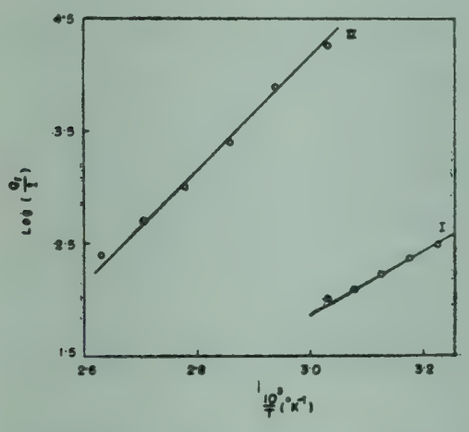

Fig. 5—Fit of experimental data for both the peaks of curve B of Fig. 1 with Bucci's equation of PVF_2 films of thickness 35 μm, poled at 333 K for $5{\cdot}40\times10^3$ sec with $E_P = 1{\cdot}0\times10^5$ V/cm. [Straight lines I and II correspond to peaks I and II, respectively.]

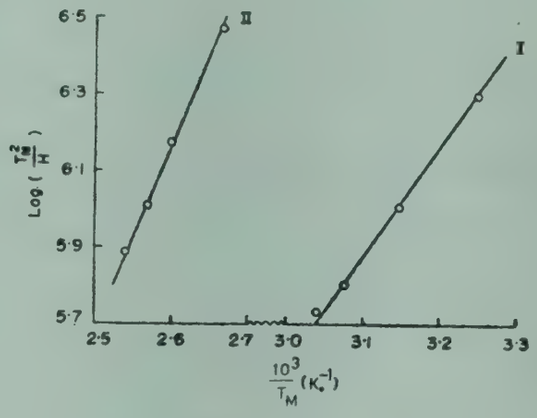

Fig. 6—A plot of $\log\left(\frac{T_M^2}{H}\right)$ versus $\left(\frac{1}{T_M}\right)$ obtained from the TSDC curves of the PVF_2 films of thickness 35 μm, poled at 333 K for $5{\cdot}40\times10^3$ sec with $E_P = 1{\cdot}0\times10^5$ V/cm, for heating rates varying from 0·047 to 0·2 K/sec [Straight lines I and II correspond to peaks I and II, respectively.]

and II, respectively, which are very close to the values of U calculated by the method of Bucci *et al.*[15] and by the initial rise method.[14]

4. Discussion

Three dielectric relaxation processes, namely α_c, α_a and β, have been detected in bulk PVF_2 by many workers[17–20] from the frequency dependence of dielectric loss (ϵ'') measured in the temperature range 77-425 K and over the frequency range 0·1-0·3 MHz. These processes have also been observed by the dynamical mechanical measurements.[21] The α_c relaxation peak located at 370 K (1 kHz) is related to the molecular motion in the crystalline region and the α_a relaxation located at 246 K (1 kHz) attributed to the micro-Brownian motion of the amorphous main chains.[21] The relaxations accompanied with small values of U, located at 226 K (1 kHz) are very small and hence are attributed to the local oscillations of the frozen main chains. Later, Pfister *et al.*[11] have observed the peak at 220 K in the TSDC spectrum in addition to another two peaks at temperatures higher than 300 K. They have attributed the low temperature peak to the molecular motion involving the thermal randomization of the aligned dipoles connected to PVF_2 chains in the glass transition temperature region.

Peak I observed in our experiments, being the lowest temperature peak, may correspond to the already observed relaxation peak[11] which is also supported by the value of U associated with this discharge process. The energy required for the molecular motion or for the reorientation of the dipoles in many polymers[2,4–6] is also of the same order, and no current has been observed on reheating the unpoled specimen. These facts indicate

that this peak may be attributed to the molecular motion involving the depolarization of the aligned dipoles of the main polymer chain. Such a value of U may also be observed if the current into the external circuit is due to the release of the charge either at the glass transition temperature or through the phase change or by the migration of charge carriers at microscopic level with subsequent trapping. But the first two possibilities are being ruled out since the PVF_2 has transitions[8] at 220 K and 290 K. Moreover, no transition has been detected in the DTC measurements in the temperature range under study. The linear increase in the charge[22] associated with peak I with the increase in E_P indicates that this peak may be either because of thermal randomization of the aligned dipoles or due to migration of charge carriers over microscopic distance with subsequent trapping rather than due to the detrapping of the space charge created either by the migration of the charge carriers over a microscopic distance, injection or spraying of the charge carriers from the electrodes. However, it is difficult to believe that charge associated with peak I is due to the dipole orientation because of the following reasons. (i) The orientation of the permanent dipoles cannot be retained in the amorphous region above room temperature (the glass transition temperature being 220 K) and the orientation of the permanent dipoles of PVF_2 chain is difficult because these chains may be locked in the highly crystalline regions of the polymers which would prevent any segmental motion even around T_g. (ii) If one assumes that the charge released to the external circuit is due to the deorientation of the dipoles, then one expects a few hundred dipoles per monomer (considering the density of PVF_2 as 1·78 g/cm^3, dipole moment 2·1 D and the degree of polymerization about 10^3) which is not possible in this case, since in PVF_2 the dipolar motion could arise from the orientation of the permanent dipoles associated with the C—F bonds only. (iii) When a depolarized specimen is reheated (results not reported here), depolarization current in the external circuit in the temperature range coincident with peak I during the first heating is observed which leads to the conclusion that the depolarization current is due to the movement of the real charges.

Therefore, the mechanism associated with peak I may be the migration of the charge carriers over microscopic distances with subsequent trapping in the available traps as already proposed.[23] These charge carriers (possibly electrons/holes) when released from the valence band are trapped in their respective available electron/hole traps and when the specimen is heated to observe thermal currents, these charges are released from these traps, migrate under local fields and are recaptured.

If one assumes a recapture time small compared with the lifetime in traps, the rate of decay of polarization depends on the rate of release of charge carriers from traps and the thermal currents should have the same temperature dependence as in the case of the molecular motion.[5] In view of the above facts, it may be concluded that peak I is associated with the migration of the charge carriers over a microscopic distance with subsequent trapping. The decrease in the magnitude of the peak current and hence that of the charge with the increase in the poling time and temperature can be explained on the basis of the net trapping probability of the charge carriers.[24,25] At higher values of T_P, the relative detrapping probability from shallow traps becomes high which would favour the redistribution of charges and their trapping into the deeper traps. Moreover, the magnitude of peak I would also depend, to a great extent, upon the relative number of the shallow and the deep traps which are very sensitive to the physical properties of the polymers. Therefore, the number and the type of the traps may change depending on the poling conditions.

The activation energy of the discharge process associated with peak II is of the order of 0·99 $\pm$ 0·02 eV and its charge remains practically constant with the increase of the poling field[22] and dependence of this charge on the poling time and temperature indicates that the mechanism involved in the discharge process corresponding to peak II is the detrapping of the charge carriers as already suggested by Gerson and Rohrbaugh[26] and later by Caserta and Serra.[27] Although the order of energy values ($\sim$ 0·7 eV) is generally associated with the ionic traps,[28] the high value of U as found here (i.e. 0·99 $\pm$ 0·02 eV) may not necessarily be associated with the ionic traps in a large band gap material.[29] Since the glass transition temperature of the material under study is far below RT, at temperatures $\geq$ RT, one would expect the availability of free carriers (possibly ions) due to the degradation of the polymer chain, dissociation of the molecules, due to the presence of trapped impurities or ionic species released during chemical degradation which would give rise to the H^+ and F^- ions. This inference is further supported by the fact that solvent cast films as used in these experiments are having free ionic carriers because of the presence of trace impurities, particularly alkalies which are likely to degrade the material during solvation.

Initially these carriers must be distributed uniformly throughout the material: therefore, no

depolarization current was observed on heating the unpolarized specimens. With the increase in T_P (Fig. 1) more and more carriers would be available during the poling and would give rise to an increase in the magnitude of peak II. Since the carrier migration would be a time-dependent phenomenon, an increase in the magnitude of peak II would be expected with the increase in the poling time (Fig. 2). When the specimen is heated at an elevated temperature in the presence of E_P, free charges are produced from the valence band. On cooling the specimen, these charge carriers would be trapped into the deeper traps which would give a shift in the position of peak II with the increase in T_P and t_p. A continuous shift in the position of peak II is observed with the increase in T_P and t_p and the activation energies associated with the isolated processes under peak II are also found to increase with increase in T_P and t_p (Figs. 1 and 2) suggesting thereby that peak II may not be due to a discrete level of activation energy having a single relaxation time; rather, it may be a complex peak having a distribution[30,31] of relaxation times, since it is established[15] that for a single relaxation process of fixed U and H the position of peak is independent of t_p and T_P. A linear increase of activation energies associated with the isolated processes under peak II is in support of our assumption of the distribution of relaxation times.

When the specimens are poled under identical conditions with different electrode metals, namely copper, silver, aluminium and indium having different work functions but each one having a work function less then that of the polymer used,[32] the metal having higher work function would have smaller barrier height and hence would inject/transport larger number of charge carriers than the metal having comparatively lower work function. Thus there would be a maximum number of injected/transported charge carriers from copper to the polymer and a minimum from indium to the polymer. Since the injection of the charge carriers from the electrodes to the polymer would result in the reduction of the contribution of the heterocharge[33] (due to the indigenous charge carriers), it would give rise to a decrease in the magnitude of peak II as we go from indium to copper. However, the increase in the magnitude of peak I (with the increase in the work function of the electrode metal) is perhaps due to the space charge, created by the applied field and acts in the same direction as that of E_P and hence would increase the effect of E_P which finally results in the enhancement of the charge associated with peak I as shown in Fig. 3. Further experiments are in progress to understand the nature of the conduction mechanism involved in the discharging of PVF_2.

5. Summary of Results and Conclusions

(i) Two relaxation processes at 319 K (peak I) and 385 K (peak II) having activation energies $0{\cdot}62 \pm 0{\cdot}02$ and $1{\cdot}04 \pm 0{\cdot}02$ eV and the relaxation times at 300 K, $5{\cdot}9 \times 10^2$ and $8{\cdot}99 \times 10^5$ sec, respectively, are obtained for PVF_2 films of thickness 35 μm poled at 333 K for $t_p = 5{\cdot}40 \times 10^3$ sec with $E_P = 1{\cdot}0 \times 10^5$ V/cm.

(ii) Peak I is attributed to the migration of the charge carriers with subsequent trapping into the shallow traps and peak II is associated with the detrapping of the charge carriers from the deeper traps.

(iii) The decrease in the magnitude of peak I and increase in the magnitude of peak II with the increase in t_p and T_P suggest that the trapping probability and the type of the carriers play an important role in the charging of PVF_2.

(iv) The shift in the positions of peak II with the increase in t_p and T_P and the linear increase in the activation energy with T_P are attributed to the distribution of relaxation times.

(v) The activation energy, as determined from the initial rise method, agrees well with those obtained by the modified Bucci's plot and also with the heating rate method.

Acknowledgement

The authors are grateful to Dr A R Verma Director, National Physical Laboratory, New Delhi, for his deep interest in the problem. One of them (SC) is also thankful to CSIR, New Delhi, for financial assistance.

References

1. Gross B, *J. chem. Phys.*, 17 (1949), 866.
2. Pillai P K C, Jain K & Jain V K, *Phys. Status Solidi (a)*, 13 (1972), 341.
3. Gutmann F, *Rev. mod. Phys.*, **20** (1948), 457.
4. Van Turnhout J, *Thermally stimulated discharge of polymer electrets* (Elsevier, Amsterdam), 1975.
5. Perlman M M, *J. appl. Phys.*, **42** (1971), 2645.
6. Mehendru P C, Jain K & Mehendru P, *J. Phys.*, **D 8** (1975), 305; **D10** (1977), 729.
7. Lilly A C, Steward L L & Henderson R M, *J. appl. Phys.*, **41** (1970), 2001, 2007.
8. Sasabe H & Saito S, *J. Polym. Sci. A-2: Polym. Phys.*, 7 (1969), 1405.
9. Callens A, Balist De R & Eersels L, *Nuovo Cim.*, **33B** (1976), 434.

10. Yano S, *J. Polym. Sci. A*-2: *Polym. Phys.*, **8** (1970), 1057.
11. Pfister G & Abkowitz M A, *J. appl. Phys.*, **45** (1974), 1001; **46** (1975), 2559.
12. Pillai P K C, Jain K & Jain V K, *J. electrochem. Soc.*, **120** (1975), 435.
13. Jain K, Rastogi A C & Chopra K L, *Phys. Status Solidi* (*a*), **20** (1973), 167.
14. Garlick C F J & Gibson A F, *Proc. phys. Soc. Lond.*, **60** (1948), 574.
15. Bucci C, Fieschi R & Guidi G, *Phys. Rev.*, **148** (1966), 816.
16. Hoogenstraaten W, *Philips Res. Rep.*, **13** (1958), 515.
17. Brereton M G & Davies G R, *J. Polym. Sci. A*-2: *Polym. Phys.*, **15** (1977), 583.
18. Nakagawa K & Ishida Y, *J. Polym. Sci. A*-2: *Polym. Phys.*, **11** (1973), 1503.
19. Kakutani H, *J. Polym. Sci. A*-2: *Polym. Phys.*, **8** (1970), 1177.
20. Yano S, Tadano K & Aoki K, *J. Polym. Sci. A*-2: *Polym. Phys.*, **12** (1974), 1875.
21. Peterlin A & Elwell J, *J. mater. Sci.*, **2** (1967), 1.
22. Jain K, Chand S & Mehendru P C, *Physics Lett.*, **74A** (1979), 288.
23. Roggen Van A, Annual Report, *Proc. Conf. Elect. Insulation* (National Research Council, Ottawa, Canada), (1965), 1356.
24. Suzuoki Y, Yasuda K, Mizutani T & Ieda M, *Japan J. appl. Phys.*, **17** (1978), 1215.
25. Ikezaki K, Hottori M & Arimoto Y, *Japan J. appl. Phys.*, **16** (1977), 863.
26. Gerson R & Rohrbaugh J H, *J. chem. Phys.*, **23** (1955), 2381.
27. Caserta G & Serra A, *J. appl. Phys.*, **42** (1971), 3778.
28. Jonscher A K, *Thin Solid Films*, **1** (1967), 213.
29. Gupta N P, Jain K & Mehendru P C, *Thin Solid Films*, **61** (1979), 297.
30. Hino T, *Elect. Engng.* (*Japan*), **93** (1973), 31.
31. Gupta N P, Jain K & Mehendru P C, *J. chem. Phys.*, **68** (1978), 1785.
32. Davies D K, *Brit., J. appl. Phys.*, **2** (1969), 1533.
33. Mehendru P C, Jain K & Mehendru P, *J. Phys.*, **D 11** (1978), 1431.

Indian Journal of Pure & Applied Physics
Vol. 18, March 1980, pp. 191-194

Polarized Absorption Spectra of Fluoranthene in Pure & Mixed Crystals

N B Palit, S C Chakravorty & M K Choudhury
Solid State Physics Laboratory, Jadavpur University, Calcutta 700 032

Received 5 *December* 1978

Polarized absorption spectra of single crystals of fluoranthene and fluoranthene-doped in fluorene crystal matrix have been studied in the wavelength range 3080-3800 Å at 90 K. The crystal spectrum in this region is somewhat different from the solution spectrum of the molecule, and the spectral region has been found to consist of two different electronic absorption systems. The first and second absorption systems appear to arise from singlet-singlet transition of $A_1 \leftarrow A_1$ (long-axis polarized) and $B_2 \leftarrow A_1$ (short-axis polarized) species respectively. Such an assignment has been made considering the absorption intensity and polarization ratios of the two systems investigated in pure and mixed crystal.

1. Introduction

Fluoranthene is a non-alternant hydrocarbon compound of medium size. Spectral data of such non-alternant compounds are very few. To collect more information about such non-alternant compounds we have studied the polarized absorption spectrum of fluoranthene crystal.

In view of the pronounced dissimilarity that has been noticed between the solution spectrum[1] and the crystal spectrum in *bc* face of the crystal, such an investigation became more important.

We have concentrated our attention around two main aspects, viz. (i) whether the spectral region 3080-3800 Å investigated consists of only one singlet-singlet absorption system or more; (ii) to assign the said transition (or transitions) to the molecular symmetry species. The study of the polarized spectrum of fluoranthene as guest in fluorene host crystal matrix has helped us on both aspects.

2. Experimental Procedure

A sample of fluoranthene (Coch-light) was subjected to repeated recrystallization for purification. Single crystals were grown from melt between two fused silica plates; single crystals thus grown generally develop (100) face and exhibit good extinction property. Very thin crystals grown in this method were scanned under a polarizing microscope and the axes were identified.

Spectroscopic arrangement for obtaining polarized absorption spectra has been described elsewhere.[2] In our experiment, spectra were recorded spectrophotometrically by an IP-28 photomultiplier tube fitted to a Hilger medium dispersion quartz monochromator. A high pressure Zeiss XBO-101 xenon lamp was used as a source of continuous light. To attain the low temperature, crystals were inserted in a metal cryostat.

3. Result and Discussion

Fluoranthene is a monoclinic crystal[3] having space group P_{21}/n and containing eight molecules per unit cell. There are two independent sets of molecules in the asymmetric unit. The unit cell dimensions are $a = 19{\cdot}907$ Å, $b = 6{\cdot}221$ Å, $c = 18{\cdot}349$ Å and $\beta = 109{\cdot}86°$.

From the molecular position given in the crystallographic data, the orientation of the molecule in the crystal lattice was computed and the (*b*:*c*) oriented gas model polarization ratio was calculated for the two independent sets and are given in Table 1.

Table 1—Orientation of Fluoranthene Molecule in Crystal Lattice

Transition direction	Angle with axes				Polarization ratio *b*:*c*
	a	*b*	*c'*	*c*	
			1st Set		
L	38 41′	52 9′	82 14′	99 58′	12·53:1
M	97 5′	13 47′	78 10′	76 42′	17·82:1
N	52 13′	90 3′	14 13′	15 34′	—
			2nd Set		
L	45 43′	52 46′	69 2′	80 20′	12·94:1
M	91 20′	166 28′	76 34′	76 48′	18·12:1
N	44 20′	90 13′	25 15′	15 22′	—

Four distinct peaks are observed in the solution spectra[1] of this region—the first three being equally intense and the fourth one of slightly diminished intensity. Polarized absorption spectra of fluoranthene crystal as recorded by us (Fig. 1) shows several peaks. As regards their intensity and sharpness, they are quite different from their solution counterpart. Band peaks appearing at 27248, 27624 and 28571 cm^{-1} are of very low intensity in comparison to the other peaks appearing at 30303 and 31948 cm^{-1}. Thus two distinct sets of bands appear to be observed in the crystal spectra of this region unlike the solution spectra. If the spectrum of entire region investigated is assumed to belong to the same absorption system, the enormous lowering of intensity of the first few bands cannot be reconciled. Nor can it be explained on the basis of crystal induced mixing of state as this should not affect the intensity of bands of the same system so abruptly. It is to be noted here that the two asymmetric dispositions of the molecules in the unit cell cannot affect the peak intensity of this spectrum, as in both the asymmetric units the molecular axes make almost equal angles with *b* and *c*-axes of the crystal.

We now consider the other possibility that the two sets of bands observed in the crystal spectrum may belong to two different absorption systems. It may so happen that the free molecular extinction coefficients of bands of the two systems are nearly same but their transition directions are different.

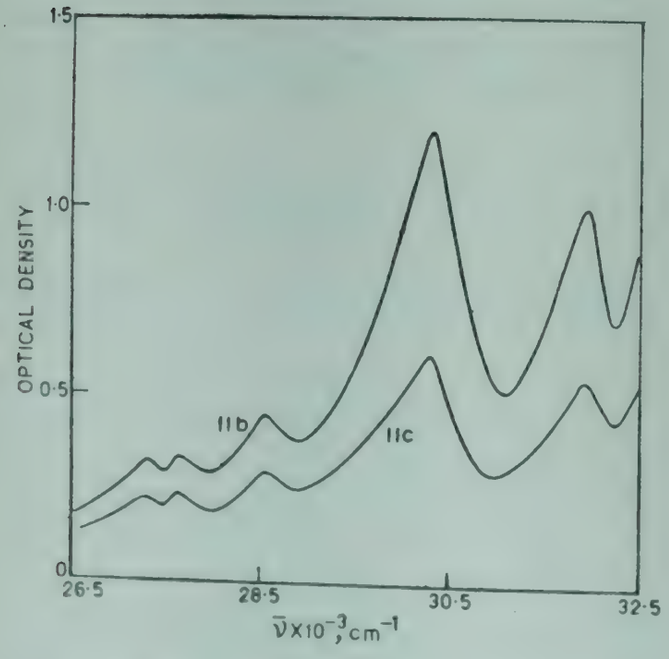

Fig. 1—Absorption spectra of fluoranthene in *bc*-face at 90 K polarized || *b* and || *c* axes [crystal thickness $(t)=0{\cdot}2\mu$]

Fluoranthene molecule belongs to C_{2v} symmetry and so two types of transitions can take place for π-electron, one is short axis polarized ($B_2 \leftarrow A_1$) transition and the other is long-axis polarized ($A_1 \leftarrow A_1$) transition. These two transition directions have different orientations with respect to the crystallographic axes *b* and *c*. As the long-axis of the molecule makes larger angles with *b* and *c* axes respectively, compared to those made by short-axis, absorption intensity due to this transition is expected to be lower than that due to the short-axis polarized transition. In the light of this consideration, the first set of absorption bands appearing in the longer wave-length side seems to be due to long-axis (*L*-axis) and the more intense next absorption system seems to be due to short-axis (*M*) polarized transition. If this assignment be true, the polarization ratio (*b*:*c*) should be higher for the second system than for the first one (Table 1). The observed polarization ratio is found to obey this sequence (Table 2), but the actual value in either case is lower than the oriented gas model value. On the basis of this assignment, we also try to correlate the observed extinction coefficient (obtained from Fig. 2) with the free molecular extinction coefficient computed from solution spectral data. It is found that observed *b* polarized extinction coefficient agrees quantitatively with the calculated value for both the systems (Table 3) but the observed *c*-polarized extinction coefficient for either system is greater than the calculated extinction coefficient. It thus appears that the first set of absorption bands are due to long-axis ($A_1 \leftarrow A_1$) and the second set of absorption bands are due to short-axis ($B_2 \leftarrow A_1$) polarized

Table 2—Polarization Ratios for the Long-axis and Short-axis Transitions

Band peak position $\bar{\nu}$ cm^{-1}	Frequency interval $\bar{\nu}-\bar{\nu}_0=\Delta\bar{\nu}$ cm^{-1}	Analysis	Polarization ratio *b*:*c*
First system; Assignment:	Long-axis ($A_1 \leftarrow A_1$) transition		
27248	0	0-0	1·43:1
27624	376	376	1·46:1
28571	1323	1323	1·49:1
Second system; Assignment:	Short-axis ($B_2 \leftarrow A_1$) transition		
30303	0	0-0	1·968:1
31948	1645	1645	1·82:1

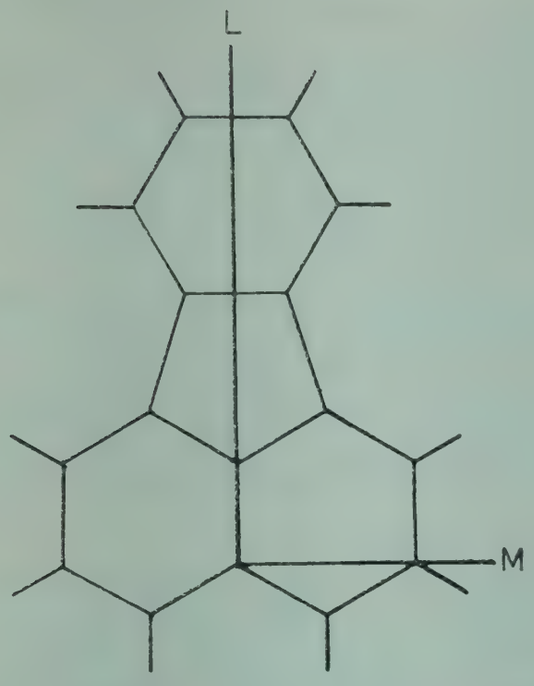

Fig. 2—Long (*L*) axis and Short (*M*) axis of fluoranthene molecule

Table 3—Calculated and Observed Extinction Coefficient for the Two Absorption Systems

Band peak position	Observed extinction Coefficient		Calculated extinction Coefficient			
			Long-axis transition		Short-axis transition	
$\bar{\nu}$ cm^{-1}	*b*-polarized	*c*-polarized	*b*-polarized	*c*-polarized	*b*-polarized	*c*-polarized
			First System			
27248	2625	1875	9476	726·7	23560	1310·5
28571	3675	2550	9049·5	694	22490	1252
			Second System			
30303	10040	5083	6864	522·8	17065	949·6
31948	8373	4167	4146·5	319·5	10285	572

transition. However, the quantitative agreement of the oriented gas model value of polarization ratios and extinction coefficient with the experimentally measured values are somewhat poor. This lack of agreement has prompted us to undertake a supporting work in the form of a mixed crystal experiment.

3.1 Mixed Crystal Spectra

Mixed crystals were prepared either by slow evaporation of the alcoholic solution of fluorene containing a small amount of fluoranthene or from a melt of fluorene containing a small amount of fluoranthene between two fused silica plates. Crystals grown by either way develop crystallographic *ab* face.

Mixed crystal spectra were recorded spectrophotometrically and are shown in Fig. 3. The first set of bands appearing between 27200 to 28900 cm^{-1} in pure crystal spectra appears only as a slight hump at 27385 cm^{-1} in the mixed crystal spectra. But the sharp and intense second set of band peaks appearing in the pure crystal spectra, appears equally sharp and intense in this mixed crystal spectra. The long-axis (*L*-axis) of the fluorene[4] molecule is along the *c*-axis direction of the crystal, i.e. normal to *ab* face and the short-axis (*M*-axis) lies in the *ab*-face. If we assume, that fluoranthene molecules go into substitution solid solution in fluorene matrix, the *L*-axis polarized transition of fluoranthene in fluorene should be completely absent and *M*-axis polarized transition should appear very strongly when viewed normally through *ab*-face.

Now in the solution spectra of fluoranthene, the set of bands lying between 27000 to 33300 cm^{-1} are of comparable intensity. But in the mixed crystal

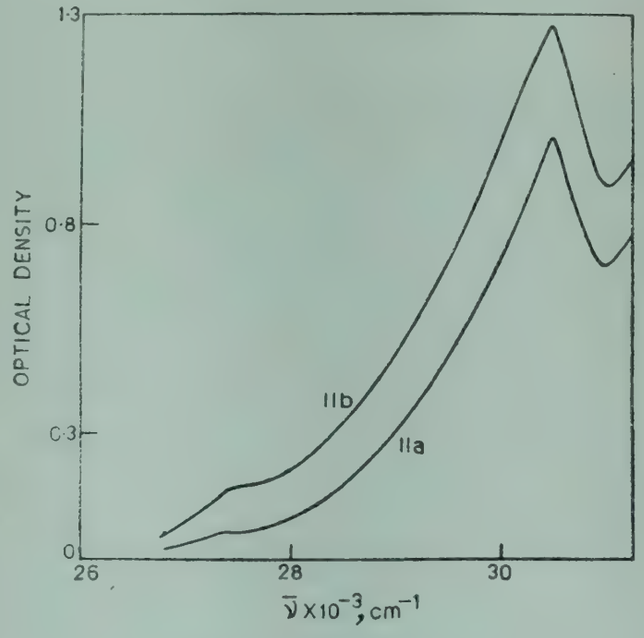

Fig. 3—Absorption spectra of fluoranthene in fluorene at 90 K polarized ‖ *b* and ‖ *a* axes.

Table 4—Molecular Orientation of Fluorene in Crystal Lattice

Transition direction	Angle with axes			Polarization ratio *b* : *a*
	a	*b*	*c*	
L	90°	90°	0	—
M	55° 10′	34° 50′	90°	2·06:1
N	145 10′	55 10′	90	1:2·06

spectra of fluoranthene in fluorene taken on the *ab*-face, the observed intensity distribution among these bands has been completely changed, as is evident from Fig. 3. As it has already been mentioned that only a slight hump has appeared between 27200 and 28900 cm^{-1} in the mixed crystal spectra (Fig. 3) which corresponds to 27200 to 28900 cm^{-1} bands in pure crystal and 27000 to 30000 cm^{-1} intense bands in solution spectra. Thus it appears that this first set of bands of fluoranthene crystal arises due to *L*-axis polarized transition. This observation is in conformity with the observation made in connection with pure crystal spectra. The other bands occurring beyond 30,000 cm^{-1} in mixed crystal spectra as shown in Fig. 3 corresponding to 30,000 to 33,300 cm^{-1} bands in solution spectra are very intense. It thus appears that these do not arise due to *L*-axis polarized transition. Comparing the observed polarization ratio with the oriented gas model value (Table 4), the origin of these strong bands are assigned to be due to short axis transition as was expected from the observation of pure crystal spectra.

In case the guest and the host molecules differ in shape, there may be misalignment of the guest molecules in the host. Due to this misalignment, observed polarization ratio may show noticeable departure from the oriented gas model value. The observed deviation in the polarization ratio of our mixed crystal experiment may be explained in this way.

The different bands occurring between 3000 and 3700 Å in solution spectra seem to belong to a single system. But from the observation of the crystal spectra, both pure and mixed, it appears that these bands belong to two completely different systems and arise due to two differently polarized transitions.

References

1. Friedel R A & Orchin M, *Ultra-violet spectra of aromatic compounds* (John Wiley, New York), 1951.
2. Chaudhuri M K, *Electronic absorption and luminescence spectra of some aromatic single crystals—both pure and mixed*, D Sc thesis (University of Calcutta, Calcutta).
3. Hzell A C, Jones D W & Sowden J M, *Acta Crystallogr.*, B33 (1977), 1516-1522.
4. Chakravorty S C & Ganguly S C, *J. Phys.*, B2 (1969), 1213.

Indian Journal of Pure & Applied Physics
Vol. 18, March 1980, pp. 195-199

Vibrational Spectra of Biological Molecules : 2, 4-Diamino-6-Hydroxy Pyrimidine*

R K Goel
Department of Physics, D N College, Meerut 250 002
and
S N Sharma
Analytical Physics Section, Indian Institute of Petroleum, Dehra Dun 248 005

Received 20 *December* 1978; *revised received* 7 *May* 1979

The infrared absorption spectra of 2,4-diamino-6-hydroxypyrimidine have been recorded on Perkin Elmer-521 spectrophotometer in the region 250-4000 cm^{-1} using KBr pellet and nujol mull techniques. The spectra have been analyzed assuming C_s point group symmetry for the molecule. The fundamentals have been compared with those of pyrimidine. Assignments have been proposed and discussed. Tautomerism is also discussed.

1. Introduction

In spite of great biological importance of N-heterocyclic molecules like pyrimidine, cytosine and their derivatives, very little detailed spectroscopic work has been carried on pyrimidine compounds. However, vibrational assignments have been made for pyrimidine.[1-4] Short and Thompson[5] have reported the infrared (IR) spectra of a number of substituted pyrimidines on Perkin Elmer 12 C prism spectrometer, but no detailed assignments of the observed bands have been made. In case of 2, 4-diamino-6-hydroxy pyrimidine, they[5] recorded only 4 bands in the region 400-700 cm^{-1} and no observations were made below 400 cm^{-1}. The region 1300-1700 cm^{-1} is very important as characteristic bands of aromatic character appear in this region and the 3000-3700 cm^{-1} region is important from group-frequency considerations which may also throw light on tautomeric behaviour of the molecule. But very few bands have been recorded by Short and Thompson[5] in these regions, and these were quite insufficient to conclude about the tautomerism also. Recently, the vibrational spectra of some substituted pyrimidines[6-10] have also been studied in detail. As a part of our research project on N-heterocyclic molecules, it was thought worthwhile to undertake the detailed vibrational analysis (which has not been done so far) of the molecule 2, 4-diamino-6-hydroxy pyrimidine, which is of considerable biological importance, at present.

2. Experimental Details

Pure chemical, 2, 4-diamino-6-hydroxy pyrimidine (hereafter referred to as 2, 4 DA6 HP), obtained from M/s Tokyo Kesei Kogyo Co., Tokyo, was solid at room temperature. It was used as such without further purification. The infrared absorption spectra have been recorded on a double beam Perkin—Elmer-521 grating spectrophotometer in the region 250-4000 cm^{-1} using KBr pellet and nujol mull techniques. The observed bands have been calibrated with the help of the spectra of a thin sheet of polystyrene. A minor shift in the frequencies of some of the bands observed in the present study has been noticed as compared to the previous IR records,[5] which may be due to experimental parameters. Because of the use of high resolution grating spectrometer, many broad bands observed by Short and Thompson[5] have been resolved and many more bands have also appeared which enables us to have the detailed vibrational analysis of this molecule.

3. Results and Discussion

The structure of several pyrimidine compounds has been determined[11,12] and in all cases the molecules were found to be planar. Assuming NH_2 and OH groups as single mass points, the molecule 2, 4 DA6 HP would belong to C_s point group symmetry. Following Mulliken's recommendations,[13] the 24

* Part of this work was presented at the National Seminar on Molecular Spectroscopy and Lasers, held at Banaras Hindu University, Varanasi in January 1979.

normal modes will be distributed as 17 a' (planar) and 7 a'' (non-planar). Because of the high complexity and low symmetry of the molecule, it is difficult to interpret the spectra of such molecules. For making a complete and correct vibrational assignment, studies of the vapour phase IR spectra of this molecule along with its deuterated analogue and Raman spectra are needed. In the absence of Raman and vapour phase IR studies, the interpretation of the observed bands in the present study is based mainly on the magnitudes and ralative intensities of the observed bands and the assignments in related molecules. The observed bands in the IR spectra of 2, 4 DA6HP along with their intensities and their assignments are presented in Table 1. The fundamentals have also been compared with the fundamentals of pyrimidine in Table 1. The discussion of some of the important assignments is given in the following.

3.1 C—H Vibrations

In pyrimidine there are three CH stretching modes belonging to the a_1 species and one belonging to the b_2 species. On substitution at 4 and 6 positions, the modes ν_{13} and ν_{7b} drop in accordance with the assignments given by Nejad and Stidham[7] for pyrimidine-4, 6-d_2, the modes ν_{13} and ν_{7b} drop when substitutions are made at 4 and 6 positions. Thus, in the present case, the band observed at 3109 cm^{-1} has been assigned to C—H stretching mode ν_{20a}. Similarly a medium band observed at 1146 cm^{-1} has been assigned to ν_3 vibration corresponding to C—H in-plane bending mode. The C—H out-of-plane mode ν_{11} has been assigned at 829 cm^{-1}. This also finds support from the work of Goel *et al.*[8] in the case of some N-heterocyclic molecules.

3.2 C—C and C—N Vibrations

In the spectra of pyrimidine,[7] pairs of absorption bands at 1398 (ν_{19a}), 1466 (ν_{19b}) cm^{-1} and at 1564 (ν_{8a}), 1568 (ν_{8b}) cm^{-1} have been observed which are analogous to the pair of bands originating from e_{1u} (1485) and e_{2g} (1595) modes of benzene, observed in substituted benzenes;[14] ν_{19a} was also observed at 1382 cm^{-1} in 2-chloropyrimidine[6] and at 1391 cm^{-1} in 5-methyl-pyrimidine.[10] In the present study, these bands ν_{19a}, ν_{19b}, ν_{8a} and ν_{8b}, thus have been assigned at 1380, 1474, 1569 and 1604 cm^{-1} respectively. In analogy with the spectra of substituted benzenes, these bands are due to double bond C=C and C=N stretching vibrations of the ring. These are also in agreement with literature values.[7,8,15] The 1370 cm^{-1} Raman line of pyrimidine corresponding to the vibration ν_{14} has been identified at 1309 cm^{-1} in the present molecule. This vibration has been identified at 1305 cm^{-1} in pyrimidine -4, 6-d_2.[7]

In substituted benzenes, the frequency of one of the two ring modes ν_1 and ν_{12} reduces to $\sim$ 820 cm^{-1} while the other remains at $\sim$ 1000 cm^{-1}. ν_1 and ν_{12} modes have been identified at 768, 1000 cm^{-1} respectively in 2-amino-4-methylpyrimidine[8] and at 820, 1050 cm^{-1} respectively in 5-methylpyrimidine.[10] In view of these assignments, the bands at 789 and 989 cm^{-1} in the present molecule have been assigned to correspond to ν_1 and ν_{12} modes respectively.

The ring out-of-plane banding vibrations ν_4,ν_{16a} and ν_{16b} in pryrimidine[7] appear at 708, 399 and 344 cm^{-1} respectively. The bands observed at 724, 404 and 340 cm^{-1} in the present case have been assigned to these modes respectively. These also find support from the work of Goel *et al.*[8] and Job and Kartha[10] in substituted pyrimidines. The ring planar deformation ν_{6a} and ν_{6b} in 5-methylpyrimidine[10] were assigned at 559 and 639 cm^{-1} respectively. In the present molecule these modes are identified at 514 and 622 cm^{-1} respectively. This is also in agreement with the assignments of Goel *et al.*[16] in the case of amino-methyl pyridines.

3.3 C—X Vibrations

The X-sensitive vibration ν_{13} due to C—OH stretching (OH at 6 position) has been identified at 1254 cm^{-1} in the present molecule, while the C—OH in-plane bending ν_{9a} and out-of-plane bending ν_5 have been identified at 549 and 320 cm^{-1} respectively. These assignments are in agreement with the assignment proposed by Goel *et al.*[17] and Verma and Rai[18] in substituted phenols.

In substituted anilines,[19,20] the C—NH_2 stretching vibrations ν_2/ν_{7b} appears near 1300 cm^{-1}. Goel *et al.*[16] have also assigned this mode at 1320, 1319 and 1330 cm^{-1} in various aminomethyl pyridines. Evans[21] assigned this mode near 1278 cm^{-1} in aniline. Since the 2, 4 DA6HP molecule contains two NH_2 groups, in view of the above assignments the strong bands at 1309 and 1339 cm^{-1} have been assigned to ν_2 and ν_{7b} modes respectively.

Sanyal *et al.*[20] have assigned the X-sensitive C—NH_2 in-plane bending mode ν_{15}/ν_{18b} at 385 cm^{-1} in 3-fluoro-4-chloro aniline and Goel *et al.*[16] have assigned this mode at around 380 cm^{-1} in various aminomethyl pyridines. In view of these assignments, the medium strong bands observed at 332 and 349 cm^{-1} have been assigned to ν_{18b} and ν_{15} modes respectively. The out-of-plane C--NH_2 modes (ν_{10b} and ν_{17a}) are also X-sensitive in the

Table 1—Analysis of the IR Absorption Spectra of 2, 4 DA6HP and Correlation of Fundamentals with Those of Pyrimidine

Symmetry species	Pyrimidine (Ref. 7)		2, 4-Diamino-6-hydroxy pyrimidine				Assignment
			KBr		Nujol		
	Vibration number	Frequency cm^{-1}	Frequency cm^{-1}	Int.	Frequency cm^{-1}	Int.	
			296	mw			ν_{6b}-ν_5
			309	m			ν_{11}-ν_{6b}
a''	5	980	320	ms			C—X o.p.b. (γC—OH)
a'	18*b*	1071	332	ms			C—X i.p.b. (β C—NH_2)
a''	16*b*	344	340	ms			C—C o.p.b., e_{2u} (404)
a'	15	1159	349	ms	349	vw	C—X i.p.b (β C—NH_2)
a'			363	ms	360	mw	γ (O—H)
			382	m	380	m	NH_2 twist-NH_2 wag.
a''			390	m	390	vw	γ C=O out of phase
a''	16*a*	399	404	s	404	ms	C—C o.p.b, e_{2u} (404)
			426	vw	426	vvw	2 × NH_2 torsion
					454	w	2 × NH_2 torsion
a'	6*a*	678			514	w	C—C i.p.b. e_{2g} (608)
a'	9*a*	1139	549	ms	544	m	C—X i.p.b. (β C—OH)
a'					566	wb	β C=O in phase
a'	6*b*	623	622	m	616	ms	C—C i.p.b, e_{2g} (608)
			650	vvw			2 ν_5
a'			665	s	667	s	NH_2 wag.
a'			674	s			NH_2 wag.
a''	4	708			724	s	C—C o.p.b.
			764	ms			ν_{16a} + ν_{15}
a'	1	992	789	vs	784	s	C—C stretching ring-breathing
a''	11	811	829	ms	824	msb	C—H o.p.b.
a'	12	1065	989	vs	984	s	C—C i.p.b.
			1044	s	1039	ms	NH_2 twisting
			1109	s	1104	s	NH_2 twisting
a'	3	1225	1146	vw	1146	mb	C—H i.p.b.
a'			1168	m	1164	mb	β O—H
a'	13	3038	1254	vvs	1254	s	C—X stretch (ν C—OH)
a'	2, 14	3052, 1370	1309	vvs	1309	s	C—X stretch (ν C—NH_2), C—C stretch
a'	7*b*	3086	1339	m	1344	vw	C—X stretch (ν C—NH_2),
a'	19*a*	1398	1380	vvs	1388	vs	C—C stretch, ν CN
			1414	vvw	1412	vw	ν_1 + ν_{6b}
					1456	sb	ν_{11} + ν_{6b}
a'	19*b*	1466	1474	vs	1472, 1478	s	C—C stretch, ν CN
					1489	ms	OH + ν_5
					1494	ms	OH + ν_{18b}
			1508	vw	1502	w	ν_3 + ν_{15}
			1514	m	1514	w	ν_1 + ν_4
					1532	m	ν_{12} + ν_{9a}
					1550	m	ν_4 + ν_{11}
a'	8*a*	1564			1569	vw	C—C stretch, ν CN
a'	8*b*	1568	1604	sb	1602	mb	C—C stretch, ν CN
			1624	vw	1624	vw	ν_1 + ν_{11}
			1634	vw	1630	m	ν_2 + ν_5' ν_{14} + ν_5
a'			1644	m	1644	ms	NH_2 scissoring
a'			1662	ms	1663	ms	NH_2 scissoring
			1679	vw			β OH + ν_{6a}

(Table 1 Contd.)

Table 1—Analysis of the IR Absorption Spectra of 2,4 DA6HP and Correlation of Fundamentals with Those of Pyrimidine (Contd.)

Symmetry Species	Pyrimidine (Ref. 7) Vibration number	Pyrimidine (Ref. 7) Frequency cm^{-1}	2, 4-Diamino-6-hydroxy pyrimidine KBr Frequency cm^{-1}	KBr Int.	Nujol Frequency cm^{-1}	Nujol Int.	Assignment
a'			1694	vw	1692	ms	ν (6 C=O)
			1716	vw	1714	ms	$\nu_{12} + \nu_4$
			1731	m	1729	mb	$\nu_{19} + \nu_{15}$
			1762	w	1762	mw	$\nu_3 + \nu_{6b}$
			1794	w	1796	mw	β OH + ν_{6b}
					1808	vw	ν_3 + NH_2 wag.
					1816	vw	ν_3 + NH_2 wag.
					1829	vw	β OH + NH_2 wag.
			1844	vw	1844	vw	β OH + NH_2 wag.
			1864	vw	1862	mw	$\nu_3 + \nu_4$
					2254	mb	$\nu_{13} + \nu_{12}$
			2269	mb	2269	vw	$\nu_1 + \nu_{19b}$
					2469	vw	β OH + ν_2
					2719	vw	$\nu_{19a} + \nu_{7b}$
					2984	mw	$\nu_{8b} + \nu_{19a}$
a'	20a	3074			3109	mw	ν C—H
a'			3169	vw	3169	vw	ν (N—H)
a'			3235	vw	3220	vvw	2 × ν_{8b}
a'			3300	vw	3300	vvw	ν (N—H)
a'					3361	mw	ν (N—H) sym.
a'					3439	mb	ν (N—H) sym.
a'					3519	m	ν (N—H) asym.
a'					3561	m	ν (N—H) asym.
					3579	vw	2 ν_{19a} + ν_{11}
					3595	vw	2 × ν_2 + ν_{12}
					3659	vw	$\nu_{20a} + \nu_{9a}$
					3684, 3719	ms	ν (O—H)
					3818	mb	ν NH + γ C=O
					3954	m	ν NH + ν_{6a}

s, strong; vs, very strong; vvs, very very strong; ms, medium strong; mw, medium weak; w, weak; vw, very weak; vvw, very very weak; b, broad; ν, stretching; β, in-plane bending; γ, out-of-plane deformation; i.p.b., in-plane bending; and o.p.b., out-of-plane bending.

present case. Evans[21] has assigned the C—NH out-of-plane mode at 233 cm^{-1} in aniline, and Green *et al.*[22] assigned this mode at still lower frequency. Thus these modes could not be observed in the present molecule as these lie below the region under study.

3.4 OH Group Vibrations

For molecules containing OH group, the OH valence oscillation appears in the range 3500-3700 cm^{-1}. In phenol[23] this mode has been identified at 3628 cm^{-1}. In the present case, the medium strong band, at 3684/3719 cm^{-1} has been assigned to this mode. There is some possibility of interaction between C—OH stretching and O—H in-plane bending vibrations, but the lower of the two frequencies has been attributed mainly due to the O—H deformation mode. Mecke and Rassmy[24] have reported a band at 1180 cm^{-1} which possesses a strong O—H character. Green *et al.*[25] have assigned the bands at 1178, 1189 and 1180 cm^{-1} to this mode in 2, 6- ; 2, 5- and 3, 4-dichlorophenols respactively. In conformity with these assignments the medium band observed at 1168 cm^{-1} in 2, 4 DA6HP has been assigned to O—H in-plane bending mode. The O—H out-of-plane bending vibration has been identified at 363 cm^{-1} in the present molecule while Green *et al.*[25] have assigned this mode at 400, 366 and 312 cm^{-1} in three dichlorophenols.

3.5 NH_2 Group Vibrations

In most of the primary aromatic amines, there occur two bands in the region 3350-3550 cm^{-1}, which are associated with N—H stretching vibrations. It has been pointed out by Bellamy[14] that in N-octamide in chloroform solution, the NH_2 free absorption occurs at 3530 cm^{-1} and 3415 cm^{-1}, but it also shows additional bands at 3498, 3345, 3300 and 3182 cm^{-1}. This suggests occurrence of different

types of simultaneous association of free and bonded NH bonds. In solid states, the pattern simplifies and gives two broader NH peaks near 3350 cm^{-1} and 3164 cm^{-1}. In view of these assignments we have assigned the bands observed at 3169, 3300, 3361, 3439, 3519 and 3561 to N—H stretching modes. The appearance of additional bands at 3169 and 3300 cm^{-1} shows that one H-atom in NH_2 group is loosely bound which may join with the nitrogen of the ring and thus may exhibit tautomerism. However, in the absence of other confirmatory data the existence of tautomerism is not very much conclusive. Further, a medium strong band at 1694 cm^{-1} has been identified in C=O region corresponding to 6 C=O stretching mode and C=O in-plane and out-of-plane bending modes have also been identified at 566 and 390 cm^{-1} respectively in the present molecule, which are in agreement with literature values.[8,20] This indicates that the tautomerism is due to OH group at 6-position. However, as O—H stretching and bending vibrations also appear, the existence of tautomerism may be taken to be very weak.

The NH_2 scissoring mode has been suggested to lie in the region 1590-1650 cm^{-1}.[14,26] The two NH_2 scissoring modes due to two NH_2 groups have been identified at 1644 and 1662 cm^{-1} in the present case. The NH_2 twisting frequency lies around 1060 cm^{-1}.[21] In 2, 4 DA6HP, because of two NH_2 groups, the interaction of similar frequencies is possible which may modify these modes. Thus the strong bands observed at 1044 and 1109 cm^{-1} have been assigned to this mode. This also finds support from the literature values.[15,21]

The NH_2 wagging vibration has been identified at 670 cm^{-1} by Evans[21] and at 655 cm^{-1} by Goel *et al.*[8] Therefore, the bands observed at 655 and 674 cm^{-1} in the 2, 4 DA6HP have been assigned to this mode. The NH_2 torsion mode lies below the region under study. However, the bands observed at 426 and 454 cm^{-1} in the spectra of the molecule presently under study have been assigned to the first overtone of the NH_2 torsional mode as has been done by Evans[21] in the case of aniline.

Acknowledgement

Authors are thankful to Dr S P Gupta, Principal, D N College, Meerut for providing necessary facilities. One of the authors (RKG) is thankful to the University Grants Commission, New Delhi, for financial assistance.

References

1. Ito M, Shimada R, Kuraishi T & Mizushima W, *J. chem. Phys.*, **25** (1956), 597.
2. Lord R C, Marson A J & Miller F A, *Spectrochim. Acta*, **9** (1957), 113.
3. Simmons J D & Innes K K, *J. molec. Spectrosc.*, **13** (1964), 435.
4. Sbrana G, Adembri G & Galifano S, *Spectrochim. Acta*, **22** (1966), 1831.
5. Short L N & Thompson H W, *J. chem. Soc.*, (1952), 168.
6. Sarma Y A, *Spectrochim. Acta*, **30A** (1974), 1801.
7. Nejad F M & Stidham H D, *Spectrochim. Acta*, **31A** (1975), 1433.
8. Goel R K, Sanyal Nitish K & Srivastava S L, *Indian J. pure appl. Phys.*, **14** (1976), 842.
9. Allenstein E, Kiemle P, Weldin J & Podszun W, *Spectrochim. Acta*, **33A** (1977), 189.
10. Job V A & Kartha S B, *Proc. Indian Acad. Sci.*, **85A** (1977), 476.
11. Lancaster J E & Stoicheff B P, *Can. J. Phys.*, **34** (1956), 1016.
12. Wheatley P J, *Acta crystallogr.*, **13** (1960), 80.
13. Mulliken R S, *J. chem. Phys.*, **23** (1955), 1997.
14. Bellamy L J, *The infrared spectra of complex molecules* (Chapman & Hall, London), 1975.
15. Sanyal Nitish K, Srivastava S L & Goel R K, *Indian J. Phys.*, **51B** (1977), 108.
16. Goel R K, Gupta S K & Sharma S N, *Indian J. pure appl. Phys.*, Communicated.
17. Goel R K, Kansal K P & Sharma S N, *Indian J. pure appl. Phys.*, **17** (1979), 778.
18. Verma V N & Rai D K, *Appl. Spectrosc.*, **24** (1970), 445.
19. Singh V B, Singh R N & Singh I S, *Spectrochim. Acta*, **22** (1966). 927.
20. Sanyal Nitish K, Srivastava S L & Goel R K, *Indian J. pure appl. Phys.*, **16** (1978), 719.
21. Evans J C, *Spectrochim. Acta*, **16** (1960), 428.
22. Green J H S, Harrison D J & Kynaston W, *Spectrochim. Acta*, **27A** (1971), 793.
23. Evans J C, *Spectrochim. Acta*, **16** (1960), 1382.
24. Mecke R & Rassmy G, *Z. Electrochim.*, **59** (1955), 866.
25. Green J H S, Harrison D J & Kynaston W, *Spectrochim. Acta*, **28A** (1972), 33.
26. Rao C N R, *Chemical applications of infrared Spectroscopy* (Academic Press, New York), 1963.

Communications

Emission Spectrum of Copper Chloride Molecule

P Meenakshi Raja Rao

Spectroscopy Division, Bhabha Atomic Research Centre
Trombay, Bombay 400 085

Received 12 *March* 1979; *revised received* 7 *May* 1979

Details of a large number of new bands observed in the region of 5900-6800 Å in the emission spectrum of copper chloride molecule are described. The rotational analysis of the 0-0 band of the $A-X$ system is also presented.

Recently, a new band system of CuCl in the region 6900-7500 Å, is reported[1] involving transition from a new excited state to the ground state. During these investigations, a number of new bands have been observed in the region 5900-6800 Å. Some of these bands are degraded to the red, while some others are degraded to the violet.

As is well known, natural copper chloride is a mixture of four isotopic species, viz. $^{63}Cu^{35}Cl$, $^{65}Cu^{35}Cl$, $^{63}Cu^{37}Cl$ and $^{65}Cu^{37}Cl$, their relative abundance being 7 : 3 : 2·3 : 1. In addition, there is an overlap of the red and violet degraded bands, which makes the spectra look complicated. Hence it became necessary to record the spectra of copper chloride with enriched isotopes.

At the time of carrying out this work, no complete rotational analysis of the $A-X$ system was available, and the nature of the A state also remained to be established. For reasons mentioned already, the spectrum of enriched $^{63}Cu^{35}Cl$ molecule, has also been recorded. At the dispersion and resolution available to us only the 0-0 band was amenable for a complete rotational analysis. The 1-1 band also has been partially analyzed.

Electrodeless discharge tubes containing milligram quantities of enriched isotopes of copper and chlorine were prepared as described in Ref. 2. ^{63}Cu and ^{65}Cu were taken in the form of CuO, each isotope of copper enriched to 99·6% and ^{35}Cl and ^{37}Cl in the form of NaCl, ^{35}Cl enriched to 95·5% and ^{37}Cl enriched to 96·5%. The spectra were excited by a microwave oscillator (2450 MHz). The spectra of $^{63}Cu^{35}Cl$, $^{65}Cu^{35}Cl$ and $^{63}Cu^{37}Cl$ were photographed in juxtaposition (spectral region 5900-6800 Å) at a dispersion of 2·5 Å/mm. The 0-0 and 1-1 bands of $^{63}Cu^{35}Cl$ were photographed at 1·2 Å/mm. The measurements on the band head as well as the rotational lines were carried out on an Abbe comparator. The accuracy of the measurements is $\pm 0{\cdot}02$ cm^{-1} for sharp rotational lines and $\pm 0{\cdot}1$ cm^{-1} for the well defined strong band heads.

Spectrum in the region of 5900-6800 Å—Fig. 1 is a reproduction of a part of this spectrum showing some of the intense bands belonging to three isotopic species of CuCl. The data on the band heads degraded to the red along with their isotope shifts are given in Table 1, while similar data on the violet degraded bands are given in Table 2. The fact that the bands show shifts for both copper and chlorine isotopic changes goes to prove that these atoms are involved in the emitter. Therefore, it is concluded that the emitter is the CuCl molecule. Finally, a preliminary analysis of the rotational structure reveals that they arise from singlet transitions.

Rotational analysis of the $A-X$ *system*—Fig. 2 shows the 0-0 band at 5262·4 Å belonging to the $A-X$ system of $^{63}Cu^{35}Cl$ molecule. The band is double headed and from the rotational analysis it is concluded that the transition is $^1\Pi-{}^1\Sigma$ type, $^1\Sigma$

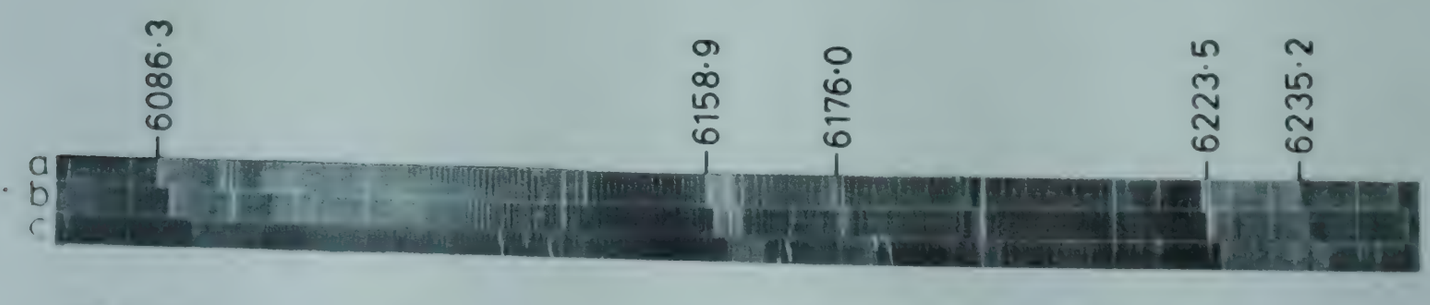

Fig. 1—Emission spectrum of CuCl molecule in the region 5900-6800 Å [(a), $^{63}Cu^{35}Cl$; (b), $^{65}Cu^{35}Cl$; (c) $^{63}Cu^{37}Cl$]

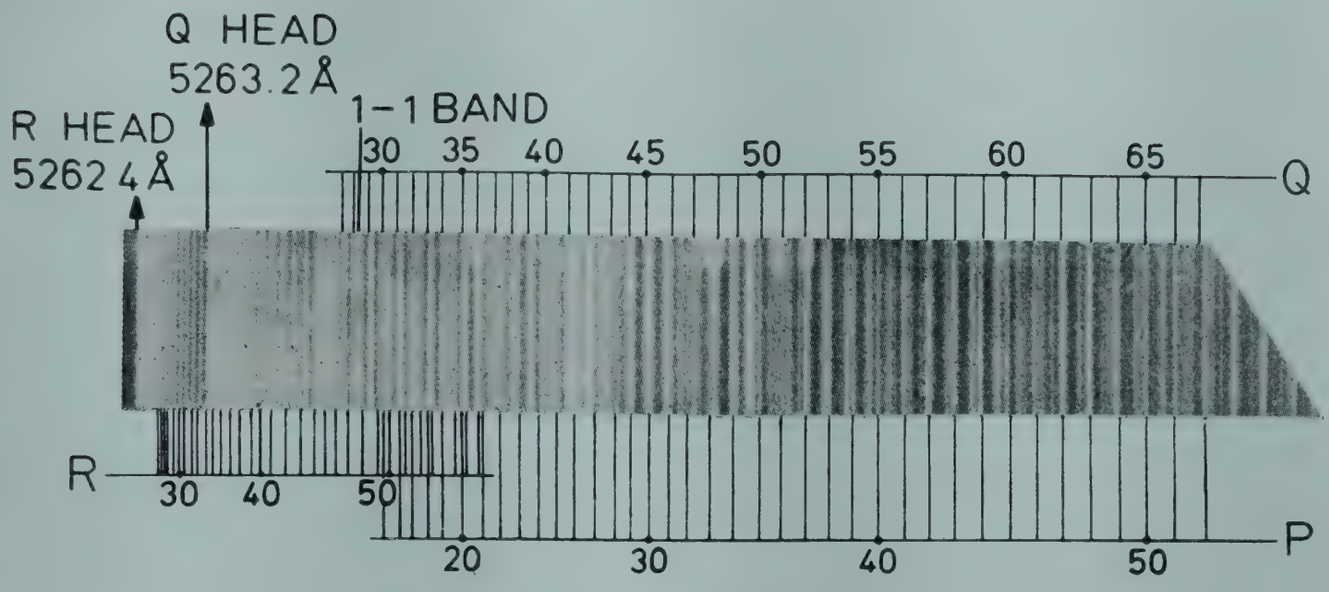

Fig. 2—0-0 Band at 5262-4 Å of $A—X$ system of the spectrum of $^{63}Cu^{35}Cl$ molecule

Table 1—New Red-degraded Bands of CuCl Molecule

$^{63}Cu^{35}Cl$		$^{65}Cu^{35}Cl$		$^{63}Cu^{37}Cl$		Isotope shift $\Delta\nu(cm^{-1})$	
λ(Å) (air)	$\nu(cm^{-1})$ (vac.)	λ(Å) (air)	$\nu(cm^{-1})$ (vac.)	λ(Å) (air)	$\nu(cm^{-1})$ (vac.)	Cu	Cl
5866·9	17040·1	5869·1	17033·6			+6·5	
5912·5	16908·6	5914·8	16902·2	5919·2	16889·5	+6·4	+ 9·1
6036·1	16562·4	6037·6	16558·2	6041·0	16549·1	+4·2	+13·3
6086·2	16426·1	6088·2	16421·2	6091·1	16412·7	+4·9	+13·4
6158·8	16232·4	6160·0	16229·2	6162·2	16223·5	+3·2	+ 8·9
6222·8	16065·5	6223·7	16063·2	6225·1	16059·6	+2·3	+ 5·9
6260·0	15969·9	6261·0	15967·5	6263·1	15962·1	+2·4	+ 7·8
6275·9	15929·5	6276·1	15929·0	6276·7	15927·5	+0·5	+ 2·0
6286·6	15902·4	6287·1	15901·3	6287·8	15899·3	+1·1	+ 3·1
6342·9	15761·4	6343·0	15760·9	6343·5	15759·0	+0·5	+ 1·6
6349·4	15745·2	6349·7	15743·7	6350·3	15743·0	+1·5	+ 2·2
6360·1	15718·6	6360·2	15718·4	6360·4	15718·0	+0·2	+ 0·6
6383·7	15660·6	6384·7	15658·0	6386·5	15653·6	+2·6	+ 7·0
6413·6	15587·7	6413·3	15588·2	6412·8	15589·5	−0·5	− 1·8
6415·2	15583·8	6414·6	15585·0	—	—	−1·2	—
6430·5	15546·7	—	—	6430·3	15547·1	—	− 0·4
6481·0	15425·5	6481·2	15425·0	6481·7	15423·7	+0·5	+ 1·8
6483·0	15420·7	6483·1	15420·6	6483·6	15419·4	+0·1	+ 1·3
6530·4	15308·5	6530·6	15308·4	6530·1	15309·4	- 0·1	− 0·9
6574·5	15206·2	6573·8	15207·7	6572·2	15211·3	−1·5	− 5·1
6625·9	15088·2	6527·6	15088·4	6624·9	15090·4	−0·2	− 2·0
6674·7	14977·6	6673·5	14980·5	6674·5	14889·1	−2·9	−11·5
6720·6	14875·5	6719·4	14878·2	6716·0	14885·7	−2·7	−10·2
6775·6	14754·7	—	—	6785·0	14734·3	—	+20·4

Table 2—New Violet-degraded Bands of CuCl Molecule

$^{63}Cu^{35}Cl$		$^{65}Cu^{35}Cl$		$^{63}Cu^{37}Cl$		Isotope shift $\Delta\nu(cm^{-1})$	
λ(Å) (air)	$\nu(cm^{-1})$ (vac.)	λ(Å) (air)	$\nu(cm^{-1})$ (vac.)	λ(Å) (air)	$\nu(cm^{-1})$ (vac.)	Cu	Cl
6043·2	16542·8	6052·5	16536·8	6052·3	16518·0	+ 0·6	+24·8
6055·4	16509·8	6061·9	16492·0	—	—	+17·8	—
6176·0	16187·5	6177·4	16183·5	6180·7	16174·9	+ 4·0	+12·6
6235·2	16033·4	6136·2	16030·9	6138·8	16024·3	+ 2·5	+ 9·1
6247·8	16001·3	6249·1	15997·8	6251·9	15990·8	− 3·5	+10·5
6516·2	15342·0	6515·3	15344·3	—	—	− 2·3	

Table 3—Vacuum Wavenumbers and J Assignments of the 0-0 Band of $A-X$ System of $^{63}Cu^{35}Cl$

J	$R(J)$	$O(J)$	$P(J)$	J	$R(J)$	$Q(J)$	$P(J)$
11	7	$18994{\cdot}1_0$		40	$18992{\cdot}4_8$	$18978{\cdot}6_4$	$18965{\cdot}3_3$
12		$93{\cdot}7_0$	$18989{\cdot}6_7$	41	$91{\cdot}9_5$	$78{\cdot}0_4$	$64{\cdot}2_4$
13		$93{\cdot}3_0$	$88{\cdot}9_9$	42	$91{\cdot}5_1$	$77{\cdot}1_6$	$63{\cdot}0_8$
14		$92{\cdot}9_2$	$88{\cdot}3_0$	43	$91{\cdot}0_4$	$76{\cdot}3_4$	$61{\cdot}9_1$
15		$92{\cdot}4_8$	$87{\cdot}6_3$	44	$90{\cdot}4_9$	$75{\cdot}3_9$	$60{\cdot}6_7$
16		$91{\cdot}9_5$	$86{\cdot}5_2$	45	$89{\cdot}6_7$	$74{\cdot}5_3$	$59{\cdot}5_6$
17		$91{\cdot}5_1$	$85{\cdot}8_9$	46	$89{\cdot}5_0$	$73{\cdot}5_8$	$58{\cdot}3_5$
18		$91{\cdot}5_1$	$85{\cdot}1_6$	47	$88{\cdot}9_9$	$72{\cdot}8_4$	$56{\cdot}7_6$
19		$91{\cdot}0_4$	$85{\cdot}1_0$	48	$88{\cdot}0_3$	$71{\cdot}8_9$	$55{\cdot}8_7$
20		$90{\cdot}4_9$	$83{\cdot}9_0$	49	$87{\cdot}4_1$	$70{\cdot}6_2$	$54{\cdot}6_2$
21		$90{\cdot}1_0$	$82{\cdot}9_5$	50	$86{\cdot}8_2$	$69{\cdot}5_8$	$53{\cdot}3_3$
22		$89{\cdot}6_7$	$82{\cdot}2_9$	51	$86{\cdot}2_1$	$68{\cdot}4_8$	$51{\cdot}4_2$
23		$88{\cdot}9_9$	$81{\cdot}5_1$	52	$85{\cdot}4_8$	$67{\cdot}5_0$	$49{\cdot}9_1$
24		$88{\cdot}6_0$	$80{\cdot}4_3$	53	$84{\cdot}5_6$	$66{\cdot}4_1$	$48{\cdot}6_9$
25		$88{\cdot}3_0$	$79{\cdot}8_9$	54	$83{\cdot}8_9$	$65{\cdot}3_3$	$47{\cdot}2_5$
26		$87{\cdot}6_3$	$79{\cdot}1_4$	55		$64{\cdot}2_4$	$45{\cdot}8_9$
27	$18996{\cdot}6_7$	$87{\cdot}1_0$	$78{\cdot}0_4$	56		$63{\cdot}7_1$	$44{\cdot}4_2$
28	$96{\cdot}4_5$	$86{\cdot}5_2$	$77{\cdot}1_6$	57		$61{\cdot}9_1$	$43{\cdot}7_3$
29	$96{\cdot}0_9$	$86{\cdot}2_1$	$76{\cdot}3_4$	58		$60{\cdot}6_7$	$40{\cdot}9_6$
30	$95{\cdot}8_8$	$85{\cdot}4_8$	$75{\cdot}3_9$	59		$59{\cdot}3_6$	$39{\cdot}5_2$
31	$95{\cdot}7_4$	$84{\cdot}7_6$	$74{\cdot}5_3$	60		$58{\cdot}3_5$	$37{\cdot}9_7$
32	$95{\cdot}3_4$	$84{\cdot}3_8$	$73{\cdot}5_8$	61		$57{\cdot}1_5$	$36{\cdot}5_2$
33	$95{\cdot}1_6$	$83{\cdot}5_9$	$72{\cdot}6_5$	62		$55{\cdot}8_7$	$34{\cdot}9_9$
34	$94{\cdot}7_6$	$82{\cdot}9_5$	$71{\cdot}6_4$	63		$54{\cdot}6_2$	$33{\cdot}4_4$
35	$94{\cdot}4_5$	$82{\cdot}2_8$	$70{\cdot}6_2$	64		$53{\cdot}3_3$	$31{\cdot}8_8$
36	$94{\cdot}1_0$	$81{\cdot}5_1$	$69{\cdot}5_8$	65		$52{\cdot}0_4$	$30{\cdot}3_0$
37	$93{\cdot}7_0$	$80{\cdot}8_9$	$68{\cdot}4_8$				
38	$93{\cdot}3_0$	$80{\cdot}2_1$	$67{\cdot}5_0$				
39	$92{\cdot}9_2$	$79{\cdot}4_9$	$66{\cdot}4_1$				

Table 4—Combination Differences in the 0-0 Band of the A—X System of $^{63}Cu^{35}Cl$

J	$\Delta_1F''(J)$		$\Delta_1F'(J)$	
	$R(J)-Q(J+1)$	$Q(J)-P(J+1)$	$R(J)-Q(J)$	$Q(J+1)$ $-P(J+1)$
35	12·94	12·66	12·21	11·93
36	13·21	13·03	12·59	12·41
37	13·44	13·39	12·81	12·76
38	13·85	13·85	13·04	13·04
39	14·28	14·12	13·47	13·31
40	14·44	14·40	13·84	13·80
41	14·88	14·96	14·00	13·08
42	15·19	15·25	14·37	14·43
43	15·64	15·67	14·69	14·72
44	15·96	15·83	15·10	15·17
45	16·09	16·28	15·14	15·23

Table 5—Molecular Constants (in cm^{-1}) of $A\,^1\Pi$ and $X\,^1\Sigma$ States of $^{63}Cu^{35}Cl$

	$X\,^1\Sigma$ State	$A\,^1\Pi$ State
B_0	0·1778	0·1682
B_1	—	0·1674
D_0	$1·38\times10^{-7}$	$1·057\times10^{-7}$
ν_0(0-0)	18994·5	
ν_0(1-1)	18985·8	

being the ground state. The line positions and the J assignments of the different branches are given in Table 3. The rotational constants B and D are determined for both the states by adopting a least square fit method using $\Delta_1 F$ as well as $\Delta_2 F$ values. While forming the combination differences $R(J) - Q(J+1)$ on one hand and $Q(J)-P(J+1)$ on the other, no combination defect is observed as can be seen from Table 4, from which it can be concluded that the λ-doubling in the A ($^1\Pi$) state is very small. Hence taking average B value from Δ_1F and Δ_2F values is justified. The B_0'' and D_0'' values obtained agree well with the earlier reported values.

The Q branch of 1-1 band also could be identified and from the graph of $Q(J)$ vs $J(J+1)$, the slope which gives $(B_1' - B_1'')$, is determined. B_1' is calculated by using the earlier known value of B_1'' (Ref. 3). The band origin for 1-1 band is also calculated from the same graph. For the 0-0 band, the band origin is calculated from the Q branch as well as from the graph of $R(J-1) + P(J) - 2(B'-B'')\,J^2$ vs J^2. Both values agree very well. The constants obtained are listed in Table 5.

References

1. Meenakshi Raja Rao P & Ramakoteswara Rao P, *Spectrosc. Lett.*, 79 (1974), 463.
2. Ramakoteswara Rao P & Brody J K, *J. chem. Phys.*, 35 (1961), 776.
3. Ramakoteswara Rao P, Brody J K & Asundi R K, *Can. J. Phys.*, 40 (1962), 412.

Notes

On the Debye Characteristic Temperatures of Some Crystals with NaCl-type Structure

(Miss) Debasri Basu & J K D Verma

Saha Institute of Nuclear Physics, Calcutta 700 009

Received 1 *February* 1979; *revised received* 19 *March* 1979

The values of Debye characteristic temperatures of eight cubic crystals obtained by different methods [*Indian J. pure appl. Phys.*, 16 (1978), 693] are compared with the 'exact' values obtained using parametrized tables. It is observed that the values obtained using Verma-Aggarwal Approximation [*J. appl. Phys.*, 46 (1975), 2841] are closer in agreement with the exact values than those by other methods.

Recently, Subhadra and Sirdeshmukh[1] have calculated the Debye characteristic temperatures of eight cubic crystals by different methods. They found that though the differences in the values of the Debye temperature by various approximations are not large, the values calculated using Verma-Aggarwal Approximation[2] (VAA) seem to be in better agreement with those obtained using the series expansion method. It thus appears that these workers have assumed that the series expansion method yields the 'exact' values of Debye temperatures and, hence, compared the relative accuracies of all the other methods with respect to this method.

It may be pointed out that the 'exact' values of the Debye temperature can be calculated only by numerical integration of the cubic secular equation[3] or by using parametrized tables based on extensive computer calculations by DeLaunay[4] and by Overton and Schuch.[5] With the help of these tables[5], it is possible to calculate the Debye temperature of any cubic crystal with an accuracy of greater than $\pm$ 1 in 10^5. Using these tables, any error in the Debye temperature is essentially determined by the error in the input data, i.e. elastic constants and density of the solid.

To compare the relative accuracies of the VAA and the series expansion methods, exact values of the Debye temperatures of eight cubic crystals calculated using Overton and Schuch[5] tables are given in Table 1. The values of Zener anisotropy parameter (η) are also listed in Table 1. The exact value of Debye temperature of KCN could not be computed as the existing DeLaunay[4] or Overton and Schuch[5] tables do not encompass the range of elastic constants encountered in this case.

Table 1—Debye Temperatures of Some Cubic Crystals by Different Methods

(η is the Zener anisotropy parameter)

Crystal	η	Debye temperature, K		
		VAA	Series expansion	Exact
NH_4I	0·2376	118·17	114·53	116·17
CsF	0·4646	157·96	157·43	157·71
MnS	1·5072	419·40	420·23	419·50
BaO	0·8947	290·86	290·84	290·86
MnO	1·3929	532·76	532·98	532·82
CoO	1·4286	513·22	513·58	513·40
NiO	1·4483	577·48	577·65	577·48
KCN	0·4002	122·81	122·57	—

It is seen from Table 1 that the Debye temperatures obtained using VAA are closer to 'exact' values than those obtained using the series expansion. Only in the case of NH_4I, where anisotropy is large, the relative error for the series expansion value is about 1·4% while that for the VAA is 1·7%. This further substantiates the superiority of VAA over other approximations[1] as reported earlier for a number of cubic elements,[2] semiconducting compounds[2] and alkali halides.[6] Moreover, VAA is less cumbersome than the series expansion method. In cases like KCN where Overton and Schuch[5] tables cannot be used and direct numerical integration is not feasible, the VAA values can be taken as 'exact'. Preliminary results indicate that VAA can also be used with advantage for calculating the Debye temperatures of non-cubic crystal; as also where parametrized tables are not available for computing exact values.[7]

References

1. Subhadra K G & Sirdeshmukh D B, *Indian J. pure appl. Phys.*, 16 (1978), 693.
2. Verma J K D & Aggarwal M D, *J. appl. Phys.*, 46 (1975), 2841.
3. Alers G A, *Physical acoustics*, edited by W P Mason (Academic Press, New York) 3B (1965), 1.
4. DeLaunay J, *J. chem. Phys.*, 30 (1959), 91.

5. Overton (Jr) W C & Schuch A F, *Los Alamos Scientific Lab. Rep. Nos.* 3162 & 3615, unpublished.
6. Verma J K D & Aggarwal M D, *J. appl. Phys.*, 47 (1976), 2778.
7. Verma J K D, Basu D & Aggarwal M D, unpublished work.

Studies On the Stability & Strength of fcc Aluminium Using Morse Potential

A K Mitra
Department of Physics, Regional Engineering College
Durgapur 9, West Bengal

&

P K Sengupta
Department of Physics, University of Burdwan
Burdwan, West Bengal

Received 28 *April* 1979

Mechanical stability of a perfect fcc crystal lattice of aluminium is studied following the idea of Born and Furth that the real stability condition will be the condition that the lattice strongly stressed in one direction must be stable against any small deformation in any arbitrary direction. The empirical Morse interatomic potential function determined by Girifalco and Weizer is used to calculate the energy density of the lattice and this quantity is minimized at a given main deformation and arbitrary additional deformations. Under an uniaxial tensile stress, a range of stability is obtained. The theoretical strength and corresponding strain are compared and found to agree with experimental values.

High-strength composite materials find widespread applications in advanced structural fields. These composite materials owe their strength to the strong crystalline metallic whiskers which are used as reinforcements in a comparatively weaker matrix. Exceedingly thin crystal whiskers have been seen to possess very high tensile strength and in most of the cases, they are almost perfect lattices devoid of any observable imperfections. So to tailor materials for specific structural applications, it is useful to study the stability and strength of perfect lattices of metal crystals. The present analysis on fcc aluminium has been motivated by these considerations.

Several investigators have attempted to study the stability and to calculate the tensile strength of crystals on the basis of the lattice theory.[1] But we have used the idea put forward by Born and Furth[2] which appears to be the most realistic and sound. The range of lattice parameters within which the Born stability criteria are satisfied denotes the stable region and the points where they are violated are recognized as the start of instability. From the coordinates of these transition points, we calculate the theoretical strength of the crystal under given loading conditions.

As a model for interatomic interaction we choose the central pairwise Morse potential function with the parameters determined by Girifalco and Weizer.[3] The Morse potential function has previously been successfully used to study the elastic properties of metals[3,4] and to calculate tensile strength of bcc iron.[5] In this investigation, studies are made on a perfect fcc lattice of aluminium under uniaxial stresses (tension and compression) along $\langle 100 \rangle$ axis.

Born stability criteria—For a crystal lattice homogeneously deformed under applied forces to be stable, the total system (crystal plus applied forces) potential energy must be at a minimum. So if on the primary deformation is superposed, an additional arbitrary, but very small homogeneous deformation, the total system potential energy is increased.

For the lattice to be in equilibrium in the initial state there must be an equilibrium of forces between the externally applied forces and the internal forces resulting from the mutual potential energy of the atoms. Thus

$$F_i^0 = \left(\frac{\partial E}{\partial a_i} \right)_0 \qquad \ldots(1)$$

a_i's being the lattice parameters; $i = 1, 6$

The energy may be written in the form

$$E = E^0 + \sum_i F_i^0 \, \delta a_i + \frac{1}{2} \sum_{i,j} F_{ij}^0 \, \delta a_i \, \delta a_j + \ldots, \qquad \ldots(2)$$

neglecting higher terms where

$$F_{ij}^0 = \left(\frac{\partial^2 E}{\partial a_i \, \partial a_j} \right)_0 \qquad \ldots(3)$$

The condition for E^0 to be a minimum with respect to any arbitary additional deformation δa_i is that the second term on the right-hand side of Eq. (2) must be equal to the work done by the external forces, and that the third term must be positive. The first of these conditions is automatically satisfied by the equilibrium conditions given by Eq. (1). The double sum in the third term will be positive for any arbitrary deformation if and only if the principal minors of F_{ij} are all positive. For a cubic crystal under uniaxial stress where the atoms interact through a central pairwise potential function, the necessary and sufficient conditions for the lattice to be in stable equilibrium in terms of the Born criteria are

$$F_{11} > 0, \; F_{22} > 0, \; F_{12} > 0, \; F_{23} > 0, \; F_{22} - F_{23} > 0$$

and $F_{11}(F_{22} + F_{23}) - 2F_{12}^2 > 0$

Morse potential function—The potential energy of two atoms in the lattice separated by a distance r is given in terms of Morse function as

$$\phi(r)=D\,[\exp\{-2\alpha(r-r_0)\}-2\exp\{-\alpha(r-r_0)\}] \quad ...(4)$$

where D, α and r_0 are constants. These parameters are determined[3] using experimental values for the energy of vaporization, the lattice constant and the compressibility.

The energy per unit cell of the lattice is

$$E = \frac{n}{2}\sum_r \phi(r), \quad ...(5)$$

n being the number of atoms per unit cell.

Numerical calculations—We investigated the behaviour of an fcc perfect crystal lattice of aluminium when stressed along $\langle 100 \rangle$ crystallographic axis. As there are no applied shear stresses, the lattice parameters a_4, a_5 and a_6 will retain their initial values of $\pi/2$, a_1 will elongate, a_2 and a_3 will contract keeping $a_2=a_3$. Here

$$r^2 = 1/4\,(l_1^2\,a_1^2 + l_2^2\,a_2^2 + l_3^2\,a_3^2) \quad ...(6)$$

where r is the position vector of a lattice point at l_1, l_2 and l_3, (which are integers), from the origin,

$$\frac{\partial E}{\partial a_i} = -\frac{n}{4}\,a_i \sum_{l_1 l_2 l_3} l_i^2\,\frac{D\alpha}{r}$$

$$[\exp\{-2\alpha\,(r-r_0)\} - \exp\{-\alpha\,(r-r_0)\}] \quad ...(7)$$

$$\frac{\partial^2 E}{\partial a_i\,\partial a_j} = \frac{n}{8}\,a_i\,a_j \sum_{l_1 l_2 l_3} l_i^2\,l_j^2\,\frac{D\alpha}{r^2}\left[\left(\alpha+\frac{1}{2r}\right)\right.$$

$$\exp\{-2\alpha\,(r-r_0)\} - \left(\frac{\alpha}{2}+\frac{1}{2r}\right)$$

$$\left.\exp\{-\alpha\,(r-r_0)\}\right] + \delta_{ij}\,\frac{n}{4}\sum_{l_1 l_2 l_3} l_i\,l_j\left(-\frac{D\alpha}{r}\right)$$

$$[\exp\{-2\alpha\,(r-r_0)\} - \exp\{-\alpha\,(r-r_0)\}] \quad ...(8)$$

The potential parameters[2] used for fcc aluminium were

$\alpha = 0{\cdot}6163$ au^{-1}

$r_0 = 6{\cdot}1470$ au

$D = 0{\cdot}0199$ rydberg

where the equilibrium value of the lattice parameter is $a^0=7{\cdot}6160$ au.

The fcc lattice sums were evaluated including sufficient number of neighbour shells. We imposed a limit

$$(l_1^2 + l_2^2 + l_3^2) \leqslant 50$$

Results and discussion—From the unstrained equilibrium value a_0 where the internal potential energy is minimum, the lattice parameter a_1 was given regular increments by 0·05 au and at each stage F_i and F_{ij} were calculated. Changes of a_2 and a_3 were regulated to make F_2 and F_3 equal to zero all through. The first violation takes place at $a_1 = 8{\cdot}1260$ au where the stability condition $F_{22}-F_{23}>0$ is broken. The corresponding stress is $0{\cdot}2375\times10^{-3}$ rydberg/au^3 or $34{\cdot}87\times10^9$ dyne/cm^2. The strain at that point is 0·0669 or about 6·7%. So these are the tensile strength and corresponding strain for $\langle 100 \rangle$ uniaxial tension.

On compression, the lattice becomes unstable at $a_1=7{\cdot}0660$ au where $\{F_{11}(F_{22}+F_{23})-2F_{12}^2\}$ becomes negative. The stress then is $-0{\cdot}9758\times10^{-4}$ rydberg/au^3 or $-14{\cdot}33\times10^9$ dyne/cm^2 and the strain is $-0{\cdot}0722$ or about $-7{\cdot}2\%$.

Hence the fcc aluminium lattice has a region of stability bounded by $a_1=8{\cdot}1260$ au to $a_1=7{\cdot}0660$ au.

Results of numerical calculations are shown in Figs. 1-3.

The experimentally measured[6] tensile strength of high purity aluminium in the form of wire of diameter 0·15 mm is $0{\cdot}024\times10^6$ psi or $16{\cdot}55\times10^8$ dyne/cm^2. So our calculated values are an order of magnitude

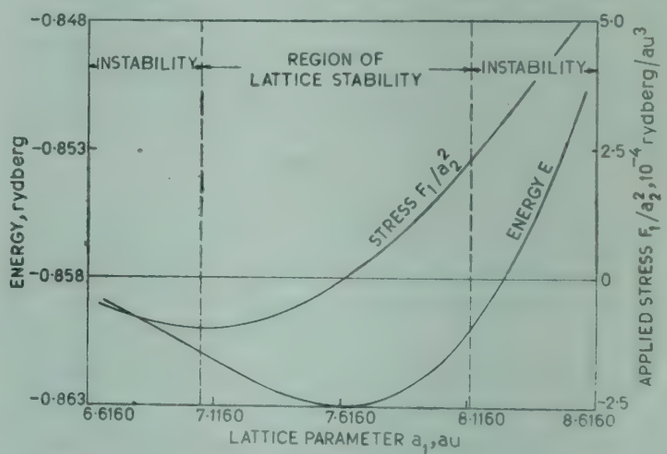

Fig. 1—Energy and applied stress as functions of a_1

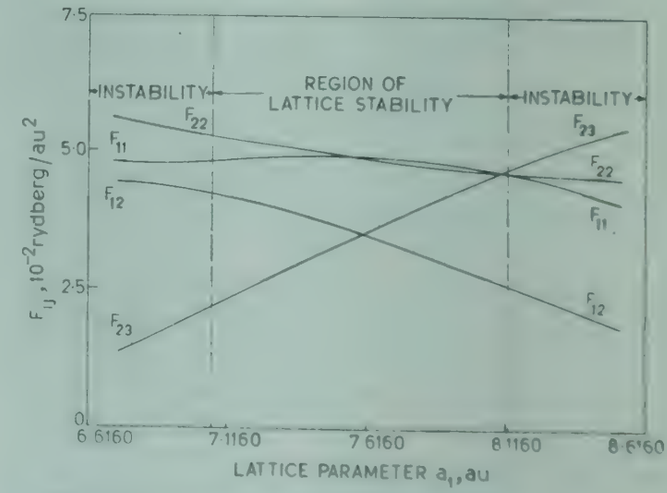

Fig. 2—Independent moduli F_{ij} as a function of a_1

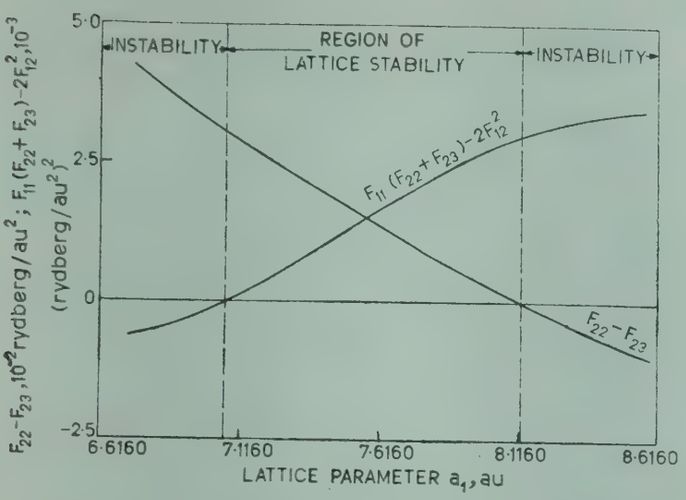

Fig. 3—$F_{22}-F_{23}$ and $F_{11}(F_{22}+F_{23})-2F_{12}^2$ as functions of a_1

higher. But this disparity may be attributed to the presence of dislocations and other imperfections in the drawn metallic wire which is not microscopically thin.

The morse potential function used in our calculations does, in no way, represent the actual state of affairs regarding the interaction of metallic atoms in the lattice. A more rigorous interatomic potential function is sure to yield better results. We already tried[7,8] a pseudopotential model and presently working with other models.

References

1. Kelly A, *Strong solids* (Clarendon Press, Oxford), 1973.
2. Born M & Furth R, *Proc. Camb. Phil. Soc.*, **36** (1940), 454.
3. Girifalco L A & Weizer V G, *Phys. Rev.*, **114** (1959), 687.
4. Lincoln R C, Koliwad K M & Ghate P B, *Phys. Rev.*, **159** (1967), 463.
5. Milstein F, *Phys. Rev.*, **B3** (1971), 1130.
6. Rumbles W E, *et al.*, *Proc., SAMPE Filament Winding Conference*, 1961, pp. 122.
7. Mitra A K & Sengupta P K, *Proc. Nucl. Phys. & Solid St. Phys. symp.*, Vol. **19c** (1976), 165.
8. Mitra A K & Sengupta P K, Paper presented to the *International Symposium on Solid State Physics, Calcutta*, January, 1977 (to be published in *Indian J. Phys.*).

Isothermal Decay of CaO:Eu:Tb Phosphors

Y Raman, S Sivaraman & J D Ranade

Department of Physics, University of Saugar, Sagar 470 003

Received 28 *February* 1979; *revised received* 5 *July* 1979

The results obtained on the decay of CaO:Eu:Tb phosphors at room temperature are reported. The curves have been analyzed on the basis of Randall and Wilkins' theory and correlated with thermoluminescence data. A fair agreement has been observed between the trap depths obtained from exponential decay curves and thermoluminescence measurements.

The growth and decay of luminescence provides information regarding the energy distribution of the traps and their numbers.[1,2] Decay studies, along with thermoluminescence and photoconductivity measurements give useful information about the type of mechanism in the luminescence process. In this note, we report the phosphorescence decay of CaO:Eu:Tb phosphors and its correlation with thermoluminescence.

The phosphor preparation has been described elsewhere.[3] The decay apparatus consists of a brass block with a cavity at the centre into which the phosphor is packed. X-rays were used for excitation and the phosphors were excited for 5 min. The sample was placed at one end of a wooden box and a detector was attached to the other end. An IP21 photomultiplier tube was used as the detector, the output of which was connected to a multiflex galvanometer, type MG 2 Gerat NV1423 M, having an initial resistance of 1300Ω and a sensitivity of $4{\cdot}1 \times 10^{-9}$ A/mm. An Anu Vidyut power supply (type-720) was used to provide the necessary voltage to the photomultiplier tube.

The CaO:Eu phosphor is found to emit an intense line at 600 nm which corresponds to $^5D_0 \rightarrow {}^7F_1$ and magnetic dipole transition. There is a weak emission between 610 and 620 nm which corresponds to $^5D_0 \rightarrow {}^7F_2$ and to electric dipole transition. If europium occupies a site with inversion symmetry, then magnetic dipole transition dominates. The weak lines between 610 and 620 nm may be caused by coupling between lattice vibrations giving rise to temporary deviation from cubic symmetry. The spectra of CaO:Tb show seven lines at 420, 438, 460, 490, 555, 588 and 625 nm and correspond to transitions from $^5D_3$ to $^7F_{5,4,3}$ and $^5D_4$ to $^7F_{6,5,4,3}$ levels of Tb (Ref. 3).

The nature of the decay curves recorded was investigated by plotting log I vs time. The curves were found to be nonlinear ruling out an exponential nature of decay. However, the graphs between log I vs log t were found to be linear. Therefore, the decay may be hyperbolic in nature.

In phosphors where the decay has been observed to take place in stages, the first-stage decay is very rapid and is followed by another slow component.[1] This may be considered to be due to different trap depths and, therefore, it can be assumed that as the number of exponentials increases the decay curve changes from a straight line to a hyperbolic curve on a semi-log plot.[4] According to Bube,[5] the minimum number of exponentials required to form a hyperbolic curve is three, and it is found to be so

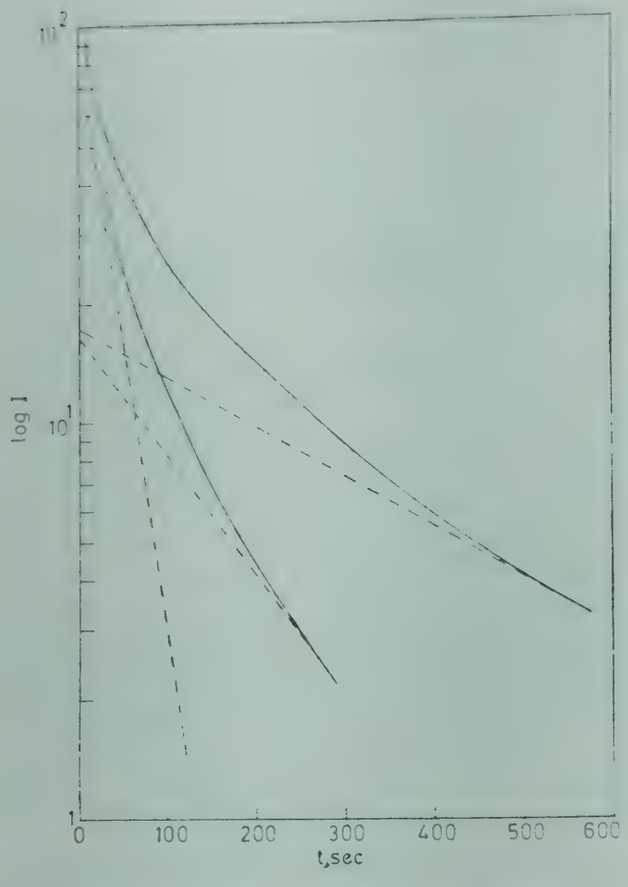

Fig. 1—Peeling-off of decay curves log I vs t for CaO:Eu (0·2 mole %)

in the present case (Fig. 1). Therefore, the hyperbolic decay of phosphors containing traps of different energies and population can be explained on the basis of a monomolecular mechanism using the superposition scheme.

The trap depths were calculated from the slopes of the semi-log plot using the formula :

$$E = kT \log S - \log\left(-\frac{\log I/I_0}{t}\right) \qquad ...(1)$$

where k is the Boltzmann's constant, T the temperature in K, S the frequency of escape factor, I_0 and I the intensities at the time $t = 0$ and at any time t. The values are presented in Table 1.

The value of the decay constant has been calculated by the method of least squares, and was found to be negative in all cases. Therefore, a power law is applicable so that

$$I = I_0 t^{-b} \qquad .. (2)$$

The values of the activation energy calculated from thermoluminescence measurements[6] were found to be slightly more than those calculated from the decay experiment. In the decay experiment, the sensitivity of the experimental set-up has to be adjusted according to the initial intensity which is usually high. The decay, therefore, is always recorded

Table 1—Trap Depths from the Peeling-off Curves and TL Measurements

Sample	b	E (in eV) from peeling off curve			E (in eV) from TL
		I	II	III	(Ist peak only)
Mole % of Eu		CaO:Eu phosphor			
1	−0.92	0·59	0·61	0·65	0·70
3×10^{-1}	−0·91	0·60	0·62	0·65	0·67
2×10^{-1}	−0·84	0·62	0·63	0·65	0·69
1×10^{-1}	−0·77	0·62	0·64	0·66	0·68
Mole % of Tb		CaO:Tb phosphor			
1	−0·93	0·62	0·63	0·64	0·69
2×10^{-1}	−0·91	0·61	0·62	0·63	0·68
$1·5\times10^{-1}$	−1·0	0·62	0·63	0·64	0·71
1×10^{-1}	−0·78	0·56	0·59	0·64	0·71
		CaO:Eu_x:Tb_y phosphor (x = 0·1 mole %)			
$y=10^{-6}$	−0·78	0·61	0·62	0·63	0·66
10^{-5}	−0·83	0·62	0·63	0·65	0·66
10^{-4}	−0·75	0.62	0·64	0·65	0·67
10^{-3}	−0·68	0·62	0·63	0·65	0·66
		CaO:Tb_y:Eu_x pnosphor (y = 0·1 mole %)			
$x=10^{-7}$	−0·56	0·62	0·63	0·64	0·70
10^{-6}	−0·36	0·61	0·62	0·64	0·69
10^{-5}	−0·74	0·61	0·62	0·63	0·72
10^{-4}	−0·62	0·61	0·62	0·63	0·68

up to a low intensity but not zero intensity. This would imply that the group of traps corresponding to the slowest exponential is not completely emptied during the experiment. The calculated trap depth should, therefore, be a little lower than if all the traps were emptied. In the thermoluminescence experiment, on the other hand, after excitation at room temperature, the emission is allowed to decay to a low value, in which time the shallow traps corresponding to the fastest and middle exponentials are almost empty. Even allowing for a redistribution of electrons to a certain extent, the first glow peak will have very little contribution from the shallow traps. Further, the traps due to the slowest exponential are completely emptied during the glow run. The average trap depth evaluated from the thermoluminescence data should, therefore, be expected to be higher than the value calculated from the lowest exponential. However, it is likely that the frequency factor may be affected by temperature to

an uncertain but small extent. Thus a fair agreement between trap depths calculated from the slowest exponential and the first glow peak (the latter being marginally higher) is to be expected. Such an agreement has been found in the present system when the trap depths from the glow peaks are calculated using the formula given by Curie on the basis of Randall and Wilkins' theory.

CaO has a large band gap (7·7 eV) which inhibits conduction and the electrons and holes cannot move freely. Further, it has been reported[7] that the greater electronegativity of the lighter members of the alkaline earth oxide series insures the trapping of the electron near the site of excitation whereas the electron is comparatively free to move in the case of SrO and BaO. These considerations further justify the analysis of the observed decay in terms of a superposition of exponentials. An estimate of μ was made[8] where the overlap of the glow curves was small and it came out to be around 0·42 indicating that the recombination kinetics are of the first order.

One of the authors (YR) gratefully acknowledges the financial assistance given by the University Grants Commission, New Delhi.

References

1. Randall J T & Wilkins, M H F, *Proc. R. Soc.*, A184 (1945), 366.
2. Urbach F, Nail N R & Pearlman D, *J. opt. Soc. Am.*, 39 (1949), 675.
3. Raman Y, Sivaraman S & Ranade J D, *Phys. Status Solidi*, 51 (1979), 683.
4. Gergely G, *J. opt. Soc. Am.*, 40 (1956), 356.
5. Bube R H, *Phys. Rev.*, 80 (1950), 655.
6. Raman Y, Sivaraman S & Ranade J D, unpublished work.
7. Hecht H G & Taylor E D, *J. Phys. Chem. Solids*, 28 (1967), 1599.
8. Halperin A, & Braner A A, *Phys. Rev.*, 117 (1960), 408.

Moelwyn-Hughes Parameter of Pure Liquids & Liquid Metal Alloys

K P Thakur
School of Molecular Sciences, University of Warwick
Coventry C V 4 7AL, England
&
Lakshmi Kant Jha*
Department of Chemistry, K K M College
Jamui (Monghyr) 811 307

Received 8 *December* 1978; *revised received* 20 *February* 1979

Moelwyn-Hughes Parameter (C_1) has been calculated for some pure liquids and liquid sodium-potassium alloys, using ultrasonic data. Value of C_1 is found to decrease with increasing temperature for organic liquids and increase for liquid alloys. The results obtained are discussed in terms of the liquid state model.

*To whom correspondence should be addressed

Recently, a new characteristic parameter termed as Moelwyn-Hughes (MH) parmeter has become the subject of extensive study.[1-7] Following Moelwyn-Hughes,[8] it is possible to compute the sum of the exponent $(m + n)$ of generalized Lennard-Jones potential, which has been applied to a variety of physico-chemical systems, by the relation

$$m + n = 3\,(C_1 - 2) \qquad \ldots(1)$$

where C_1 in the MH parameter.

The complete potential function for the molecular interaction is given by the equation

$$U(r) = ar^{-n} - br^{-m} \qquad \ldots(2)$$

where a and b are constants and n must be greater than m for this term to dominate at small intermolecular separations and m has the integral values 1, 2, 3, 4, 6, or 8.

Eq. (2) can be modified to incorporate the thermodynamic properties of liquids so that the final relation becomes

$$\frac{\alpha V}{\beta C_V} = -\frac{d \ln \nu}{d \ln V} = \frac{m + n + 1}{6} \qquad \ldots(3)$$

But for liquids, the pseudo-Grüneisen parameter[9] Γ is defined as

$$\Gamma = \frac{C^2 \alpha}{C_p}$$

where C is the velocity of sound. Using the relations

$$C^2 = \frac{1}{\beta_s \rho} \; ; \; \frac{C_p}{C_V} = \frac{\beta_T}{\beta_s}$$

we get

$$\Gamma = \frac{\alpha V}{\beta_T C_V} \cdot \frac{\gamma - 1}{T\alpha} \qquad \ldots(4)$$

where β_s, β_T, γ, T and V are respectively the adiabatic compressibility, isothermal compressibility, specific heat ratio, absolute temperature and molar volume.

Using Eqs. (3) and (4), one obtains

$$m + n = 6\Gamma - 1 \qquad \ldots(5)$$

From Eqs. (1) and (5), we get

$$3\,(C_1 - 2) = 6\,\Gamma - 1 \qquad \ldots(6)$$

Substituting the value of $\Gamma = (\gamma - 1)/T\alpha$ from Eq. (4) in Eq. (6), we have

$$C_1 = \frac{6\,(\gamma - 1)/T\alpha + 5}{3} \qquad \ldots(7)$$

Eqs. (7) and (1) have been utilized for the calculation of MH parameter and sum of exponent $(m+n)$ of generalized LJ potential of pure liquids and liquid metal alloys. This parameter and sum of exponent

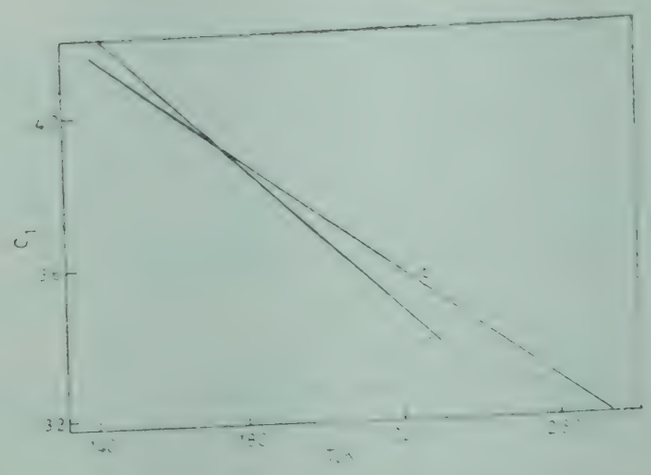

Fig. 1—Variation of MH parameter (C_1) with temperature for (a) Liquid propane and (b) Liquid *n*-Butane

Table 1—Sum of Exponent ($m+n$) of Lenard-Jones Potential for Liquid Propane and *n*-Butane

Temp., °C	$m+n$	Temp., °C	$m+n$
Propane		*n*-Butane	
228	4·15	268	3·63
223	4·35	263	3·75
213	4·63	253	4·04
203	4·92	243	4·26
193	5·22	233	4·51
183	5·50	223	4·75
173	5·80	213	4·98
163	6·07	203	5·17
153	6·31	193	5·34
143	6·56	183	5·62
		173	5·89
		158	6·11
		153	6·20
		148	6·30
		143	6·41

Table 2—Moelwyn-Hughes Parameter (C_1) and Sum of Exponent ($m+n$) of LJ Potential for Some Organic Liquids

Temp., °C	C_1	$m+n$	Temp., °C	C_1	$m+n$
Benzene			Cyclohexane		
10	4·41	7·24	20	3·49	4·48
40	3·82	5·46	30	3·43	4·30
Chloroform			Toluene		
0	4·53	7·59	0	4·23	6·69
20	4·23	6·70	50	3·51	4·52
30	4·12	6·35			
Bromobenzene			Octane		
0	4·80	8·40	10	3·09	3·27
50	3·78	5·34	30	2·92	2·77
Carbon tetrachloride			Nonane		
0	4·54	7·62	10	3·92	5·77
20	4·20	6·60	30	3·16	3·49
30	4·06	6·18			
			Decalin		
			15	3·88	5·64
Ethyl bromide			Decene		
20	4·20	6·61	10	3·40	4·20
			30	3·22	3·66
Ethyl iodide			Decane		
0	4·34	7·03	20	3·19	3·57
			30	3·13	3 38
Carbon disulphide			Undecane		
0	4·16	6·48	10	3 32	3·97
20	4·84	8·53	30	3·16	3·48
30	4·68	8·05			
40	4·52	7·56			
Tridecane			Cetane		
10	3·43	4·30	30	3·02	3·06
30	3·13	3·40			

($m+n$) of LJ potential are very useful in investigating the microscopic behaviour of solids as well as polar and non-polar liquids.[7,8]

Results and discussion—Due to experimental difficulties, very little work has been done on the measurement of ultrasonic velocity in liquefied gases. Using the pulse technique, the velocities of ultrasonic waves in liquefied propane and *n*-butane were measured within ± 1% by Rao.[10] The values of MH parameter for these liquids have been calculated at different temperatures using Eq. (7) and have been plotted against temperature for propane and *n*-butane in Fig. 1; the $m+n$ values of these liquids are presented in Table 1. In both cases we get straight line curves. Fig. 1 shows that the intercept of C_1 against T plot at $T=0$K decreases and the negative value of slope also decreases with the addition of a $-CH_2$ group in the higher alkane series.

The values of MH parameter for a number of organic liquids have been calculated from the available data on acoustic and thermodynamic properties and the results are presented in Table 2. In the case of organic liquids, the necessary data for the calculation of C_1 were taken from Nomoto's paper.[11] We have also presented in Table 3, the calculated values of C_1 at 30°C for some inorganic liquid

Table 3—Moelwyn-Hughes Parameter (C_1) and Sum of Exponent ($m+n$) of Lenard-Jones Potential for Some Inorganic Liquid Halides (Temperature=30°C)

Liquid	C_1	$m+n$
$SiCl_4$	3·68	5·05
$TiCl_4$	4·13	6·39
$CeCl_4$	3·84	5·53
$SnCl_4$	4·02	6·06
PCl_3	4·13	6·38
PBr_3	4·97	8·90
$AsCl_3$	4·52	7·56

Table 4—Moelwyn-Hughes Parameter (C_1) and Sum of Exponent ($m+n$) of Lenard-Jones Potential for Liquid Sodium-Potassium Alloys

Liquid Alloy	Temp.,°C	C_1	$m+n$
Pure Na	104	3·86	5·59
	118	3·82	5·61
	130	3·89	5·68
	147	3·90	5·71
	154	3·91	5·73
74% Na-26% K	30	3·96	5·89
67% Na-33% K	25	3·99	5·98
57% Na-43% K	20	3·97	5·91
	72	3·97	5·92
	130	3·98	5·95
49% Na-51% K	20	2·99	5·97
32% Na-68% K	20	4·01	6·10
	65	4·07	6·21
	100	4·08	6·25
Pure K	74	4·20	6·60
	108	4·20	6·60
	116	4·20	6·61
	150	4·19	6·60

halides, using Weissler's ultrasonic data.[12] It is interesting to note that C_1 decreases with increase in the temperature for all the organic liquids.

Some properties of liquid metals[13–15] (Hg, Na, K, Rb, etc.) have been studied in order to investigate their internal structures and quasi-crystalline properties. Litovitz *et al.*[16] conducted the acoustic investigations of liquid sodium-potassium alloys and measured accurately the velocity and absorption of ultrasonic waves in these alloys from 20 to 154°C. The values of C_1 have been computed according to Eq. (7) from these data,[13–16] and are listed in Table 4.

Table 5—Moelwyn-Hughes Parameter (C_1) and Sum of Exponent ($m+n$) of Lenard-Jones Potential for Some Liquids and Liquid Metals

Liquid	Temp.,°C	C_1	$m+n$
Neon	25-37	6·5	13·4
Krypton	150-200	5·8	11·6
	(Pressure range 25 to 600 atm.)		
Propane	143-228	3·77	5·3
n-butane	143-268	2·77	5·1
Copper	1356 (m.p.)	58·67	160·0
Silver	1234 (m.p.)	7·83	17·5
Zinc	693 (m.p.)	5·93	11·8
Cadmium	594 (m.p)	6·80	14·4
Mercury	234 (m.p.)	7·27	15·8
Aluminium	933	6·33	13·0
Gallium	303	6·87	14·6
Indium	429	6·50	13·5
Tin	505	6·93	14·8
Lead	601	6·70	14·1
Bismuth	544	6·03	12·1

The value of C_1 is found to increase with increasing temperature. The behaviour of these liquid Na-K alloys is similar to those of solids for which the MH parameter is independent of temperature; with the percentage increase of potassium in the alloy the value of C_1 increases interestingly.

The values of MH parameter for some liquids and liquid metals, calculated from Eq. (7), are given in Table 5. The values of input data used for the liquid metals mentioned were collected from different sources.[17] The values of $(m+n)$ computed according to Eq. (1) are also listed for all the liquids under study in Tables 1 to 5. The computed values of $(m+n)$ vary from a minimum value of 2·77 for octane at 30°C to a maximum value of 160 for copper at 1356 K. The cause for the misleading values of $(m+n)$ and hence C_1 for other liquids may be due to the inadequacy of Eq. (2), based upon the harmonic oscillator model, or the inaccuracy of the input experimental data.

As a result of the present study, it is felt that the wide range of the values of m and n may be due to the approximations made in the calculations. Quantitative comparison of the theoretical values of the physical parameter with the experimental results can be made only after having full analysis of the implications of the various approximations made.

References
1. Rao R V G, Keer H V, *Z. phys. Chem.*, 219 (1962), 231.
2. Rao R V G, Keer H V & Das C D, *Z. phys. Chem.*, 220 (1962), 71.
3. Rao R V G, Keer H V & Das C D, *Indian J. Chem.*, 2 (1964), 27.
4. Rao R V G, Das C D & Keer H V, *Indian J. Phys.*, 37 (1963), 238.
5. Keer H V, *Z. Phys. Chem.*, 251 (1972), 22.
6. Thakur K P & Pandey J D, *Indian J. pure appl. Phys.*, 12 (1974), 779.
7. Thakur K P, *Acta crystallogr.*, 32A (1976), 363.
8. Moelwyn-Hughes E A, *Physical chemistry*, 2nd revised. (Pergamon Press, London), p. 330.
9. Grüneisen E, *Handb. Phys.*, (Springer-Verlag, Berlin), 10 (1926), 21.
10. Seshagiri Rao M G, *Indian J. pure appl. Phys.*, 2 (1971), 169.
11. Nomoto O, *J. phys. Soc. Japan*, 18 (1963), 1536.
12. Weissler A, *J. Am. chem. Soc.*, 71 (1949), 1272.
13. Knopoff L & Shapiro J N, *Phys. Rev.*, 1B (1970), 3893.
14. Kor S K, Tondon V S & Singh B K, *Physics Lett.*, 38A (1972), 187.
15. Tondon U S & Pandey S K, *Physics Lett.*, 41A (1972), 161.
16. Litovitz T A & Jarzynski J, *J. chem. Phys.*, 41 (1964), 1920.
17. Jain R P & Pandey J D, *Indian J. pure appl. Phys.*, 12 (1974), 830.

EPR & Optical Absorption Studies on the Coordination Compounds of Copper (II) with (3,5-Dimethyl Isoxazole) & (3-Methyl, 5-Phenyl Isoxazole) Ligands

G Ponticelli & G Pelizzi

Instituto Chimico Policattedra, University of Cagliari, 09100 Cagliari, Italy

and

B A Sastry, S Md Asadulla & E S Chary

Department of Physics, Osmania University Hyderabad 500 007

Received 22 *September* 1978; *revised received* 22 *November* 1978

EPR and optical absorption studies are carried out on Cu (3,5-dimethyl isoxazole)$_4$ $(ClO_4)_2$ and Cu (3-methyl, 5-phenyl isoxazole)$_4$ $(ClO_4)_2$ in N,N′-dimethylformamide (DMF) solvent. From the magnitude of the spin-Hamiltonian parameters, it is found that the coordinating atom is oxygen of isoxazole ligand but not nitrogen as observed in solids of these complexes by IR and other spectroscopic techniques. Using these spin-Hamiltonian constants and optical absorption parameters, the metal-ligand bond parameters are calculated and are found to possess weak σ- and π-bonds. The 4*s* contribution to the ground state is found to be nil.

It is well known that isoxazole derivatives possess very interesting pharmacological properties and these are very important from biological point of view. The isoxazole ligand has two potential donor atoms namely oxygen and nitrogen. In most metal complexes of isoxazole and its derivatives it is shown that this ligand behaves as bridging ligand O-bonded and N-bonded.[1–5] But in few complexes like Cu[3,5-dimethyl isoxazole]$_4$ $(ClO_4)_2$ and Cu[3-methyl, 5-phenyl isoxazole]$_4$ $(ClO_4)_2$, it is found from IR absorption in solids that only nitrogens are bonded with the metal ion in a square planar fashion.[2,4] It is also known that 3,5-dimethyl isoxazole shows marked action as a diuretic, analgesic and produces hypoglycemia.[6,7] Since the pharmacological and biological properties and medical importance of metal complexes depend on the atoms coordinating the metal ion the authors have taken up the detailed EPR and optical absorption study of the above two metal complexes, dissolved in N,N′-dimethyl-formamide (DMF) to decide the coordinating atoms and the metal-ligand bond nature. The structural formule for the above two ligands are shown in Fig. 1.

The complexes under investigation are prepared by the methods described earlier.[2,4] A Varian E-4 *X*-band ESR spectrometer with E-231 cavity is employed to record the first derivative signals of the EPR absorption in 0·005*M* solutions of these complexes both at room and liquid nitrogen temperatures. A varian field dial regulator is used to accurately calibrate the magnetic field. The magnetic field homogeneity is about ± 30 mgauss over the effective sample volume. DPPH is used as a *g*-marker. The error in *g* and hyperfine separation values are about ± 0·001 and ± 0·5 gauss respectively. A Unicam SP 700 spectrophotometer is used to record the optical absorption spectrum.

The EPR spectra of both the complexes in DMF resulted in single lines at room temperature. The EPR spectrum at 77 K of Cu (3,5-dimethyl isoxazole)$_4$ $(ClO_4)_2$ is shown in Fig. 2. The principal *g* and *A* values are obtained from the computer (JEC-6) simulated spectra for a Lorentzian line shape[8] and are given in Table 1. Except in a few cases,[9–11] the hyperfine lines on the high field size of frozen solution and powder spectra of copper complexes will not be resolved completely. In most of

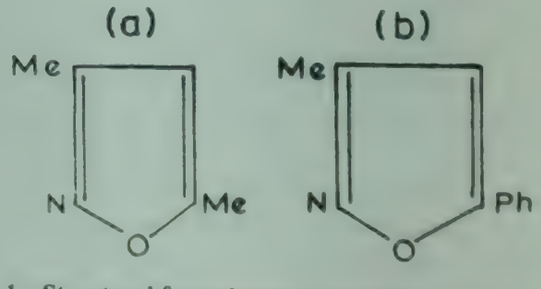

Fig. 1—Structural formulae for the compounds (a) 3, 5-dimethyl isoxazole and (b) 3-methyl, 5 phenyl isoxazole

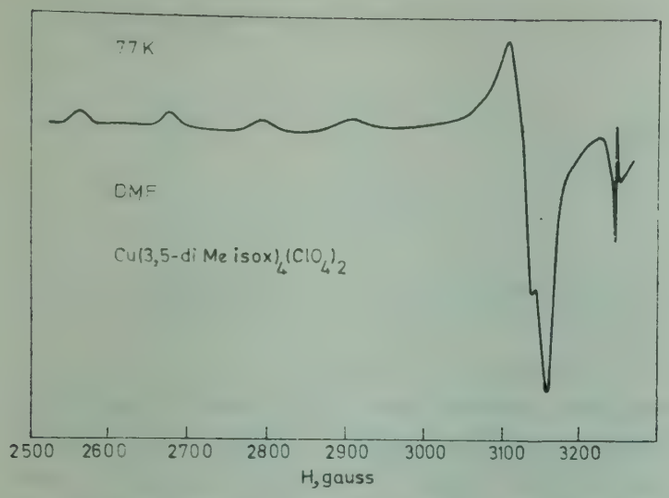

Fig. 2—EPR spectrum of Cu [3, 5-dimethyl isoxazole]$_4$ $(ClO_4)_2$ in DMF at 77 K

Table 1—Spin-Hamiltonian Constants and Optical Data

Parameter	Substance	
	Cu [3-methyl, 5 phenyl isoxazole]$_4$ $(ClO_4)_2$	Cu [3, 5- dimethyl isoxazole]$_4$ $(ClO_4)_2$
g_e	2·194	2·196
$g_{\|\|}$	2·404	2·407
$g_\perp$	2·09	2·091
$A_{\|\|}$, MHz	405·6	409·5
$A_\perp$, MHz	20·6	14·7
ΔE, cm^{-1}	12400	12200

the cases, the high field side of the spectrum will be a single line due to overlap of hyperfine lines. But in the present case, the kink on the high field side most probably results due to a partial splitting of these lines. From the above computer simulations it is evident that this kink on the high field line does not correspond to the rhombic electric field around copper (II). From these g and A values, it is evident that the bonding atom is oxygen but not nitrogen. This is because it is found, from the literature, that CuO_4 and CuO_6 chromophores have $g_{\|\|}$ values lying between 2·35 and 2·52 and $A_{\|\|}$ values in between 140 and 90gauss when the ground state is $d_{x^2-y^2}$, (Ref. 12-14), whereas in the case of CuN_4 chromophore, the corresponding values lie between 2·150 and 2·22 and 220 and 160 gauss. From the g and A values (Table 1) of these complexes it is evident that the unpaired electron is in $d_{x^2-y^2}$ orbital. Using the expressions of the molecular orbital theory of Maki and McGarvey,[18] the values of σ- and in- and out-of-plane π-bond parameters, α^2, β_1^2 and β^2 respectively are calculated and are found to be the same for these complexes; α^2, β_1^2 and β^2 come out to be 0·86, 0·90 and 0·82 respectively indicating less covalent nature of the metal-ligands bonds. Since axial ligands mix the 4s character into the ground state we have also calculated the fraction of 3d-character (f^2) in copper 3d-4s ground state using the expressions (15′) and (16′) of Kuska *et al.*[19] The value of f^2 from these calculations comes out to be unity for both the complexes indicating that the complexes in DMF solutions are planar.

From the EPR and optical absorption studies of the complexes under investigation in DMF solution it can be seen that the N-coordinated original ligands of the complex in solid have changed to O-coordinated DMF ligands indicating the presence of copper-oxygen bond of DMF. Both the complexes in the present investigation may have square planar arrangement around copper (II). The Cu—O bond of DMF in solution for both the complexes in less covalent.

We are grateful to Dr H Kozltowski, Institute of Chemistry, University of Wroclow, Poland, for his help in computer simulations. We are also thankful to Prof. K V Krishna Rao, Head of the Department, Osmania University, Hyderabad, for his constant encouragement throughout the work. We express our gratefulness to Prof. T Navaneeta Rao, Head of the Department of Chemistry, Osmania University, for the facilities given to take the optical spectra.

References

1. Devoto G, Ponticelli G & Preti C, *J. inorg. nucl. Chem.*, **37** (1975), 1635.
2. Massacesi M & Ponticelli G, *J. inorg. nucl. Chem.*, **37** (1975), 1641.
3. Cristini A & Ponticelli G, *J. inorg. nucl. Chem.*, **36** (1974), 2473.
4. Devoto G, Massacesi M, Ponticelli G & Preti C, *J. inorg. nucl. Chem.*, **39** (1977), 271.
5. Karayannis N M, Mikulski C M, Sonsino S D, Bradshaw E E & Pytlewski L L, *Inorg. chim. Acta*, **14** (1975), 195.
6. Vetulani J, *Disc Pharm. Pharmacol.*, **18** (1966), 13, 19.
7. Gordonoff T, *Med. Exptl.*, 7 (1962), 201.
8. The computer Programme we applied was based on W C Tennat—*Computer simulations of ESR powder spectra*, Report No. C D 2153/1972, Chemistry Division, Department of Scientific and Industrial Research, Lower Nutt, New Zealand.
9. Yokoi H, Sai M & Isode T, *Bull. chem. Soc. Japan*, **43** (1970), 1078.
10. Pradilla-Sorzano J & Fakler J P, *Inorg. Chem.*, **13** (1974), 38.
11. Barbucci R & Campbell M J M, *Inorg. chim. Acta*, **15** (1975), L15.
12. Hitchman M A & Waite T D, *Inorg. Chem.*, **15** (1976), 2150, 2155.

13. Joesten M D, Koch R C, Martin T W & Venable J R, *J. Am. chem. Soc.*, **93** (1971), 1138.
14. Dawson K, Hitchman M A, Prout C K & Rossotti F J C, *J. chem. Soc.*, **A5** (1972), 1509.
15. Wasson J R & Zacharopoulos P, *J. inorg. nucl. Chem.*, **31** (1969), 3881.
16. Hsu Y, *Molec. Phys.*, **21** (1971), 1087.
17. Assour J M, *J. chem. Phys.*, **43** (1965), 2477.
18. Maki A H & McGarvey B R, *J. chem. Phys.*, **31** (1958), 29, 35.
19. Kuska H A, Rogers M T & Drullenger R E, *J. phys. Chem.*, **71** (1967), 109.

Relativistic Electronic State of a One-Dimensional System

C L Roy, A Singh* & G Roy**
Department of Physics, Indian Institute of Technology
Kharagpur

Received 19 *March* 1979

A quantitative investigation of the band structure of electronic energy spectrum, for a one-dimensional monoatomic crystal with rectangular well potential has been carried out. Two approaches are followed for the purpose, one due to M L Glasser and S G Davison [*Int. J. quant. chem.*, IIIS (1970), 867] (GD) and the other due to M Steslicka and S G Davison [*Phys. Rev.*, **B1** (1970), 1858.] (SG). The results yielded by the two procedures are critically compared and thereby the circumstances under which the relatively simpler approach due to SG would afford quite satisfactorily, the relativistic corrections to bulk state energies, are indicated.

The theoretical investigation of relativistic bulk states[1-3] and relativistic surface states[4,5] for one-dimensional systems, has become an important aspect of solid state physics during the last decade. The starting point for such investigations is the following time-independent Dirac equation :

$$i\hbar\,\sigma_x \frac{d\Phi}{dx} - mc^2\,\sigma_t\,\Phi = [E - V(x)]\,\Phi \qquad \ldots(1)$$

where $\sigma_x = \begin{bmatrix} 0 & 1 \\ 1 & 0 \end{bmatrix}$, $\sigma_z = \begin{bmatrix} 1 & 0 \\ 0 & -1 \end{bmatrix}$

Φ = a two-component spinor $\begin{pmatrix} \Phi_1 \\ \Phi_2 \end{pmatrix}$

m = rest mass of the electron.

The form of the potential $V(x)$ is finally taken as a δ-function, which is realizable as a limiting case of either a rectangular barrier potential or a rectangular well potential. For the rectangular well or barrier type potential, Eq. (1) can be solved to obtain Φ as[6] in Eq. (2).

$$\Phi = \begin{pmatrix} -\gamma \\ 1 \end{pmatrix} \alpha \exp(i\rho_v x) + \begin{pmatrix} \gamma \\ 1 \end{pmatrix} \beta \exp(i\rho_v x) \qquad \ldots(2)$$

where, $\rho_v^2 = \dfrac{(\epsilon - V)[(\epsilon - V) + 2mc^2]}{\hbar^2 c^2}$

$$\epsilon = (E - mc^2),\ \gamma = \frac{\epsilon}{\hbar c \rho_v} \frac{V}{}$$

V is the constant potential over the regions occupied by the barriers or the wells in the lattice.

The application of Eq. (1) to the study of both bulk and surface states requires Φ to satisfy some boundary conditions in all situations, other than the case of bulk states of Kronig-Penney (KP) model with δ-function potentials.[1] Glasser and Davison (GD) proposed[7] the boundary condition that the spinor Φ as a whole can be supposed to remain continuous at points of potential discontinuity. Subsequently, Steslicka and Davison (SG) proposed[6] another procedure which makes the assumption that the smaller component Φ_1 of Φ can be neglected compared with the larger component Φ_2; as boundary conditions, they choose the criteria that Φ_2 and $d\Phi_2/dx$ are continuous at all points. Compared with the treatment of GD, that of SG is rather approximate; of the two procedures, the one due to SG is, however, mathematically less intricate and is formally akin to the corresponding nonrelativistic (NR) treatment.

A considerable fraction of the works published in the domain of relativistic bulk and surface states in one-dimensional systems, was concerned with numerical computations relevant to various aspects of such states.[2-4] The potential chosen in these works was a δ-function and the procedure followed was that due to GD. The major objective behind these works was to explore how the results of relativistic approach due to GD compare with the corresponding non-relativistic ones. No work seems to have yet been done about how the approximate relativistic treatment of SG compares quantitatively with the rigorous treatment of GD. We feel that there is need for this kind of comparative studies as they can indicate the circumstances under which, one can obtain reasonably satisfactory relativistic corrections to bulk and surface states with the help of the relatively simpler approach due to SD.

With the motivation mentioned above, we report in this paper a computational investigation of the band structures, on the basis of the approaches due to both SD and GD. We choose for the purpose a one-dimensional model with rectangular well potential as shown in Fig. 1. As has been discussed by Allen,[8] the rectangular well (or barrier) describes

* Permanent address : Cooperative College, Jamshedpur
** Permanent address : Department of Physics, Midnapur College, Midnapur

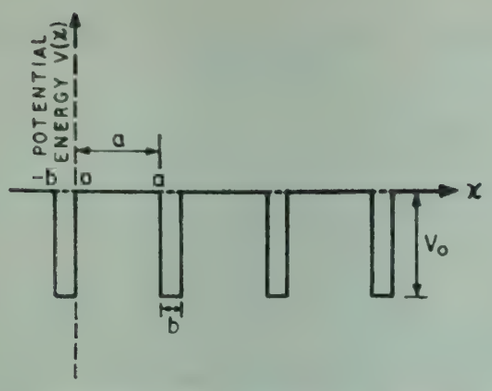

Fig. 1—A one-dimensional monoatomic crystal with rectangular atomic potentials. The energy $V(x)$ equals $-V_0$ ($V_0 > 0$) over b regions and zero over a regions

more realistically the potential in a one-dimensional system than the δ-function; this is the reason why we choose rectangular well potential in our investigation rather than the δ-function potential, which has been used by previous workers. The results of the two treatments are compared critically. This comparison affords us the conditions under which the use of relatively simpler SD approach would be justified for the purpose of computing relativistic corrections to band structures in one-dimensional systems.

To begin with the type of investigations mentioned above, we need the relevant equations for electronic energies. The equation for electronic energies on the basis of GD boundary conditions, derivable easily via an appropriate scattering matrix,[7] [Eq. (46)] reads as:

$$\cos \mu (a+b) = \cos \rho_I b \cos \rho_{II} a - \zeta \sin \rho_I b \sin \rho_{II} b \quad ...(3)$$

where

$$\rho_I = \frac{(\epsilon + V_0)\,[(\epsilon + V_0) + 2 m c^2]}{\hbar^2 c^2}$$

$$\rho_{II} = \frac{\epsilon\,[\epsilon + 2 m c^2]}{\hbar^2 c^2}$$

$$\zeta = \frac{1}{2}\left[\frac{\rho_{II}}{\rho_I}\frac{(\epsilon+V)}{\epsilon} + \frac{\rho_I}{\rho_{II}}\frac{\epsilon}{\epsilon+V_0}\right]$$

μ = Wave vector

$V = -V_0$, $V_0 > 0$, over regions of width b

$V = 0$, over regions of width a.

The treatment with SD approach depends on using a wavefunction of the form :

$$\psi = \Phi_2 = \alpha \exp(i \rho_v x) + \beta \exp(-i \rho_v x) \quad ...(4)$$

Formally, the treatment depending on Eq. (4) and on the relevant boundary conditions discussed earlier, reduces to what is followed for dealing with the same model non-relativistically[9] and leads to the following equation [Eq. (18) of Ref. 6] for electronic energies:

$$\cos \mu (a+b) = \cos \rho_{II} a \cos \rho_I b - \sigma \sin \rho_{II} a \sin \rho_I b \quad ...(5)$$

where

$$\sigma = \frac{1}{2}\left[\frac{\rho_{II}}{\rho_I} + \frac{\rho_I}{\rho_{II}}\right]$$

The computations we have carried out are based on Eqs. (3) and (5). On the basis of these equations, we have evaluated the widths of the allowed and forbidden bands; the results are shown in Figs. 2 and 3. We took $a = 1{\cdot}8$ Π Å and $b = 0{\cdot}2$ Π Å; these values are close to the ones used by Allen[8] earlier for a non-relativistic case. For V_0, we took three values, namely 1400 eV, 1500 eV and 1600 eV. These values of V_0 are large enough to warrant a display of relativistic effects.

Figs. 2 and 3 show that the variations of band widths, and band gaps with band numbers, are qualitatively the same for both kinds of boundary conditions. Quantitatively, the widths of the allowed bands for SD boundary conditions are generally smaller than those for GD boundary conditions; with respect to band gaps, the situation is just the opposite. Further, the difference between the results of the two treatments increases with V_0. It is seen that, for $V > (-1400)$ eV, the two kinds of boundary conditions would give identical results.

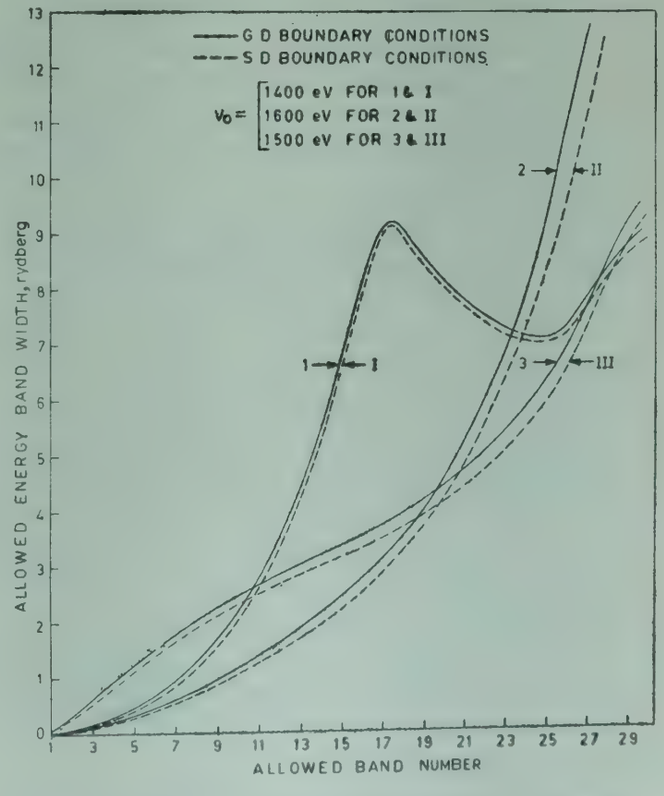
G D BOUNDARY CONDITIONS
S D BOUNDARY CONDITIONS
V_0 = 1400 eV FOR I & I
1600 eV FOR 2 & II
1500 eV FOR 3 & III
ALLOWED ENERGY BAND WIDTH, rydberg
ALLOWED BAND NUMBER
0 1 2 3 4 5 6 7 8 9 10 11 12 13
1 3 5 7 9 11 13 15 17 19 21 23 25 27 29

Fig. 2—Variation of allowed band energy with band numbers

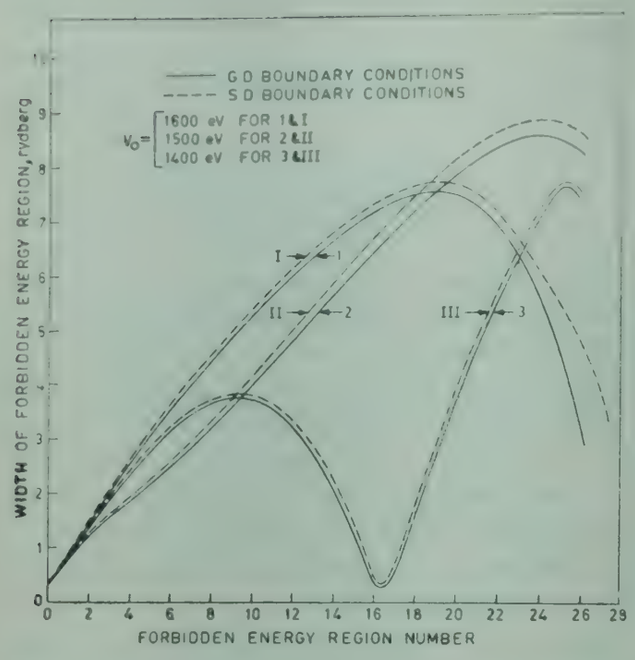

Fig. 3—Variation of width of forbidden energy regions with serial numbers of such regions

The graphs also show that the quantitative difference between the two sets of results, is larger for higher bands; the results given by the two kinds of boundary conditions are almost the same quantitatively, up to a few lower bands, e.g. 6th or 7th band. To summarize, we can say that, for one-dimensional Krong Penney crystal with rectangular well potential, the relativistic corrections to band structures can be obtained fairly accurately with the help of simple SD approach, as long as we confine our attention to well depth smaller than 1400 eV (i. e. $V > -1400$ eV) and up to 6th or 7th band.

The authors are grateful to Profs G B Mitra and H N Bose for their interest and encouragement.

References

1. Sen Gupta N D, *Phys. Status Solidi*, 65 (1974), 351.
2. Steslicka M *et al.*, *J. Phys. Chem. Solids*, 32 (1971), 1917.
3. Subramanian R & Bhagwat K V, *Phys. Status Solidi*, 48 (1971), 399.
4. Davison S G and Steslicka M, *J. Phys.: C*, 2 (1969), 1802.
5. Fairbairn W M *et al.*, *Surface Sci.*, 36 (1973), 462.
6. Steslicka M & Davison S G, *Phys. Rev.*, B1 (1970), 1858.
7. Glasser M L & Davison S G, *Int. J. quantum Chem.*, IIIS (1970), 786.
8. Allen G, *Phys. Rev.*, 53 (1953), 531.
9. Dekker A J, *Solid state physics* (Macmillan, New York), 1962, 243.

Microwave Absorbing Material Using Rubber & Carbon

E J Zachariah, K Vasudevan, G Sreenivas, P Mohanan, P A Pravinkumar & K G Nair
Physics Department, Cochin University, Cochin 682 022

Received 24 *May* 1979

Development of a new type of microwave absorbing material using rubber latex and carbon, for application in the interior lining of anechoic chambers, has been reported. Absorption coefficients of different combinations were estimated at *X* and *S* bands and the results were presented graphically. A combination of 50% rubber latex, 40% carbon and 10% graphite is found to form an ideal microwave absorbing material in the *X* and *S* bands.

Microwave absorbing materials are of considerable importance in the fabrication of anechoic chambers for the study of antenna characteristics. These materials are widely used as antenna guard rings which will avoid backward scattering and side-lobe formation. Large quantities of such absorbing pads will be required and their non-availability is a real problem in India. The present note is a report of the work done in developing an indigenous microwave absorbing material using the raw materials available in plenty. The results of this preliminary investigation reveal the possibility of adopting the easily available low-cost microwave absorbing material for research and development activities in our country.

Most of the microwave absorbing materials used for anechoic chamber lining are based on costly synthetic materials like polyurethane. These base materials are not offering much absorption in the microwave range. Hence sufficient quantities of absorbing materials will be added to it during its formation. The absorbers thus used are fine powders of carbon, graphite and ferrites. The appropriate proportion of these will be determined at different frequency ranges.

Natural rubber seems to be a very good choice as a base material, for it has high absorption in almost all microwave frequencies and is available in plenty indigenously.

The samples are prepared by mixing the latex, carbon and graphite in different known proportions. Though the procedure appears to be simple, certain technical difficulties are to be encountered with setting of the compound, if the material added to latex is greater than 50%. So, keeping latex content in the compound at 50%, the ratio of carbon to graphite is varied. The best composition which would give maximum absorption in microwave region can be determined experimentally.

The experimental arrangement for absorption measurements is the usual test-bench assembly for VSWR measurements. This consists of a microwave source, an isolator, an attenuator, a slotted section carrying a tunable probe and crystal assembly connected to a VSWR meter and a waveguide section to take the absorber sample. A block diagram of the set-up is shown in Fig. 1.

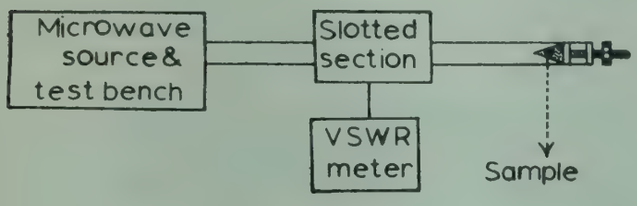

Fig. 1—Experimental set-up used

Table 1—Composition of Different Samples and Their Absorption Coefficients (Composition of rubber = 50% for all samples)

Sample No	% Composition of Carbon	% Composition of Graphite	Frequency GHz	Absorption coefficient
1	00	50	2·5	0·41
			3·9	0·41
			4·2	0·46
			9·3	0·42
2	10	40	2·5	0·52
			3·9	0·51
			4·2	0·65
			9·3	0·45
3	20	30	2·5	0·48
			3·9	0·42
			4·2	0·64
			9·3	0·54
4	30	20	2·5	0·58
			3·9	0·75
			4·2	0·79
			9·3	0·62
5	40	10	2·5	0·67
			3·9	0·86
			4·2	0·95
			9·3	0·78
6	50	00	2·5	0·63
			3·9	0·79
			4·2	0·80
			9·3	0·73

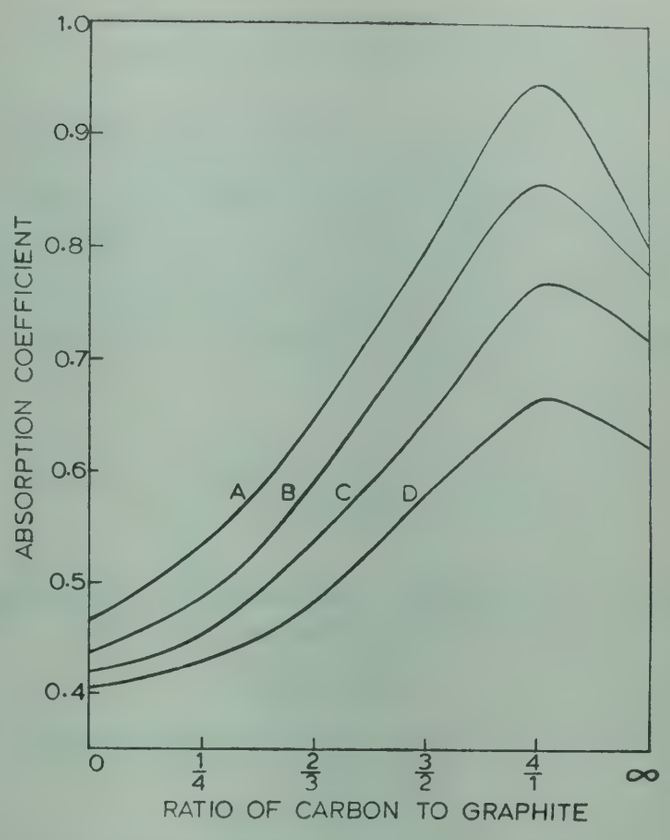

Fig. 2—Variation of the absorption coefficient with the composition of the sample at different frequencies. [For all samples, 50% is rubber; the proportion of graphite to carbon is varied in the remaining 50%; (A) 4·2 GHz; (B) 3·9 GHz, (C) 9·3 GHz and (D) 2·3 GHz.]

The absorber samples are cut exactly in the pyramidal shape, the base of which will have the same cross-section as the waveguide. This will minimize the reflections that would possibly interfere with the tunable probe. The height of the pyramid was kept greater than the wavelength of microwave radiation used. The sample is inserted in the free end of the waveguide such that its axis is collinear with the axis of the waveguide. The flat end of the pyramid touches a short-circuiting plunger. The VSWR with the absorber sample at the end of the system clearly indicates the nature of absorption and the absorption coefficient A can be calculated from the relationship,[1] $A = 1-\Gamma$, where Γ is the reflection coefficient given by $\Gamma = (S-1)/(S+1)$. Here S denotes the VSWR. Samples of six different compositions were put into the test-bench and the absorption coefficients were determined in each case. The observations are taken in the X and S bands and the results are presented in Table 1. A comparative analysis of results can be had from Fig. 2.

It is found that a combination of 50% rubber latex, 40% carbon and 10% graphite forms an ideal microwave absorbing material in the X and S bands. The material is sufficiently light and strong enough

to protrude as pyramids up to about 20 cm height and hence it will be ideally suited for interior lining of anechoic chambers.

The authors wish to acknowledge the valuable help and encouragement given by Prof. K Sathianandan, Head of the Department of Physics, Cochin University. Financial assistances given respectively to PM by the CSIR, (to EJZ by the Department of Atomic Energy and to KV, PAP and GS by the Department of Science and Technology, are also acknowledged.

References

1. Barlow H M & Cullen A L, *Microwave measurements* (Constable & Co, London), 1968.

Dipole & Quadrupole Polarizabilities & Shielding Factors of Li Using Hydrodynamic Analogy

V K Tondon*

Department of Physics, University of Roorkee, Roorkee

and

S K Suri & G C Shukla

Department of Physics, Basrah University, Basrah, Iraq

Received 25 *January* 1979

Electric dipole and quadrupole polarizabilities and shielding factors of the lithium atom have been calculated using hydrodynamic analogy in place of quantum mechanics. The results obtained have been critically analyzed and compared with those reported by earlier workers.

Hydrodynamic analogy as an alternative approach to quantum mechanics has been developed by Madelung and de Broglie[1,2] and extended by Takabayasi,[3] but only recently it has gained momentum and has been applied to various physical systems.[4-6] Its application to work out electric dipole polarizability of hydrogen atom was initiated by Weiner and Askar[7] and a variational analogue of the same was proposed by Askar and Demiralp.[8] Later, Shukla and Barbaro[9] extended this approach to calculate the multipole polarizabilities and shielding factors of the hydrogen atom. Recently this method has been applied to calculate the multipole polarizabilities and shielding factors of the lithium atom and its sequence.[10,11] In the present work, we have critically analyzed the static dipole and quadrupole polarizabilities and shielding factors of the lithium atom, using 6-term Clementi wavefunction and also simplified Shibuya wavefunction following the earlier communications.[10,11]

The multipole polarizabilities and shielding factors for the static case of the lithium atom are given by the following variational equations[10]

$$\delta \int_0^\infty |\psi_0(R)|^2 \left[(dF_L/dR)^2 R^2 + L(L+1) F_L^2 - 4 F_L R^{L+2}\right] dR = 0 \qquad ...(1)$$

where $\psi_0(R)$ is the radial part of the bound state wavefunction of Li atom and F_L is a polynomial in R given by

$$F_L(R) = F_L = C_{1L} R^L + C_{2L} R^{L+1} + C_{3L} R^{L+2} + ... \qquad ...(2)$$

In these expressions, L stands for multipoles, i.e. $L=1$ for dipole and $L=2$ for quadrupole. As shown in the earlier communication,[10] the multipole polarizability α_{2L} is given by

$$\alpha_{2L} = 2/(2L+1) \int_0^\infty |\psi_0(R)|^2 F_L R^{L+2} dR \qquad ...(3)$$

and the shielding factor β_{2L} by

$$\beta_{2L} = 2/(2L+1) \int_0^\infty |\psi_0(R)|^2 (F_L/R^{L-1}) dR \qquad ...(4)$$

The variational Eq. (1) reduces for the dipole case ($L=1$) to

$$\delta \int_0^\infty |\psi_0(R)|^2 \left[(dF_D/dR)^2 R^2 + 2 F_D^2 - 4 F_D R^3\right] dR = 0 \qquad ...(5)$$

and for the quadrupole case ($L=2$) to

$$\delta \int_0^\infty |\psi_0(R)|^2 \left[(dF_Q/dR)^2 R^2 + 6 F_Q^2 - 4 F_Q R^4\right] dR = 0 \qquad ...(6)$$

where F_D and F_Q, the functions F_L for $L=1$ and $L=2$, are

$$F_D = \sum_j C_{jD} R^j \qquad ...(7)$$

and

$$F_Q = \sum_j C_{jQ} R^{j+1} \qquad ...(8)$$

We start with the choice of F with $j=2$ and go up to the choice of F with $j=6$, and define I_l as

$$I_l = \int_0^\infty |\psi_0(R)|^2 R^l dR \qquad l=1, 2, 3, \text{etc.} \qquad ...(9)$$

Using these equations, we can write for the static dipole polarizability α_D, quadrupole polarizability α_Q and shielding factors β_D and β_Q as

$$\alpha_D = (2/3) \sum_{j=1}^{K} [C_{jD} (I_{j+3}) \qquad ...(10)$$

* Major part of this work was done when this author was at the Basrah University, Basrah, Iraq.

$$\alpha_Q = (2/5) \sum_{j=1}^{K} [C_{jQ}\, I_{j+5}] \qquad \ldots(11)$$

$$\beta_D = (2/3) \sum_{j=1}^{K} [C_{jD}\, I_j] \qquad \ldots(12)$$

$$\beta_Q = (2/5) \sum_{j=1}^{K} [C_{jQ}\, I_j]$$

with $K=2, 3, 4, 5$ or 6 ...(13)

The values of the coefficients C_{jD} and C_{jQ} are obtained using the variational Eqs. (5) and (6) respectively. The resulting equations for the typical cases of dipole and $K=5$, and quadrupole and $K=5$ are respectively

$$\begin{vmatrix} 1{\cdot}5I_2 & 2I_3 & 2{\cdot}5I_4 & 3I_5 & 3{\cdot}5I_6 \\ & 3I_4 & 4I_5 & 5I_6 & 6I_7 \\ & & 5{\cdot}5I_6 & 7I_7 & 8{\cdot}5I_8 \\ & & & 9I_8 & 11I_9 \\ & & & & 13{\cdot}5I_{10} \end{vmatrix} \begin{vmatrix} C_{1D} \\ C_{2D} \\ C_{3D} \\ C_{4D} \\ C_{5D} \end{vmatrix} = \begin{vmatrix} I_4 \\ I_5 \\ I_6 \\ I_7 \\ I_8 \end{vmatrix} \qquad \ldots(14)$$

$$\begin{vmatrix} 5I_4 & 6I_5 & 7I_6 & 8I_7 & 9I_8 \\ & 7{\cdot}5I_4 & 9I_7 & 10{\cdot}5I_8 & 12I_9 \\ & & 11I_8 & 13I_9 & 15I_{10} \\ & & & 15{\cdot}5I_{10} & 18I_{11} \\ & & & & 21I_{12} \end{vmatrix} \begin{vmatrix} C_{1Q} \\ C_{2Q} \\ C_{3Q} \\ C_{4Q} \\ C_{5Q} \end{vmatrix} = \begin{vmatrix} I_6 \\ I_7 \\ I_8 \\ I_9 \\ I_{10} \end{vmatrix} \qquad \ldots(15)$$

The $2\,S^1$ bound state wavefunction chosen for lithium atom is a linear combination of six—two of $1S$ type and four of $2\,S$ type—Slater orbitals (hereinafter called Clementi wavefunction[12]). Thus we have

$$\text{Li}\,(2\,S^1) = \psi_0 = \frac{1}{\sqrt{4\,\pi}}\,\psi_0\,(R)$$

$$= \frac{1}{\sqrt{4\,\pi}} \left[\sum_{i=1}^{2} A_i\, e^{-\xi_i R} + \sum_{i=3}^{6} A_i\, R\, e^{-\xi_i R} \right] \qquad \ldots(16)$$

Using Eq. (16), we can express I_l in terms of A_i and ξ_i as

$$I_l = l! \left[\sum_{i=1}^{2} \sum_{j=1}^{2} A_i\, A_j \,\middle|\, (\xi_i + \xi_j)^{l+1} \right]$$

$$+ (l+2)! \left[\sum_{i=3}^{6} \sum_{j=3}^{6} A_i\, A_j \,\middle|\, (\xi_i + \xi_j)^{l+3} \right]$$

$$+ 2\{(l+1)!\} \left[\sum_{i=1}^{2} \sum_{j=3}^{6} A_i\, A_j \,\middle|\, (\xi_i + \xi_j)^{l+2} \right] \qquad \ldots(17)$$

To calculate α_D, α_Q, β_D and β_Q, we use Eqs. (10)-(17). The values of variational constants C_{jD} and C_{jQ} are obtained by solving Eqs. (14) and (15) respectively, using Gauss's elimination subroutine.

To check the extent of results depending on the chosen form of ground state wavefunction, we have repeated the calculations with $2\,S^1$ wavefunction for Li atom as reported by Shibuya and Kozima[13] (hereinafter called Shibuya wavefunction).

The results obtained for the dipole and quadrupole polarizabilities and shielding factors of Li atom using the hydrodynamic analogy approach are presented in Table 1, along with the values reported by a few other workers.[10,14-18] Our values of the static dipole polarizability for Li ($\alpha_D = 20{\cdot}94$ Å^3), and quadrupole polarizability ($\alpha_Q = 61{\cdot}60$ Å^5) agree well with those of other workers; however, the shielding factors are low as compared with other estimates. Most of the earliar results obtained were based essentially on Hartree-Fock approximation (self-consistent, restricted or non-restricted) using Sternheimer procedure, whereas the present work — an alternative approach to work out the electronic polarizability for Li atom — rests mainly on the frozen core approximation and choice of the bound state wavefunction. Calculations have been made using two different wavefunctions, namely, 6-term Clementi wavefunction and Shibuya wavefunction. Table 1 shows that the Clementi wavefunction yields better values for polarizabilities compared with the Shibuya wavefunction. However, Shibuya wavefunction is a simplified one obtained without minimizing the total energy of the system and is meant

Table 1—Values of α_D, α_Q, β_D and β_Q of Li atom [Various parameters are in units of $A^2 L^{+1}$, where $L=1$ and 2 refer to dipole and quadrupole cases respectively]

Reference to work	α_D	α_Q	β_D	β_Q
Present work (using Clementi wavefunction)	20·94	61·60	0·42	0·031
Present work (using Shibuya wavefunction)	17·70	49·34	0·40	0·03
Shukla *et al.*[10]	20·63	59·577	0·39	0·029
Tewari *et al.*[14]	24·1	62·1	3·3	0·9
Langhoff *et al.*[15]	21·69	62·0	1·52	0·912
Sternheimer[16]	24·9	—	—	—
Caves and Dalgarno[17]	24·4	—	—	—
Experimental value[18]	22 ± 2	—	—	—

to be used only for discussing the properties of atoms qualitatively.[13] For Li atom, Shibuya wavefunction is a combination of only two orbitals, whereas Clementi wavefunction is that of six orbitals. However, it is interesting to note that the calculated values of the shielding factors are not very different for either choice of the wavefunction.

Our calculations for static polarizabilities depend on the choice of function F which we have taken as a polynomial in R. Since ours is a variational procedure, to test the convergence we have studied the effect of increasing the number of coefficients from 2 to 6 in F on the values of polarizabilities and shielding factors. We observe that there is an insignificant change in these values, if the number of coefficients is increased beyond 4. In the case of hydrogen atom,[9] only two such parameters have been found to be sufficient. An obvious plan for further work would be to calculate polarizability, etc. for other alkali atoms. We have tried to extend this approach to Na and K atoms. The preliminary results obtained for these atoms, using this formalism, yield unusually high values suggesting that this procedure may not be applicable to these alkali atoms in a straightforward fashion.

The authors express their sincere thanks to Dr R Al-Rashid and Prof. B P Singh for their encouragement during the course of this work.

References

1. Madelung E, *Z. Phys.*, 40 (1926), 322.
2. de Broglie, *C. r. hébd. Séanc. Acad. Sci., Paris*, **183** (1926), 447.
3. Takabayasi T, *Prog. theor. Phys., Osaka*, **8** (1952), 143; **9** (1953), 187; **11** (1955), 283.
4. Wilheim H E, *Phys. Rev.*, **D1** (1970), 2778.
5. Berula I B & Berula Z, *Phys. Rev.*, **D3** (1971), 2410.
6. Berula I B, *Phys, Rev.*, **D3** (1971), 2413.
7. Weiner J & Askar A, *J. chem. Phys.*, 54 (1971), 1108.
8. Askar A & Demiralp M, *J. chem. Phys.*, 60 (1974), 2762.
9. Shukla G C & Barbaro M, *Phys. Rev.*, A15 (1977), 23.
10. Shukla G C, Suri S K & Misho R H, *Solid St. Commun.*, 23 (1977), 67.
11. Tondon V K, Suri S K & Shukla G C, *Solid St. Commun.*, 25 (1978), 931.
12. Clementi E, *Atom. nucl. Data*, 14 (1974), 185.
13. Shibuya M & Kozima H, *J. phys. Soc. Japan*, **39** (1974), 1053.
14. Tiwari P, Rai D K & Rustogi M L, *Phys. Rev.*, **A1** (1970), 1567.
15. Langhoff P W, Karplus M & Hurst R P, *J. chem. Phys.*, 44 (1966), 505.
16. Sternheimer R M, *Phys. Rev.*, **127** (1962), 1220.
17. Caves J C & Dalgarno A, *J. quant. Spectrosc. radiat. Transfer*, **12** (1972), 1539.
18. Chamberlain G E & Zorn J C, *Phys., Rev.*, **129** (1963), 677.

Stability Measurements in Time Domain Using Dual Mixer Time Difference System

G M Saxena & B S Mathur

Time and Frequency Section, National Physical Laboratory
New Delhi, 110 012

Received 30 *October* 1978; *revised received* 23 *February* 1979

Results of the study of stability characterization of high precision oscillators and of the time domain stability measurements using Dual Mixer Time Difference (DMTD) system, have been reported. The experimental results are in good agreement with those from the existing theoretical models.

In this note results are reported of recently conducted frequency stability measurements on high performance crystal oscillators against a cesium and a rubidium standard. The measurements were confined on the time domain using dual mixer time difference system (DMTD). In this system, time fluctuations are measured instead of frequency fluctuations. This system can be used for making frequency stability measurements for sampling times as short as a few milli seconds and longer sample times as well without any dead time.

The definition of frequency stability of an oscillator in time domain[1] is based on the sample variance of the fractional frequency fluctuations. Before defining the stability in time domain, let us consider a signal generator whose instantaneous output voltage $V(t)$ is,

$$V(t)=V_0 + \epsilon(t)\,[\sin 2\pi\nu t - \phi(t)] \qquad ...(1)$$

where V_0 is the nominal peak voltage amplitude, $\epsilon(t)$ the deviation of amplitude from nominal, ν the nominal fundamental frequency and $\phi(t)$ the deviation of phase from nominal.

Ideally $\epsilon(t)$ and $\phi(t)$ should be equal to zero for all times. However, in reality there is no perfect oscillator and $\epsilon(t)$ as well as $\phi(t)$ are treated as noise components. The phase at instant t is

$$\phi(t) = 2\pi\nu t + \phi(t)$$

and instantaneous frequency ν' is expressed as,

$$\nu'(t) = \frac{1}{2\pi}\frac{d\phi}{dt} = \nu + \frac{\phi(t)}{2\pi} \qquad ...(2)$$

$y(t)$, the fractional frequency deviation from the nominal frequency ν is written as,

$$y(t) = \frac{\nu' - \nu}{\nu} = \frac{\phi(t)}{2\pi\nu} \qquad ...(3)$$

y_k the fractional frequency deviation averaged over a period τ during kth measurement, is defined as

$$\bar{y_k} = \frac{1}{\tau}\int_{t_k}^{t_k+\tau} y(t)\,dt = \frac{1}{2\pi\tau\nu}\int_{t_k}^{t_k+\tau} \tau(t)\,dt \qquad ...(4)$$

$$= \frac{\phi(t_k+\tau)-\phi(t_k)}{2\pi\nu\tau}$$

The parameter $\bar{y}$ is a dimensionless quantity; $t_{k+1} = t_k + T$, $k = 0, 1, 2, T$ is the repetition interval for measurements of duration τ and t_0 is an arbitrary initial moment. In time domain measurements, electronic counters are used for measuring the number of cycles in a period. This measures $\nu\tau\ (1 + \bar{y_k})$, where $\nu\tau\bar{y_k}$ is due to instability in the frequency. In time domain, frequency stability is defined in analogy to the sample variance by the relation

$$\left\langle \sigma_y^2(N, T, \tau) \right\rangle \equiv \frac{1}{N-1}\sum_{n=1}^{N}(\bar{y}_n - \frac{1}{N}\sum_{k=1}^{N}\bar{y}_k)^2 \qquad ...(5)$$

This measure of stability is dimensionless. An infinite time average of quantity within the angular bracket is indicated. But N, the number of data points used in obtaining a sample variance, cannot have infinite value. The value of N has to be optimized to have convergence of $\sigma_y^2\ (N, T, \tau)$ to a meaningful limit. Particular values $N = 2$ and $T = \tau$ (i.e. there is no dead time between consecutive measurements) have baen observed to improve the comparability of data.
with these values of N and T,

$$\sigma_y^2(N = 2, T = \tau) = \sigma_y^2(\tau) = \left\langle \frac{(\bar{y_k}+1-\bar{y_k})^2}{2} \right\rangle \qquad ...(6)$$

$\sigma_y^2\ (\tau)$ is the measure of the stability in time domain. It is conventionally known as Allan variance. The stability estimation using the Allan variance is dependent upon the number of independent samples. The statistical confidence of the calculated Allan variance improves nominally as the square root of the number of independent observations, M. The confidence of Allan variance is not better than $\frac{100}{\sqrt{M}}$ %.

The dual mixer time difference system used[2] by us at the National Physical Laboratory, New Delhi for measuring frequency stability is discussed below.

The block diagram of the set-up is shown in Fig. 1. There are two oscillators; one is a test oscillator whose stability is to be measured with respect to the other oscillator which is more stable and is used as a reference oscillator. In the present

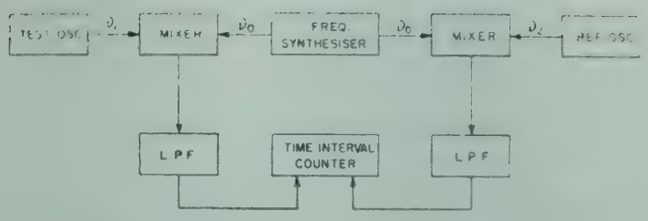

Fig. 1—Dual mixer time difference system for stability measurement in time domain

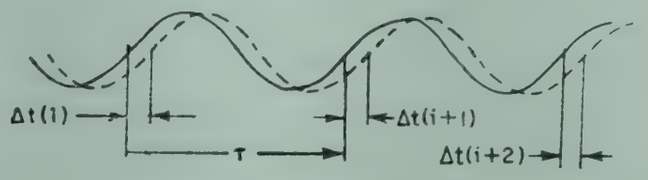

Fig 2—Schematic illustration of the positive going zero crossing of beats used to start and stop a time interval counter

case we have used two reference oscillators. The test oscillator, which is a crystal oscillator, is first compared with a commercial rubidium standard (HP 5065 A). In the second phase of the experiment the rubidium standard is replaced with a commercial cesium standard (HP 5061 A). Plots for both the cases have been presented for relative study. The standard 5 MHz signals from the test and reference oscillators are fed to the (L) ports of a pair of double balanced mixers (HP Model 10514 A, Schottky barrier diodes). A common oscillator (frequency synthesizer) with separate symmetric outputs feed to the remaining two (R) ports of the pair of mixers. The frequency of the common oscillator is offset by a desired amount from the other two oscillators. The two beat frequencies which in the present case are the same but, of different phases are fed to a time interval counter after filtering through a low-pass filter (LPF). The beat signals are of enough amplitude to drive the time interval counter. The start port input of the time interval counter is triggered with the zero crossing of one beat and the stop port input with the zero crossing of the other beat (Fig. 2). The time interval so measured gives the time difference between the test and the reference oscillators with a precision equal to that of the time interval counter reading multiplied by the ratio of the oscillator frequencies to the beat frequency.

The phase difference between the two oscillators is the same as the phase difference between the beat frequencies with the noise of the common oscillator getting cancelled. At the ith instant we have

$$\nu X(i) = \frac{\Delta t(i)}{\tau_1} + n \qquad ...(7)$$

Table 1—A Sample Calculation of Allan Variance $\sigma_y(\tau)$

$$\sigma_y(\tau) = \left\langle \sigma_y^2 (N=2, T=\tau) \right\rangle^{1/2} = \left\langle \frac{(\bar{y}_{k+1} - y_k)^2}{2} \right\rangle^{1/2}$$

Number of observations used	11
Number of difference averaged	10
Sampling time (τ)	3 sec
Beat period (τ_1)	0·05 sec
Nominal frequency	5·00 MHz

Time interval Δt (μ sec)	Data values $\bar{y}_k (\tau \tau_1 \nu) = (\Delta t_{i+1} - \Delta t_i)$	First difference $(\bar{y}_{k+1} - \bar{y}_k)$ $(\tau \tau_1 \nu)$	First difference squared $(\bar{y}_{k+1} - \bar{y}_k)^2$ $(\tau \tau_1 \nu)^2$
25909·1	+106·4	−105·0	11025
26015·5	+1·4	−60·6	3672·36
26016·9	−59·2	−14·8	219·04
25957·7	−74·0	+199·6	39840·16
25883·7	+125·6	−441·4	194833·96
26009·3	−315·8	+360·4	129888·16
25693·5	+44·6	−342·6	117374·76
25738·1	+298·0	+342·4	117374·76
25440·0	+44·4	−104·2	10857·64
25484·5	−59·8		
25424·7			

$$\sum_{k=1}^{9} (\bar{y}_{k+1} - \bar{y}_k)^2 (\tau \tau_1 \nu)^2 = 625085{\cdot}84$$

$$\sigma_y^2(\tau) = \frac{625085{\cdot}84}{2 \times 9 \times (\tau \tau_1 \nu)^2}$$

$$\sigma_y^2(\tau) = 2{\cdot}48 \times 10^{-10}$$

The confidence of the prediction $\sim \frac{100}{\sqrt{10}}$

$\sim 33\%$

where $X(i)$ is ith time difference between the two oscillators and $\Delta t(i)$ is the reading of the counter. Here τ_1 is the beat period, ν the nominal frequency and n represents the number of cycle ambiguity. As we are taking difference between the two measurements, n need not be calculated.

The fractional frequency can be derived in a normal way from the time fluctuations with averaging time same as beat period, as follows

$$y(i) = \frac{\nu' - \nu}{\nu}$$

$$\bar{y}(i, \tau_1) = \frac{X(i+1) - X(i)}{\tau_1} = \frac{\Delta t(i+1) - \Delta t(i)}{\tau_1^2 \nu} \quad \ldots (8)$$

In the present experiment the averaging time can be any multiple of the beat period. Let the averaging time be $\tau = m \tau_1$ where m is any positive integer Then the Eq. (8) is modified to,

$$\bar{y}(i, m\tau_1 = \tau) = \frac{X(i+m) - X(i)}{\tau} = \frac{\Delta t(i+m) - \Delta t(i)}{\tau \tau_1 \nu} \quad \ldots (9)$$

Substituting this value of $\bar{y}$ in Eq. (6) we can estimate $\sigma_y^2(\tau)$.

Two sets of readings were taken, each set containing 50 to 55 observations. In the first set the sampling time was kept at 3·5 sec and the reference oscillator was a Rb-standard. In the second set the sampling time (averaging time) was 3·0 seconds and the reference oscillator was a Cs-standard. Using the same data the Allan variance for $\tau = 10{\cdot}5$ sec in the first set was obtained by averaging the adjacent three readings. The Allan variance for averaging time of 17·5, 35, 52·5, 70 and 87·5 sec was similarly calculated. In the second set values of Allan variance for averaging times of 9, 15, 21, 30 42, 54, 60, 69 and 75 sec were obtained and plotted on a semi-log-graph. A sample computation of Allan variance is given in Table 1.

The results obtained in this experiment have been plotted on the semi-log scale (Fig. 3). $\sigma(\tau)$ versus τ plots of the crystal against both the Rb and the Cs standards, show the following behaviour. For small averaging times, the crystal shows

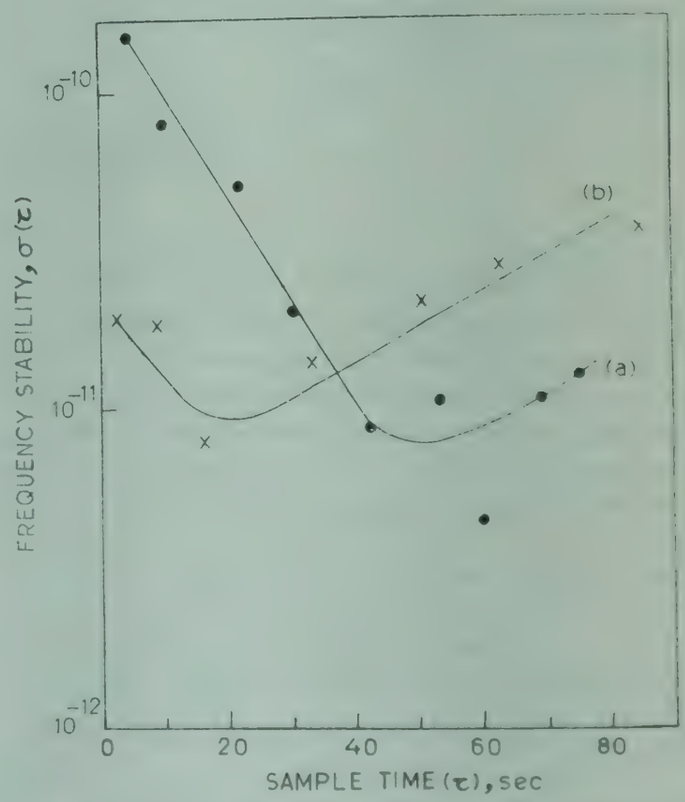

Fig. 3—$\sigma_y(\tau)$ versus τ plot of the fractional frequency fluctuations, $y(t)$, between the quartz crystal oscillator and (a) commercial Ce standard (HP 5061 A) and (b) Rb standard (HP 5065 A)

$\sigma(\tau) = \tau^{-1/2}$ behaviour. This trend can be identified with the white FM noise. The small middle region of the plot indicates the presence of flicker noise of the oscillator. The part of the plot for higher averaging times manifests $\sigma(\tau) = \tau^{+1/2}$ behaviour. This region shown the random walk FM noise in the oscillator.

In the $\sigma(\tau)$ versus τ plots the drift in the frequency of the test crystal oscillator has not been accounted for. Similarly, it was assumed that the noise in the measurement system is very small. The experiment was conducted at room temperature (21°C).

Efforts are being made to improve upon the environmental conditions and to measure the absolute stability of the crystal using triangular calculation method.

The authors are thakful to Dr P Banerjee for stimulating discussions and to Mr Hukam Singh for his help in preparing the manuscript.

References

1. Barnes James A, Chi A R & Cutler L S *et al.*, *IEEE Trans.*, IM-20 (May 1971), 105.
2. Allan D W, N B S Tech. Note 669, July 1975.

Vibrational Assignments of 2, 3-, 2, 5-, 2, 6-, & 3, 5-Dichloroanilines

R K Goel & S K Gupta*
Department of Physics, D N College, Meerut 250 002
and
R M P Jaiswal & P P Garg
Department of Physics, University of Kurukshetra, Kurukshetra 132 119

Received 1 *January* 1979; *revised received* 21 *July* 1979

The Raman spectrum of 2, 3-dichloroaniline (2, 3-DCA) has been recorded on a Russian ESP-51 three-prism glass spectrograph. Assignment of vibrational frequencies for all the 36 vibrational modes in each of 2, 3-; 2, 5-; 2, 6-; and 3, 5-dichloroanilines has been made based on the previous assignments of vibrational frequencies available in literature as well as on those of the present Raman observations in 2, 3- DCA. Thermodynamic functions of these molecules have also been computed on a TDC-316 computer.

The vibrational spectra of aniline have been studied in detail by Evans.[1] Vibrational spectra of a large number of mono-, di-, tri- and tetra- substituted anilines have also been studied by various workers.[2-7] The infrared studies of 2, 3-; 2, 5-; 2, 6-; and 3, 5- dichloroanilines along-with Raman study of 2, 6- dichloroaniline are available in literature.[3,8,9] A full use of the above data as well as the Raman spectrum of 2, 3- dichloroaniline recorded here has been made to prepare a fresh assignment of suitable frequencies to all modes of vibration in these molecules which are used to compute thermodynamic functions of these molecules.

Pure chemical, 2,3- dichloroaniline, obtained from M/s Tokyo Kesei Kogyo Co., Tokyo, was liquid at room temperature. Raman spectrum was recorded on a Russian ESP-51 three-prism glass spectrograph with a linear dispersion of 19 Å/mm at 4000 Å using a 6 cc Raman cell and low pressure. Hg-arc (3 A) 4358 Å line as the exciting radiation. Exposure time ranged between 25 and 35 hr. Measurements of Raman lines are accurate to within $\pm$ 5 cm^{-1}.

Taking NH_2 group as a point mass, 2, 3- and 2, 5-dichloroanilines (hereafter referred to as 2,3-DCA and 2, 5-DCA respectively) belong to C_s point group while 2,6- and 3,5-dichloroanilines (hereafter referred to as 2, 6-DCA and 3, 5-DCA respectively) belong to C_{2v} symmetry. Assignments of fundamental frequencies to various modes and their correlations are given in Table 1. In Table 2, six NH_2 group vibrations are correlated and compared with their counterparts in other similar molecules. Table 3 shows the principal moments of inertia, reduced moments of inertia, rotational constant (F) and barrier heights of 2,3-DCA, 2,5-DCA, 3,5-DCA and 2, 6-DCA molecules. Some of the vibrational assignments are discussed briefly in the following.

Skeleton vibrations—The C—H valence vibrations lie in the region 3030-3070 cm^{-1} (Ref. 10). In the case of 2,3-DCA, two Raman frequencies and two corresponding IR frequencies have been observed in this region and thus assigned to C—H stretching mode (Table 1).

Three very strong fundamentals in the case of 2, 3-DCA appear in the IR spectrum while only two have been observed in the Raman spectrum of this molecule in the region 1600-1400 cm^{-1} (Table 1). These have been assigned to correspond to the components of e_{2g} (1595 cm^{-1}) and e_{1u} (1485 cm^{-1}) modes of benzene. The strong bands observed at 997 ($985R^+$) and 767 cm^{-1} in 2, 3- DCA have been assigned to ring-breathing and trigonal bending modes respectively. This finds support from the assignments made by Singh and Singh.[3]

C—X *Vibrations*—In substituted anilines, the strong C—NH_2 stretching vibration appears near 1300 cm^{-1} (Ref. 3,7). A very strong band has been observed at 1307 cm^{-1} in the Raman spectrum of 2, 3-DCA. This frequency along with the corresponding strong IR frequency (1312 cm^{-1}) has been assigned to the above mode. A frequency around 200 cm^{-1} has

*Department of Physics, K K Jain Degree College Khatauli 251 201

Table 1—Assignment of Vibrational Frequencies (in cm^{-1}) of 2, 3-; 2, 5-; 3, 5- & 2, 6-Dichloroanilines

Point Group C_s				Point Group C_{2v}			
Species	2, 3-Dichloroaniline IR	2, 3-Dichloroaniline Raman	2, 5-Dichloroaniline (a)	Species	3, 5-Dichloroaniline	2, 6-Dichloroaniline (a)	Assignment/ mode
a'	3060(vs)	3067(s)	3060*	a_1	3094(vvw)	3080++	ν(C—H)
a'	3043+	—	3043	a_1	3043+	3068++	ν(C—H)
a'	1581(ms)	1585(vs)	1609	a_1	1587(vs)	1598++	ν(C—C)
a'	1465(vs) 1447(s)	1448(m)	1480	a_1	1445(vs)	1496++	ν(C - C)
a'	1312(s)	1307(vs)	1304	a_1	1302(s)	1315	ν(C—NH_2)
a'	1202(s)	1203(s)	1272	a_1	1253(ms)	1240	β(C—H)
a'	1097(vs)	1092(m)	1158	a_1	1107(vs)	1150	β(C—H)
a'	997(s)	985(s)	1038	a_1	989(s)	1068	Ring breathing
a'	767(vs)	779(vs)	779•	a_1	797(vs)	779•	α(C—C - C)
a'	737(s)	—	780	a_1	717(vs)	761*	ν(C—Cl)
a'	—	502(s)	328	a_1	529(m)	328•	α(C—C—C)
a''	957(m)	—	905	a_2	936(vs)	950	γ(C—H)
a''	397(ms) 385(m)	380(s)	380	a_2	397(mw) 382(vw)	380•	ϕ(C—C)
a''		168••	168••	a_2	168••	168••	γ(C—Cl)
a''	905(vs)	903(ms)	850	b_1	842(vs)	820	γ(C—H)
a''		830+	830	b_1	821(vs)	780	γ(C—H)
a''	697(s)	—	697*	b_1	702(sb)	697*	ϕ(C—C)
a''	437(m) 419(ms)	435(s)	447	b_1	427(s)	447+	ϕ(C—C)
a''		214(vs)	214•	b_1	214*	218++	γ(C—NH_2)
a''	—	121(s)	121•	b_1	121•	121*	γ(C—Cl)
a'	3024(s)	3017(w)	3017•	b_2	3017•	3017•	ν(C—H)
a'	1556(vw)	—	1588	b_2	1571(s)	1568++	ν(C—C)
a'		1418+	1418	b_2	1370(sb)	1472++	ν(C—C)
a'	1297(s)	—	1282	b_2	1272(ms)	1280	ν(C—C)
a'	1162(ms)	1155(w)	1198	b_2		1172	β(C—H)
a'	667(m)	—	720	b_2	658(vs)	711	ν(C—Cl)
a'	582(s)	581(vs)	578	b_2	578(ms)	578+	α(C—C—C)
a'	365(ms)	—	365•	b_2	367(vw)	365•	β(C—NH_2)
a'	325(w)		325•	b_2	325(w)	325*	β(C - Cl)
a'	299(vw)	282(s)	282•	b_2	297(vw)	282•	β(C—Cl)

a, Ref. 3; •, transferred from 2,3 DCA; +, transferred from 2,5 DCA; ••, transferred from Ref. 21; ++, from Ref. 9; s, strong; vs, very strong; sb, strong and broad; m, medium; ms, medium strong; mw, medium weak; w, weak; vw, very weak; ν, stretching; α, angle deformation; β, in-plane bending; and γ or ϕ, out-of-plane deformation.

Table 2—Correlation of Amino-Group Frequencies (in cm^{-1}) in Various substituted Anilines

Mode	2, 3-Dichloroaniline (a) IR	2, 3-Dichloroaniline (a) Raman	3, 5-Dichloroaniline (f)	3-Chloro-2-methylaniline (b)	3-fluoro 5-methyl aniline (c)	2,5DCA (d)	2,6 DCA (e)
ν_{asym} (N—H)	3484(sb)	3568(w)	3514(s)	3490(ms)	3466	3480	3465
ν_{sym} (N—H)	3394(vs)	3390(vs)	3421(vs)	3402(s)	3380	3378	3386
β (N—H) (scissoring)	1606(vs)	1613(s)	1616(ms)	1615(s)	1630	1626	1615
N—H twisting	1032(vs)	1033(s)	1062(mw)	1040(w)	1083	1088	1048
NH_2 wagging	—	644(w)	644+	624(s)	608(vs)	644+	682+
NH_2 torsion	242•	—	242•	242(ms)	240(vs)	242•	242•

(a), Present work; (b). Ref. 6; (c), Ref. 11; (d), Ref. 3; (e), Ref. 9; (f), Ref. 8; +, transferred from 2, 3 DCA; and *, transferred from Ref. 6.

Table 3—Computed Values of Moment of Inertia, Reduced Moments of Inertia, (F) and Potential Barrier Heights of 2, 3-; 2, 5-; 3, 5- & 2, 6- Dichloroanilines

Molecule	Principal moments of inertia (10^{-30} g-cm^2)			Reduced moments of inertia (10^{-32} g cm^2)	F (cm^{-1})	Barrier height V_0 kcal/mole
	I_x	I_y	I_z			
2, 3- Dichloro-aniline	124·09	70·42	53·84	0·2856	9·7919	4·2753
2, 5- Dichloro-aniline	159·48	131·19	28·45	0·2856	9·7924	4·2751
3, 5- Dichloro-aniline	59·22	157·23	98·16	0·2861	0·7747	4·2828
2, 6- Dichloro-aniline	98·17	138·14	40·14	0·2861	9·7748	4·2827

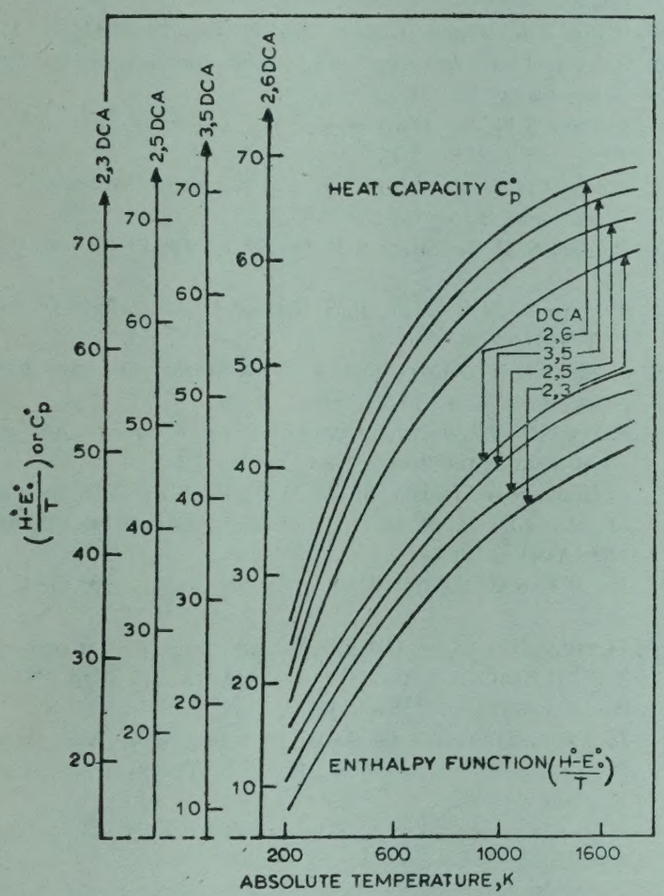

Fig. 1—Variation of enthalpy function and heat capacity with temperature

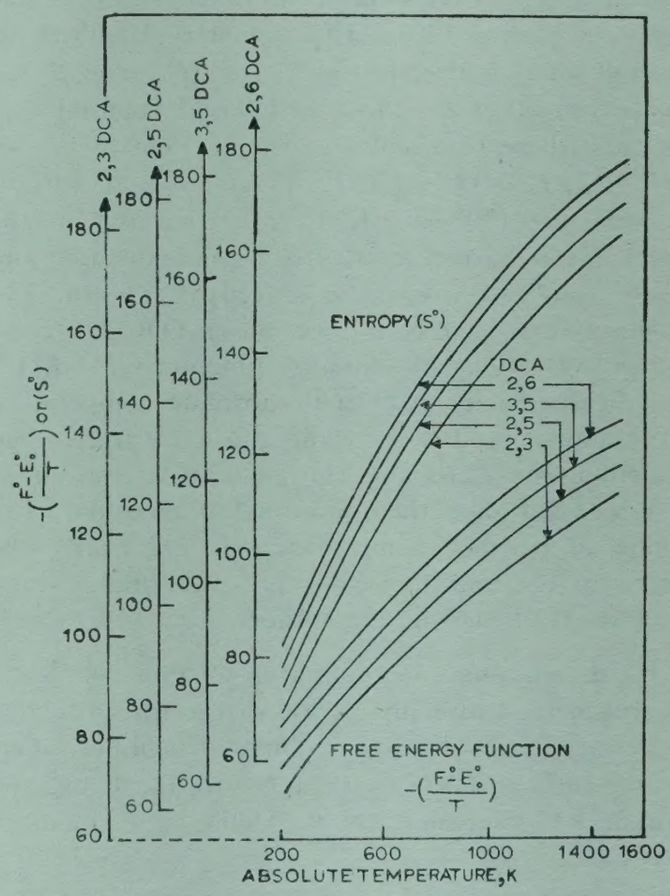

Fig. 2—Variation of free-energy function and entropy with temperature

been assigned to C—NH_2 out-of-plane deformation mode by various workers.[11,12] Thus the strong Raman band observed at 214 cm^{-1} in 2, 3- DCA has been assigned to this mode. The C—Cl stretching frequencies have been identified in the region 550-750 cm^{-1}, C—Cl in-plane bending vibration in the region 280-350 cm^{-1} and C—Cl out-of-plane vibrations in the 110-200 cm^{-1} range, by comparison with the previous assignments.[5,6,13-15]

NH_2 *group vibrations*—Evans[1] has assigned frequencies at 3440, 3360, 1618, 1054, 670 and 490 cm^{-1} respectively to the asymmetric stretching, symmetric stretching, bending or scissoring, twisting, wagging and first overtone of the torsional modes of NH_2 group in aniline. The NH_2 scissoring frequency appears in the region 1590-1650 cm^{-1} in nearly all primary aromatic amines.[10,16] Assignment of frequencies to this mode in the present case (Table 2) is also in agreement with the values given by Evans[1] and Sharma and Dwivedi.[6,11] A strong Raman frequency at 1613 cm^{-1} (Table 2) in 2,3-DCA supports the IR frequency assignment of this molecule to the above mode.

A frequency corresponding to the NH_2 torsional vibration could not be observed in the Raman spectrum of 2,3-DCA in the present study as also

in the cases of the rest of the title compounds. So a frequency at 242 cm^{-1} has been transferred for this mode from previous studies of various workers.[1,6]

Thermodynamic properties—Thermodynamic functions of 2,3-; 2,5-; 2,6- and 3,5- DCA molecules have been computed taking X-axis perpendicular to the molecular plane and Z-axis passing through the NH_2 group and utilizing standard expressions[17-19] and the fundamental frequencies of Tables 1 and 2. For determining the rotational contributions, the following structural parameters were used[1,20]: C—C = 1·397 Å, C—H (aromatic) = 1·084 Å, C—N = 1·42 Å, N—H = 1·02 Å, C—Cl = 1·70 Å, ∠ CCN = 120°, ∠CNH = 116° and ∠HNH = 112°. All other angles in the ring are taken as 120°. The symmetry numbers for overall rotation are taken as 1 for (C_s) and 2 for (C_{2v}) symmetries and those for internal rotation as 2 in all these molecules. The calculations of $(H^0-E_0^0)/T$, $-(F^0-E_0^0)/T$, S^0 and C_p^0 at various temperatures (200-1500 K) were carried out in the rigid rotor harmonic oscillator approximation and these relate to 1 mole of the perfect gas at 1 atm. The computations have been done on a TDC-316 computer. Variations of enthalpy function $(H^0-E_0^0)/T$ and heat capacity (C_p^0) with absolute temperature are shown in Fig. 1, while those of free-energy function $(F^0-E_0^0)/T$ and entropy (S^0) are given in Fig. 2, which show the usual trend of variation. The values of thermodynamic functions are nearly the same for the four molecules presently under study and are available with the authors.

The authors are thankful to Prof. N Nath, Kurukshetra University, Kurukshetra, for providing necessary laboratory and computer facilities. One of the authors (RKG) is thankful to the University Grants Commission, New Delhi, for financial assistance.

References

1. Evans J C, *Spectrochim. Acta*, 16 (1960), 428.
2. Ferguson E E, Hudson R L, Nielson J Rud & Smith D C, *J. chem. Phys.*, 21 (1953), 1457, 1464, 1470 & 1727.
3. Singh S N & Singh N L, *Indian J. pure appl. Phys.*, 7 (1969), 250.
4. Tripathi G N R & Pandey V M, *Indian J. pure appl. Phys.*, 13 (1975), 1860.
5. Sanyal Nitish K, Srivastava S L & Goel R K, *Indian J. pure appl. Phys.*, 16 (1978), 719.
6. Sharma S N & Dwivedi C P D, *Indian J. Phys.*, 50 (1976), 25.
7. Singh V B, Singh R N & Singh I S, *Spectrochim. Acta*, 22 (1966), 927.
8. Goel R K, Gupta S K & Sharma S N, *Pramana*, 11 (1978), 541.
9. Bishui P K, *Indian J. pure appl. Phys.*, 10 (1972), 637.
10. Bellamy L J, *Infrared spectra of complex molecules*, (John Wiley, New York), 1959.
11. Sharma S N & Dwivedi C P D, *Indian J. pure appl. Phys.*, 13 (1975), 570.
12. Green J H S, Harrison D J & Kynaston W, *Spectrochim. Acta*, 27A (1971), 793.
13. Pandey S M & Singh S J, *Indian J. Phys.*, 48 (1974), 961.
14. Tripathi G N R & Ram S, *Indian J. pure appl. Phys.*, 12 (1974), 529.
15. Green J H S, Harrison D J & Kynaston W, *Spectrochim. Acta*, 27A (1971), 807.
16. Rao C N R, *Chemical applications of infrared spectroscopy* (Academic Press, New York), 1963.
17. Colthup N B, Daly L H & Wiberley S E, *Introduction of infrared and Raman spectroscopy* (Academic Press, New York), 1964.
18. Pitzer K S & Cwinn W D, *J. chem. Phys.*, 10 (1942), 428.
19. Herzberg G, *Molecular spectra and molecular structure*, Vol. II, Infrared and Raman spectra (D Van Nostrand, Princeton, USA), 1966, 511.
20. *International tables for X-ray crystallography*, Vol. III—*Physical & chemical tables*, (Kynoch Press, Birmingham, England), 1962.
21. Goel R K, Sharma S D, Jaiswal R M P & Garg P P, Unpublished work.

INSTRUCTIONS TO CONTRIBUTORS

Manuscripts should be typewritten in double space and on *only one side* of good quality paper; the original and *one carbon copy are to be submitted.*

Papers must be written in clear and concise English. Good attention to spelling and grammar should be given. Long introductions should be avoided. Standard international nomenclature should be followed in giving names of chemical compounds. Standard abbreviations for units of measurement should be used in the text, tables and illustrations. The abbreviations should be used without fullstops.

Title—The title should be neither too brief/general nor unnecessarily long. It should reflect the content of the paper so as to derive the maximum advantage in indexing and information retrieval. A short title for use as running title should also be supplied. If a paper forms part of a series, a subtitle indicating the aspects of the work covered in the paper should be provided.

Abstract—The abstract should indicate the scope of the work and the principal findings of the paper. It should not exceed 3% of the length of the paper and, barring exceptional cases, it should not exceed 200 words. The abstract should be prepared in such a form that abstracting periodicals can use it without modification.

Data—Only such primary data as are essential for understanding the discussion and the main conclusions emerging from the study should be included. All such secondary data as are of interest to a specific category of readership may, if necessary, be deposited in the editorial office (or retained by the authors) for supply on demand. A footnote to this effect may be inserted at a suitable place in the paper.

Mathematical portions—Special attention should be given to the mathematical portions of the paper. Equations must be well separated from the text and written clearly with good separation between the successive lines. The usual norms of breaking long mathematical expressions may be adhered to. Equations should be numbered consecutively in Arabic numerals with the number in parentheses near the right hand margin. Superscripts and subscripts should be clearly indicated in pencil by $\vee$ and $\wedge$ sign respectively. Capital and small letters, particularly of the same letter when both occur, as well as letters or symbols likely to be confused one for the other, should be clearly distinguished. Special characters (e.g. Greek, script, vector, tensor, matrix, etc.) required must be indicated by marginal notes. Letters and symbols which should appear in bold face must be clearly indicated. To simplify typesetting: (i) long and complicated mathematical expressions which are frequently repeated should be replaced with single letter/symbol, without clashing with the others used in the paper; (ii) the "exp" form of complex exponential functions should be used: and (iii) to simplify fractions, the solidus (/) is to be used and fractional exponents are to be used instead of root signs, e.g.

write $\left(4\omega_{pl} K_{s\lambda}^2 \Big/ \tilde{\omega}\ K_D^2\right)^{1/2}$ and *not* $\sqrt{4\,\frac{\omega_{pl} K_{s\lambda}^2}{\tilde{\omega}\, K_D^2}}$

write $\exp\{-i\omega_0 (t_1 - t_2)/2\}$ and *not* $e^{-i\omega_0 (t_1 - t_2)/2}$

Tables—Tables should be typed *on separate sheets* of paper without any text matter on the page. They should be numbered consecutively in Arabic numerals and should bear brief titles. *Column headings should be brief.* Units of measurements should be abbreviated and placed below the headings. Nil results should be indicated and distinguished clearly from absence of data. Graphs as well as tables, both representing the same set of data, must be strictly avoided. Inclusion of structural formulae inside the tables should be avoided as far as possible. Tables should be referred to in the text by numbers and not by terms like 'above', 'below', 'preceding' or 'following'.

Illustrations—All illustrations should be numbered consecutively in Arabic numerals. Captions and legends to the figures should be self-explanatory and should be typed on a separate sheet of paper and attached at the end of the manuscript. Line drawings should be made with Indian ink on white drawing paper (perferably Bristol board), cellophane sheet or tracing cloth. In addition to the originals, a set of blue-prints or photostat copies should be sent. For satisfactory reproduction, the graphs and line drawings should be drawn to approximately twice the printed size.

The lettering should be uniform, perferably in stencil, so as to be *not less than 2 mm after reduction* widthwise to 3″ or 6″ as required. The size of geometrical shapes (used to distinguish different graphs), dot, lines, etc. should be sufficiently large to permit the necessary reduction without loss of detail. In the case of *photographs*, prints *must be on glossy paper and contrasty*. If an illustration is taken from another publication, reference to the source should be given and prior permission secured. Illustrations should be protected by thick cardboard packing against creases, folds and broken corners during transit. Illustrations should be referred to in the text by numbers and not by terms like 'above', 'below', 'preceding' or 'following'.

Infrared, ultraviolet, NMR and other spectra, DTA curves, etc. should be included only if they pertain to new compounds and/or are essential to the discussion; otherwise only significant numerical data should be included in the text.

References—The list of references should be prepared strictly in accordance with the style followed

in the Journal. In the text, references to literatures should be numbered consecutively, in the order of their first occurence, and should be indicated by superscripts at the relevant places; as far as possible the placement of references on numerals of other symbols should be avoided; in such cases the reference may be given in parentheses in running text, e.g. "this yielded for n a value of 2·3 (Ref. 5)". Full bibliographic details for all the references mentioned in the text should be listed in serial order at the end of the paper.

In citing references to research papers, names and initials of authors should be followed, in order, by the title of the periodical in the abbreviated form (underlined), the volume number (two lines underneath), the year within circular brackets and the page reference [e.g. Venkatesh, H G & Guha Sarkar, G, *Indian J. pure appl. Phys.*, 12 (1974), 502]. For names of periodicals, the standard abbreviations listed in the *World list of scientific periodicals* edited by P Brown & G B Stratton (Butterworths & Co. Ltd, London), 4th Edition, 1963-65, should be used. If the reference is to an article published without any authorship in a periodical, the title of the article takes the place of the author in the citation [e.g. The content, influence and value of scientific conference papers and proceedings. *Unesco Bull. Libr.*, 16 (1952), 113-26.]. If a paper has been accepted for publication, the names of the authors and the journals should be given followed by the words "in press" within circular brackets [e.g. Sastry, B. A. & Sastry, G. S., *Physica*, (in press).].

In the list of references, unpublished work, accepted papers in press and personal communications should be clearly distinguished.

Even if a reference contains more than two authors, the names of all the authors with their respective initials should be given. The abbreviations *et al.*, *idem* and *ibid* should be avoided.

Reference to a book should include details in the following order: names and initials of authors, the title of the book (underlined), name of publisher and place of publication within circular brackets and year [e.g. Herzberg, G, *Spectra of diatomic molecules* (D Van Nostand & Co. Inc., New Jersey), 2nd Edn, 1950, 31.]. If the reference is to the work of an author published in a book by a different author or edited by a different person, the fact that it is cited from the source book should be clearly indicated [e.g. Garlick, G F J, cited in *Encyclopedia of Physics*, Vol. 26—*Light and matter* II, edited by S Flugge (Springer Verlag, Berlin), 1958, 1.].

Proceedings of conferences and symposia should be treated in the same manner as books. Reference to a paper presented at a conference, the proceedings of which are not published, should include, in the following order, names and initials of authors, title of the paper (underlined), name of the conference, place where the conference was held and date (Deekshitulu, B L, *Design and fabrication of drum scanner for picture processing*, paper presented in the Symposuim on Applied Optics, Indian Institute of Science, Bangalore, 28-30 Nov. 1974).

Reference to a thesis should include the name of the author, title of the thesis (underlined), university or institution to which it was submitted and year of submission (e.g. Chandrasekaran, K S., *Studies on crystal structure and absolute configuration of crystals*, Ph. D. thesis, Madras University, 1956).

Reference to a patent should include names of patentees, country of origin (underlined) and patent number, the organization to which the patent has been assigned within circular brackets, data of acceptance of the patent and reference to an abstracting periodical where available [Trepagnier, J H, *US Pat.* 2,463,219 (to E I du Pont de Nemours & Co.), 1 March 1949, *Chem. Abstr.*, 43 (1949), 7258.].

Abbreviations and symbols—Abbreviations used should conform to the style of the journals. The following prefixes to units of measurements may be used for expressing submultiples and multiples.

Submultiples	*Abbreviation*	*Multiples*	*Abbreviation*
Deci- ($=10^{-1}$)	deci	deca- ($=10^{1}$)	deca-
centi- ($=10^{-2}$)	c	hecto- (10^{2})	hecto
milli- (10^{-3})	m	kilo- ($=10^{3}$)	k
micro- ($=10^{-6}$)	μ	mega- ($=10^{6}$)	M
nano- ($=10^{-9}$)	n	giga- ($=10^{9}$)	G
pico- ($=10^{-12}$)	p	tera- ($=10^{12}$)	T
femto- ($=10^{-15}$)	f		
atto- ($=10^{-18}$)	at		

Frequently repeating combinations of words, e.g. electric field gradient (EFG), junction field effect transistor (JFET), stimulated Raman emission (SRE), should be abbreviated subsequently, indicating the abbreviated form in parentheses, as shown, at the place of their first occurrence.

Nomenclature—Where too many symbols are used in the text, a section entitled "Nomenclature", explaining the significance of the various symbols, may be given and placed just above the Acknowledgement section.

Acknowledgement—Acknowledgements should not be exuberant and must be made only to real assistance rendered in connection with the work reported in the paper.

Appendixes—Appendixes, typed on separate sheets, should be numbered consecutively, in Arabic numerals, in the order of their occurence in the text, and should be placed at the very end of the paper.

Printed and Published by Shri D S Sastry, Publications & Information Directorate, Council of Scientific & Industrial Research, New Delhi, at the Leipzig Press, D-52 South Extension Part I, New Delhi-110 049, India

Regd. D-(C)-540